International Scientific-Technical and Production Journal

The Paton WELDING JOURNAL

December
2012
# 12

English translation of the monthly «Avtomaticheskaya Svarka» (Automatic Welding) journal published in Russian since 1948

Founders: *E.O. Paton Electric Welding Institute of the NAS of Ukraine*
International Association «Welding»

Publisher: *International Association «Welding»*

Editor-in-Chief B.E.Paton

Editorial board:
Yu.S.Borisov V.F.Khorunov
A.Ya.Ishchenko I.V.Krivtsun
B.V.Khitrovskaya L.M.Lobanov
V.I.Kyrian A.A.Mazur
S.I.Kuchuk-Yatsenko
Yu.N.Lankin I.K.Pokhodnya
V.N.Lipodaev V.D.Poznyakov
V.I.Makhnenko K.A.Yushchenko
O.K.Nazarenko A.T.Zelnichenko
I.A.Ryabtsev

International editorial council:
N.P.Alyoshin (Russia)
U.Diltey (Germany)
Guan Qiao (China)
D. von Hofe (Germany)
V.I.Lysak (Russia)
N.I.Nikiforov (Russia)
B.E.Paton (Ukraine)
Ya.Pilarczyk (Poland)
G.A.Turichin (Russia)
Zhang Yanmin (China)
A.S.Zubchenko (Russia)

Promotion group:
V.N.Lipodaev, V.I.Lokteva
A.T.Zelnichenko (exec. director)
Translators:
A.A.Fomin, O.S.Kurochko,
I.N.Kutianova, T.K.Vasilenko
Editor:
N.A.Dmitrieva
Electron galley:
D.I.Sereda, T.Yu.Snegiryova

Address:
E.O. Paton Electric Welding Institute,
International Association «Welding»,
11, Bozhenko str., 03680, Kyiv, Ukraine
Tel.: (38044) 200 82 77
Fax: (38044) 200 81 45
E-mail: journal@paton.kiev.ua
URL: www.rucont.ru

State Registration Certificate
KV 4790 of 09.01.2001

Subscriptions:
$348, 12 issues per year,
postage and packaging included.
Back issues available.

All rights reserved.
This publication and each of the articles contained herein are protected by copyright.
Permission to reproduce material contained in this journal must be obtained in writing from the Publisher.
Copies of individual articles may be obtained from the Publisher.

CONTENTS

SCIENTIFIC AND TECHNICAL

Makhnenko V.I., Velikoivanenko E.A., Rozynka G.F. and *Pivtorak N.I.* Consideration of pore formation at estimation of limiting state in zone of pressure vessel wall thinning defect 2

Kostin V.A., Grigorenko G.M., Poznyakov V.D., Zhdanov S.L., Solomijchuk T.G., Zuber T.A. and *Maksimenko A.A.* Influence of welding thermal cycle on structure and properties of microalloyed structural steels 8

Golikov N.I. and *Dmitriev V.V.* Residual stresses in circumferential butt joints in the main gas pipeline at long-term service in the North 15

Goncharov I.A., Sokolsky V.E., Davidenko A.O., Galinich V.I. and *Mishchenko D.D.* Formation of spinel in melt of the $MgO-Al_2O_3-SiO_2-CaF_2$ system agglomerated welding flux and its effect on viscosity of slag 18

INDUSTRIAL

Lobanov L.M., Pashchin N.A., Mikhoduj O.L., Cherkashin A.V., Manchenko A.N., Kondratenko I.P. and *Zhiltsov A.V.* Effectiveness of various variants of electrodynamic treatment of AMg6 alloy and its welded joints 26

Shelyagin V.D., Khaskin V.Yu., Akhonin S.V., Belous V.Yu., Petrichenko I.K., Siora A.V., Palagesha A.N. and *Selin R.V.* Peculiarities of laser-arc welding of titanium alloys 32

Kolomijtsev E.V. Corrosion-fatigue strength of 12Kh18N10T steel T-joints and methods of its improvement 36

Pokhodnya I.K., Yavdoshchin I.R. and *Gubenya I.P.* Influence of content of iron powder and compounds of alkali metals in the composition of electrode coating on their sanitary-hygienic characteristics 38

Makovetskaya O.K. Modern welding market of the North America 41

NEWS

Opening of Laser Center in Kirov, RF 44

International Specialised Exhibition of Welding Consumables, Equipment and Technologies «Weldex/Rossvarka 2012» 46

Index of articles for TPWJ'2012, Nos. 1–12 49

List of authors 53

© PWI, International Association «Welding», 2012

CONSIDERATION OF PORE FORMATION AT ESTIMATION OF LIMITING STATE IN ZONE OF PRESSURE VESSEL WALL THINNING DEFECT

V.I. MAKHNENKO, E.A. VELIKOIVANENKO, G.F. ROZYNKA and **N.I. PIVTORAK**
E.O. Paton Electric Welding Institute, NASU, Kiev, Ukraine

The tough fracture models allowing for pores forming in plastic flow either at non-metallic inclusions or in matrix from the microcracks that do not propagate by cleavage mechanism provide for the corresponding algorithms of growth of the pore due to plastic strains and respective redistribution of the stress-strain state. At present, the interest in these models is determined by growth of the scope of prediction and expert estimates for the welded structures, based on calculation estimation of the limiting state. In a number of cases, in view of the trend to utilization of high-strength and sufficiently ductile materials in the welded structures, the limiting state occurs under the tough deformation conditions at the rigid stressed state, which contribute to the pore formation. Fracture as a result takes place at relatively small plastic strains that rapidly reduce deformation capacity of corresponding welded assemblies before fracture.

Keywords: *steel pressure vessels, development of plastic flow, limiting state, pore formation, fracture zone, criteria of fracture involving pores, spontaneous fracture*

Operational defects of wall thinning in current welded pressure vessels are the most widely identified defects of long-term service structures (main pipeline, oil and gas storages, tank cars etc.). At periodic technical diagnostics of such structures the identified defects are estimated from point of view of safe operation of the structure for a period at least up to the next technical diagnostics. Specific rules based on corresponding calculation and experimental investigations are applied at that. These rules are improved according to accumulation of facts of their application, change of operation conditions for specific type of structures, development of calculation models of loading (fracture) as well as methods of realization of these models.

Observed significant progress in computer engineering, deformation and fracture mechanics of structural materials, respectively, provides for realization of the more complex physical models. It is a good basis for development of more detailed models of behavior of structural material at deformation (in stage close to fracture) as well as at fracture to certain extent. This makes the calculation approaches to prediction of a limiting state for complex cases of deformation sufficiently suitable to that is observed in experiment allowing reducing the scope of expensive experiments. Such an approach is connected with attraction of additional physical and mathematical models for development of information related with the coming of limiting state. Work in this direction is actively performed in different countries. Works of scientists of Siberian school of Prof. V.E. Panin in scope of new scientific direction, i.e. physical mesomechanics of materials [1], are worthy of notice among the current investigations. Deformation of material on mesolevel, i.e. considering significant physical discontinuity determined by presence of different interfaces (for example, gain boundary) with further estimation of reaction of material on macrolevel by means of average of characteristics of stress-strain state along representative mesovolume is considered in scope of this direction. Primitive example of inelastic material behavior according to [1] is a «shear + rotation» that allows preserving continuity condition up to fracture. The latter is a final stage of material fragmentation on macrolevel when global shear buckling takes place.

Pore formation in many cases is an important phase of material deformation before fracture stage. The pores are formed in plastic flow at non-metallic inclusions or in matrix from the microcracks that do not propagate by cleavage mechanism, i.e. being almost essential attribute of material tough fracture. It is not surprising that a great attention is paid to the issue of formation and growth of pores at tough fracture of materials [2–4]. Initial dimensions of appearing pores are not large around 1 μm as a rule. Therefore, their influence on deformation processes and fracture can be considered in scope of mesolevel

© V.I. MAKHNENKO, E.A. VELIKOIVANENKO, G.F. ROZYNKA and N.I. PIVTORAK, 2012

models, i.e. corresponding inhomogeneity of material properties in pore volumes and out of these volumes.

The results obtained under the following assumptions are given below.

The pores are nucleated in an arbitrary finite element (structural volume) under isothermic conditions, when intensity of plastic strain ε_i^p is more than specified value $(\varepsilon_i^p)_{\rm n}$ and they are uniformly distributed along the element volume, i.e. concentration of pores per unit of element volume is

$$\begin{gathered}\rho_V = \frac{V_{\rm p}}{V_{\rm f.e}} \text{ at } \varepsilon_i^p \ge (\varepsilon_i^p)_{\rm n}, \\ \rho_V = 0 \text{ at } \varepsilon_i^p < (\varepsilon_i^p)_{\rm n},\end{gathered} \tag{1}$$

where $V_{\rm p}$ is the pore volume; $V_{\rm f.e}$ is the element volume without pores.

ρ_S concept of pore concentration per unit of sectional area of the element (that can be observed in sample fracture) is introduced. By analogy with (1)

$$\begin{gathered}\rho_S = \frac{S_{\rm p}}{S_{\rm f.e}} > 0 \text{ at } \varepsilon_i^p \ge (\varepsilon_i^p)_{\rm n}, \\ \rho_S = 0 \text{ at } \varepsilon_i^p < (\varepsilon_i^p)_{\rm n},\end{gathered} \tag{2}$$

where $S_{\rm p}$ is the area of pores in given section of $S_{\rm f.e}$ value.

$l_{\rm p}$ is the total length of pores per unit of linear dimension $l_{\rm f.e}$, respectively. Then

$$\rho_l = \frac{l_{\rm p}}{l_{\rm f.e}}. \tag{3}$$

Relationship between ρ_V and ρ_l is

$$\rho_V = (1 + \rho_l)^3 - 1 = 3\rho_l \left(1 + \rho_l + \frac{1}{3}\rho_l^2\right) \approx 3\rho_l. \tag{4}$$

Correspondingly $\rho_S = 2\rho_l \left(1 + \frac{1}{2}\rho_l\right) \approx 2\rho_l$.

Developed plastic flow promotes growth of pore linear dimensions according to Rice–Tracy law [4] at $\varepsilon_i^p \ge (\varepsilon_i^p)_{\rm n}$.

Assume that the amount of pores in given structural volume has little changes, but their dimensions increase:

$$\frac{dl}{d\varepsilon_i^p} = 0.28 l \exp\left(1.5 \frac{\sigma_m}{\sigma_i}\right), \tag{5}$$

where σ_m / σ_i is the rigidity of stressed state; $\sigma_m = \frac{1}{3}(\sigma_{rr} + \sigma_{\beta\beta} + \sigma_{zz})$ is the average normal stress in coordinate system r, β, z;

$$\begin{gathered}\sigma_i = \frac{1}{\sqrt{2}} [(\sigma_{rr} - \sigma_{\beta\beta})^2 + (\sigma_{rr} - \sigma_{zz})^2 + \\ + (\sigma_{\beta\beta} - \sigma_{zz})^2 + 6(\sigma_{rz}^2 + \sigma_{r\beta}^2 + \sigma_{\beta z}^2)]^{1/2}\end{gathered} \tag{6}$$

is the stress intensity;

$$\begin{gathered}d\varepsilon_i^p = \frac{\sqrt{2}}{3} [(d\varepsilon_{rr}^p - d\varepsilon_{\beta\beta}^p)^2 + (d\varepsilon_{rr}^p - d\varepsilon_{zz}^p)^2 + \\ + (d\varepsilon_{\beta\beta}^p - d\varepsilon_{rr}^p)^2 + 6(d\varepsilon_{r\beta}^p)^2 + 6(d\varepsilon_{rz}^p)^2 + 6(d\varepsilon_{\beta z}^p)^2]^{1/2}\end{gathered}$$

is the intensity of increase of plastic strain.

Under mentioned above assumption that amount of pores in given volume V_0 has small changes, the change of ρ_l value corresponds with relative variation of the linear dimensions due to porosity.

Respectively, equation of relationship of strain tensor $d\varepsilon_{ij}$ and stress tensor σ_{ij} at i, $j = r$, z, β allowing for linear elongation equals ρ_l can be written in the following way:

$$\begin{gathered}d\varepsilon_{ij} = d\left(\frac{\sigma_{ij} - \delta_{ij}\sigma_m}{2G}\right) + \\ + d\lambda(\sigma_{ij} - \delta_{ij}\sigma_m) + \delta_{ij}[d(K\sigma_m) + d\rho_l],\end{gathered} \tag{7}$$

where ρ_l is the solution of equation (5) at $l = \rho_l$ and initial ρ_l value on (1) and (4); $G = E/(2(1 + \nu))$; $K = (1 - 2\nu)/E$; E is the Young's modulus; ν is the Poisson's ratio; $\delta_{ij} = 1$ at $i = j$ and $\delta_{ij} = 0$ at $i \ne j$.

Under sequential tracing of development of plastic strain and initial value of $\rho_V^{\rm init}$ in moment $k = 0$ on (1), assuming that $d\varepsilon_i^p$ value has small changes in a course of tracing steps k-th and $k + 1$st, solution of equation (5) relatively to value ρ_l will give

$$\ln \frac{\rho_l^{(k+1)}}{\rho_l^{(k)}} = 0.28 \exp\left(1.5 \frac{\sigma_m^{(k)}}{\sigma_i^{(k)}}\right) (\Delta\varepsilon_i^p)^{(k)}. \tag{8}$$

Under values of relationship $x = \frac{\rho_l^{(k+1)}}{\rho_l^{(k)}}$ close to one, expanding $\ln x$ as a power series

$$\ln x = 2 \sum_{n=1}^{\infty} \left(\frac{x - 1}{x + 1}\right)^n \frac{1}{n} \tag{9}$$

and being limited by member $n = 1$, the following will be obtained:

$$\begin{gathered}\rho_l^{(k+1)} = \frac{(2 + A_k)\rho_l^{(k)}}{2 - A_k}, \text{ where} \\ A_k = 0.28 \exp\left(1.5 \frac{\sigma_m^{(k)}}{\sigma_i^{(k)}}\right) (\Delta\varepsilon_i^p)^{(k)}\end{gathered} \tag{10}$$

starting from $k = 0$, for which $\rho_l^{(0)}$ is determined by conditions (4).

Knowing $\rho_l^{(k)}$ ($k = 0, 1, 2, \dots$), an increment of elongation of linear dimensions of given finite element due to porosity will be found for (7)

$$\Delta\rho_l^{(k+1)} = \rho_l^{(k+1)} - \rho_l^{(k)} = \rho_l^{(k)} \frac{A_k}{1 - 0.5A_k} \qquad (k = 0, 1, 2, \dots). \tag{11}$$

It follows from mentioned above that consideration of porosity affects to certain extent the strain and stress fields due to additional volumetric changes of $\Delta\rho_l^{(k+1)}$ ($k = 0, 1, 2, \dots$) value similar to such at temperature expansion $\Delta\varphi$ [5].

Besides, realization of flow conditions and criteria of limiting state requires consideration of net-stress in sections of finite elements, i.e. $\sigma_{ij}^{(k)}$ values from solution of boundary value problem equate to net-stress $(\sigma_{ij}^{\mathrm{net}})^{(k)} = \dfrac{\sigma_{ij}^{(k)}}{1 - \rho_s^{(k)}}$.

The following according to [2] are used as criteria of the limiting state of brittle-tough fracture in volume of given finite element:

$$\begin{gathered} \sigma_1 > S_{\mathrm{c}} \text{ — brittle fracture;} \\ \kappa_k > \varepsilon_{\mathrm{cr}}^{(k)} \left(\frac{\sigma_m}{\sigma_i}\right) \text{ — tough fracture,} \end{gathered} \tag{12}$$

where σ_1 is the maximum main net-stress; $\kappa_k = \int d\varepsilon_i^p = \sum\limits_k (d\varepsilon_i^p)^{(k)}$ is the Odqvist parameter of strain hardening; $\varepsilon_{\mathrm{cr}}^{(k)}$ is the critical value κ_k in k-th tracing step depending on rigidity of stressed state.

For example, based on MacKenzie [2]

$$\varepsilon_{\mathrm{cr}}^{(k)} \left(\frac{\sigma_m}{\sigma_i}\right) > \varepsilon_0 + a \exp\left(-1.5 \frac{\sigma_m^{(k)}}{\sigma_i^{(k)}}\right), \tag{13}$$

where ε_0 and a are the experimental characteristics of materials (for hull steels $\varepsilon_0 = 0.07$, $a = 2.99$).

Method of accumulation of tough fractures in the volume of given element can be used according to [2] in the next form for the case of rapid change in tracing of $(\sigma_m/\sigma_i)^{(k)}$ and $\varepsilon_{\mathrm{cr}}^{(k)}$ values respectively:

$$\sum_{k=0}^{k_{\mathrm{cr}}} \left(\frac{\Delta\varepsilon_i^p}{\kappa}\right)_k = 1, \tag{14}$$

where k_{cr} is the limiting value of tracing step at which given finite element will «fail», i.e. its mechanical properties rapidly change for properties of air or corresponding aggressive liquid (in presence of respective access).

Present procedure at this step of tracing on loading is performed in iteration way with constant external loading since such a replacement of properties results in redistribution of loads in adjacent finite elements. The case when replacement procedure in the given finite element leads during the next iteration to the replacements in the adjacent elements up to «spontaneous fracture» (when replacement procedure covers large volume of considered structure at specified loading) is quite natural at that. Corresponding conditions for coming of such a state are considered as macroconditions of coming of the limiting state.

Described approach is to be applied to steel pressure vessel with defect overall dimensions $s \times c \times a$ (Figure 1), where s — dimension along the generatrix; c — along the circumference; a — same to depth of the wall in which the thinning was found. Elastic characteristics of steel E and ν, yield strength σ_y and index of power strain hardening m are known.

Estimation of limiting pressure P_{lim}, at which macroscopic spontaneous fracture of the wall takes place in zone of thinning, is necessary under conditions of three-axial stressed state with internal pressure P.

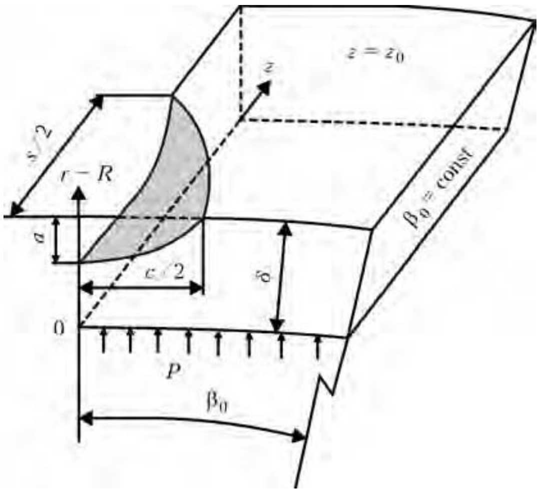

Figure 1. Scheme of fragment of pipe casing with defect of thinning being loaded by internal pressure P on the surface $r - R = 0$ and nominal stresses $\sigma_{\beta\beta}$, $\sigma_{\beta z}$ in plain $\beta = \beta_0$ and σ_{zz}, σ_{zr} in plain $z = z_0$ and symmetry conditions $\beta = 0$, $z = 0$

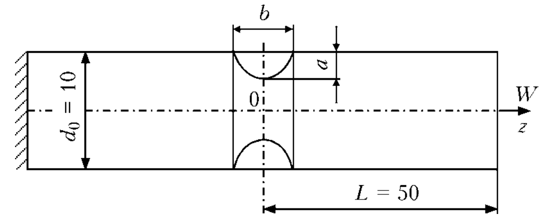

Figure 2. Scheme of axisymmetric notched cylinder specimen of $a \times b$ dimensions

Algorithm of numerical determination in scope of 3D stress-strain state in zone of considered defect taking no account to porosity is given in work [6]. The latter was considered in this work using equations (1)–(14).

Necessary data for such a model connected with specified steel are proposed to be determined using simple tensile experiments of axisymmetric notched cylinder specimens (Figure 2) from pipe steel with yield strength $\sigma_y \approx 480$ MPa. Two dimensions of notch in 10 mm diameter specimens were considered. The first is $a \times b = 1 \times 3$ and the second is $a \times b = 3 \times 1$ mm at theoretical concentration factors $\alpha_{\rm theor} = 1.60$ and 3.45.

$\sigma_{zz}^{\rm lim} = 500$ and 130 MPa are the corresponding average fracture axial stresses on clamps. For these data the process of loading of the specimens was simulated at different variation of initial data (Table 1) responsible for pore formation (Figure 3). At that variants 1–10 correspond to predetermined loading on the clamps (section $z = L$) and variant 11 — to predetermined value of axial movement $W = \Delta W n$, where n is the loading step.

Table 1. Variants of initial data responsible for pore formation

Number of variant	σ_y, MPa	ρ_V	S_c, MPa	m
1	480	0.07	1000	0.14
2	480	0.05	1000	0.14
3	480	0.03	1000	0.14
4	480	0	1000	0.14
5	400	0.05	1000	0.14
6	300	0.05	1000	0.14
7	480	0.05	1000	0.05
8	480	0.05	1000	0.25
9	480	0.05	700	0.14
10	480	0.05	1500	0.14
11	480	0.05	1000	0.14

Note. $(\varepsilon_i^p)_0 = 0.01$.

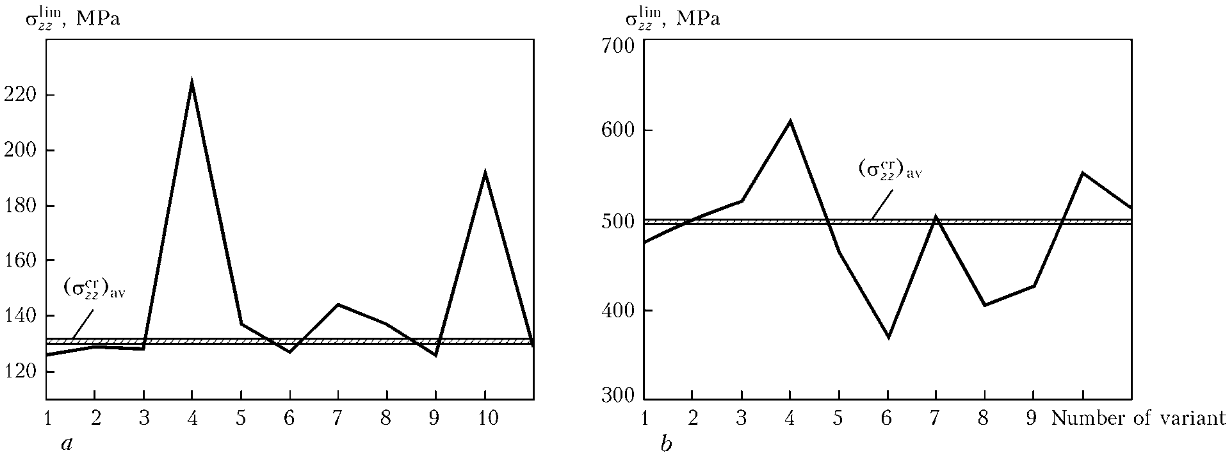

Figure 3. Results of computer simulation of the nominal limiting stresses $\sigma_{zz}^{\rm lim}$ in section $z = L$ and spontaneous fracture in section $z = 0$ of notched specimen of $a \times b = 3 \times 1$ (a) and 1×3 (b) dimensions ($\alpha_{\rm theor} = 3.45$) for different variants of change of σ_y, ρ_V, S_c, m (Table 1) in comparison with experimental data on $(\sigma_{zz}^{\rm cr})_{\rm av}$ (σ_{zz} is set at $z = L$ for variants 1–10; increment $\Delta W = 0.00261$ mm is set per each step for variant 11)

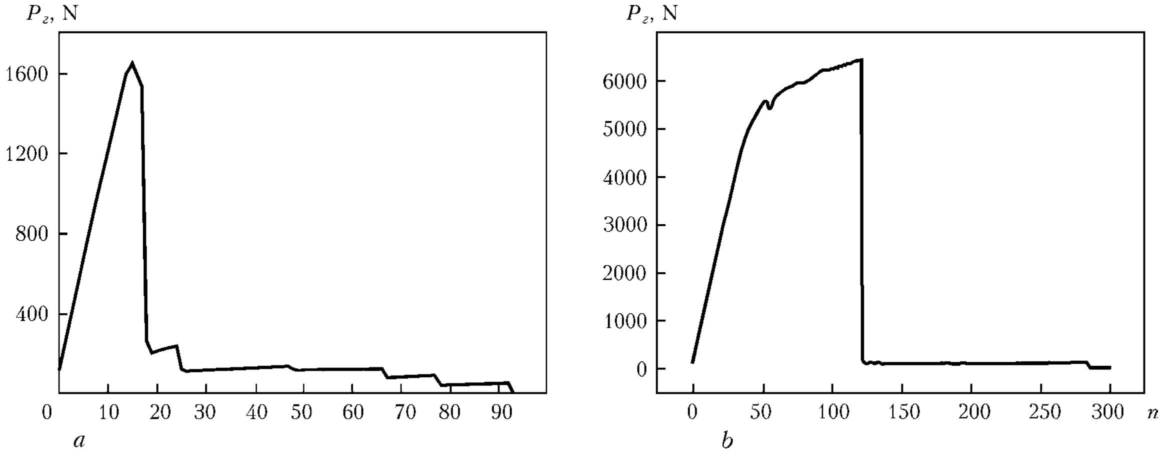

Figure 4. Results of simulation of load P_z on the edge $z = L = 50$ mm for notched specimen of $a \times b = 3 \times 1$ (a) and 1×3 (b) mm dimensions depending on step n at $\Delta W = 0.00261$ mm

Table 2. Initial and calculation data for considered wall thinning defects ($c = 40$ mm, $a = 14$ mm)

Number of variant	s, mm	$[P]$, MPa	P_{lim}, MPa	n_{saf}
1	66	7.50	18.8	2.5
2	100	5.15	17.4	3.3
3	200	4.15	14.0	3.2

For this case Figure 4 shows the kinetics of load change P_z in the process of n value growth up to coming of spontaneous fracture (without further increase of load P_z).

Correlation of σ_{zz}^{lim} value with specified average value shows that taking no account to porosity (variant 4 in Figure 3) provides conservative values of σ_{zz}^{lim}. At the same time reduction of σ_{y} below 300 MPa or S_{c} below 700 MPa as well as increase of m significantly reduce σ_{zz}^{lim} value. Change of porosity ρ_V (the main factor of fracture zone embrittlement) in the range of $\rho_V \approx$ ≈ 0.03–0.07 provides insignificant effect on σ_{zz}^{lim} critical value.

Fracture process taking into account pore formation which promotes embrittlement of the fracture zone has sufficiently high resistance to main parameters of the considered model (ρ_V, S_{c}, σ_{y}, m) for steel under study from this analysis. This allows using their approximate values for practical estimations.

$\rho_V = 0.05$, $S_{\text{c}} = 1000$ MPa, $\sigma_{\text{y}} = 440$ MPa, $m = 0.14$ and $(\varepsilon_i^p)_0 = 0.01$ were used in accordance with indicated for determination of critical load in the zone of local thinning of the wall of casing of $2R = 1420$ mm diameter pipe at wall thickness $\delta = 20$ mm from steel under consideration at 3D analysis.

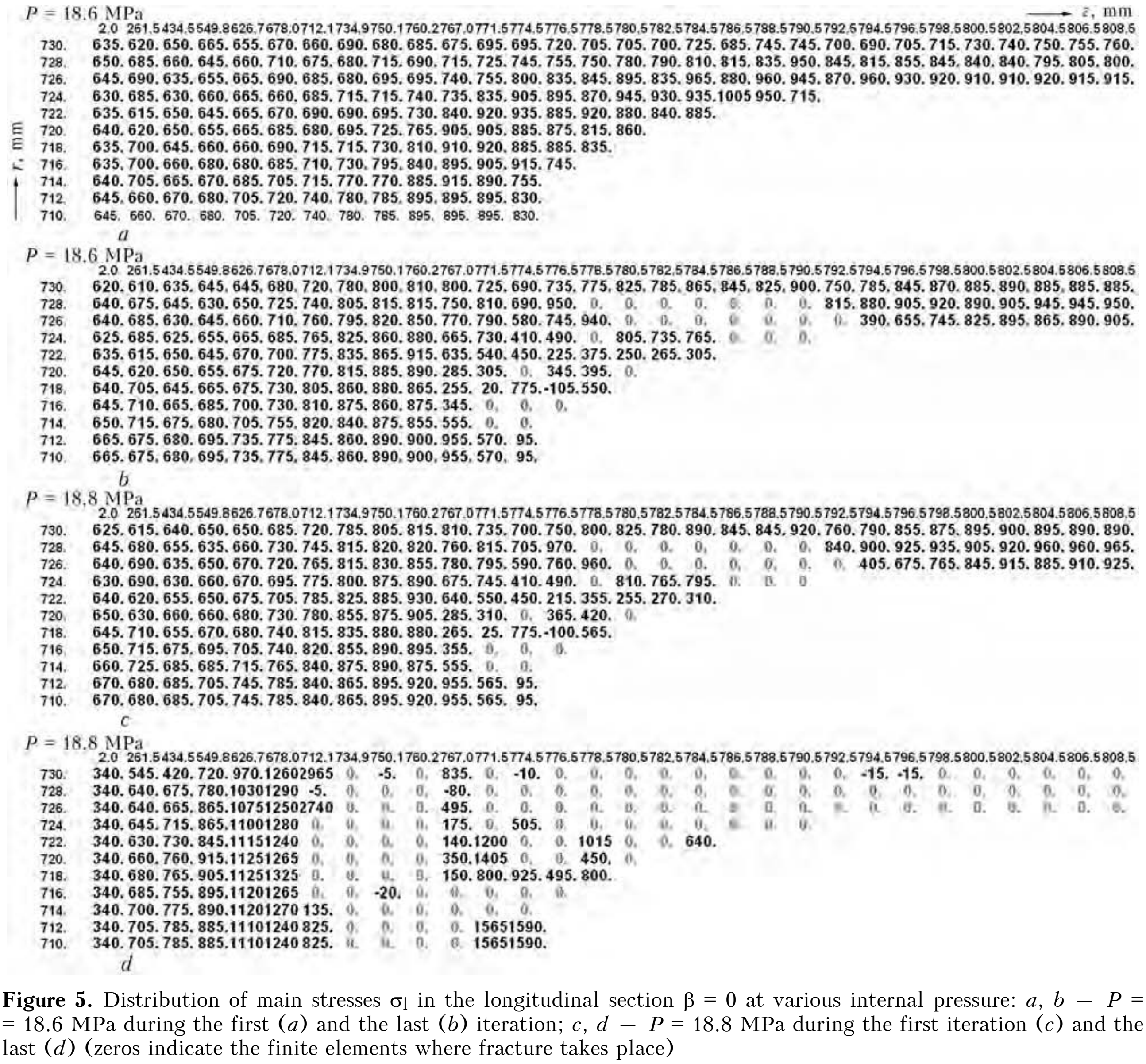
z, mm
r, mm
a
b
c
d

P = 18.6 MPa

```
        2.0  261.5434.5549.8626.7678.0712.1734.9750.1760.2767.0771.5774.5776.5778.5780.5782.5784.5786.5788.5790.5792.5794.5796.5798.5800.5802.5804.5806.5808.5
 730.   635. 620. 650. 665. 655. 670. 660. 690. 680. 685. 675. 695. 695. 720. 705. 705. 700. 725. 685. 745. 745. 700. 690. 705. 715. 730. 740. 750. 755. 760.
 728.   650. 685. 660. 645. 660. 710. 675. 680. 715. 690. 715. 725. 745. 755. 750. 780. 790. 810. 815. 835. 950. 845. 815. 855. 845. 840. 840. 795. 805. 800.
 726.   645. 690. 635. 655. 665. 690. 685. 680. 695. 695. 740. 755. 800. 835. 845. 895. 835. 965. 880. 960. 945. 870. 960. 930. 920. 910. 910. 920. 915. 915.
 724.   630. 685. 630. 660. 665. 660. 685. 715. 715. 740. 735. 835. 905. 895. 870. 945. 930. 935.1005 950. 715.
 722.   635. 615. 650. 645. 665. 670. 690. 690. 695. 730. 840. 920. 935. 885. 920. 880. 840. 885.
 720.   640. 620. 650. 655. 665. 685. 680. 695. 725. 765. 905. 905. 885. 875. 815. 860.
 718.   635. 700. 645. 660. 660. 690. 715. 715. 730. 810. 910. 920. 885. 885. 835.
 716.   635. 700. 660. 680. 680. 685. 710. 730. 795. 840. 895. 905. 915. 745.
 714.   640. 705. 665. 670. 685. 705. 715. 770. 770. 885. 915. 890. 755.
 712.   645. 660. 670. 680. 705. 720. 740. 780. 785. 895. 895. 895. 830.
 710.   645. 660. 670. 680. 705. 720. 740. 780. 785. 895. 895. 895. 830.
```

a

P = 18.6 MPa

```
        2.0  261.5434.5549.8626.7678.0712.1734.9750.1760.2767.0771.5774.5776.5778.5780.5782.5784.5786.5788.5790.5792.5794.5796.5798.5800.5802.5804.5806.5808.5
 730.   620. 610. 635. 645. 645. 680. 720. 780. 800. 810. 800. 725. 690. 735. 775. 825. 785. 865. 845. 825. 900. 750. 785. 845. 870. 885. 890. 885. 885. 885.
 728.   640. 675. 645. 630. 650. 725. 740. 805. 815. 815. 750. 810. 690. 950.   0.   0.   0.   0.   0.   0.   0. 815. 880. 905. 920. 890. 905. 945. 945. 950.
 726.   640. 685. 630. 645. 660. 710. 760. 795. 820. 850. 770. 790. 580. 745. 940.   0.   0.   0.   0.   0.   0.   0. 390. 655. 745. 825. 895. 865. 890. 905.
 724.   625. 685. 625. 655. 665. 685. 765. 825. 860. 880. 665. 730. 410. 490.   0. 805. 735. 765.   0.   0.   0.
 722.   635. 615. 650. 645. 670. 700. 775. 835. 865. 915. 635. 540. 450. 225. 375. 250. 265. 305.
 720.   645. 620. 650. 655. 675. 720. 770. 815. 885. 890. 285. 305.   0. 345. 395.   0.
 718.   640. 705. 645. 665. 675. 730. 805. 860. 880. 865. 255.  20. 775.-105. 550.
 716.   645. 710. 665. 685. 700. 730. 810. 875. 860. 875. 345.   0.   0.   0.
 714.   650. 715. 675. 680. 705. 755. 820. 840. 875. 855. 555.   0.   0.
 712.   665. 675. 680. 695. 735. 775. 845. 860. 890. 900. 955. 570.  95.
 710.   665. 675. 680. 695. 735. 775. 845. 860. 890. 900. 955. 570.  95.
```

b

P = 18.8 MPa

```
        2.0  261.5434.5549.8626.7678.0712.1734.9750.1760.2767.0771.5774.5776.5778.5780.5782.5784.5786.5788.5790.5792.5794.5796.5798.5800.5802.5804.5806.5808.5
 730.   625. 615. 640. 650. 650. 685. 720. 785. 805. 815. 810. 735. 700. 750. 800. 825. 780. 890. 845. 845. 920. 760. 790. 855. 875. 895. 900. 895. 890. 890.
 728.   645. 680. 655. 635. 660. 730. 745. 815. 820. 820. 760. 815. 705. 970.   0.   0.   0.   0.   0.   0.   0. 840. 900. 925. 935. 905. 920. 960. 960. 965.
 726.   640. 690. 635. 650. 670. 720. 765. 815. 830. 855. 780. 795. 590. 760. 960.   0.   0.   0.   0.   0.   0.   0. 405. 675. 765. 845. 915. 885. 910. 925.
 724.   630. 690. 630. 660. 670. 695. 775. 800. 875. 890. 675. 745. 410. 490.   0. 810. 765. 795.   0.   0.   0
 722.   640. 620. 655. 650. 675. 705. 785. 825. 885. 930. 640. 550. 450. 215. 355. 255. 270. 310.
 720.   650. 630. 660. 660. 680. 730. 780. 855. 875. 905. 285. 310.   0. 365. 420.   0.
 718.   645. 710. 655. 670. 680. 740. 815. 835. 880. 880. 265.  25. 775.-100. 565.
 716.   650. 715. 675. 695. 705. 740. 820. 855. 890. 895. 355.   0.   0.   0.
 714.   660. 725. 685. 685. 715. 765. 840. 875. 890. 875. 555.   0.   0.
 712.   670. 680. 685. 705. 745. 785. 840. 865. 895. 920. 955. 565.  95.
 710.   670. 680. 685. 705. 745. 785. 840. 865. 895. 920. 955. 565.  95.
```

c

P = 18.8 MPa

```
        2.0  261.5434.5549.8626.7678.0712.1734.9750.1760.2767.0771.5774.5776.5778.5780.5782.5784.5786.5788.5790.5792.5794.5796.5798.5800.5802.5804.5806.5808.5
 730.   340. 545. 420. 720. 970.12602965   0.  -5.   0. 835.   0. -10.   0.   0.   0.   0.   0.   0.   0.   0.   0. -15. -15.   0.   0.   0.   0.   0.   0.
 728.   340. 640. 675. 780.10301290  -5.   0.   0.   0. -80.   0.   0.   0.   0.   0.   0.   0.   0.   0.   0.   0.   0.   0.   0.   0.   0.   0.   0.   0.
 726.   340. 640. 665. 865.107512502740   0.   0.   0. 495.   0.   0.   0.   0.   0.   0.   0.   0.   0.   0.   0.   0.   0.   0.   0.   0.   0.   0.   0.
 724.   340. 645. 715. 865.11001280   0.   0.   0.   0. 175.   0. 505.   0.   0.   0.   0.   0.   0.   0.   0.
 722.   340. 630. 730. 845.11151240   0.   0.   0.   0. 140.1200   0.   0. 1015   0.   0. 640.
 720.   340. 660. 760. 915.11251265   0.   0.   0.   0. 350.1405   0.   0. 450.   0.
 718.   340. 680. 765. 905.11251325   0.   0.   0.   0. 150. 800. 925. 495. 800.
 716.   340. 685. 755. 895.11201265   0.   0. -20.   0.   0.   0.   0.   0.
 714.   340. 700. 775. 890.11201270 135.   0.   0.   0.   0.   0.   0.
 712.   340. 705. 785. 885.11101240 825.   0.   0.   0.   0. 15651590.
 710.   340. 705. 785. 885.11101240 825.   0.   0.   0.   0. 15651590.
```

d

Figure 5. Distribution of main stresses σ_{I} in the longitudinal section $\beta = 0$ at various internal pressure: *a*, *b* — $P =$ $= 18.6$ MPa during the first (*a*) and the last (*b*) iteration; *c*, *d* — $P = 18.8$ MPa during the first iteration (*c*) and the last (*d*) (zeros indicate the finite elements where fracture takes place)

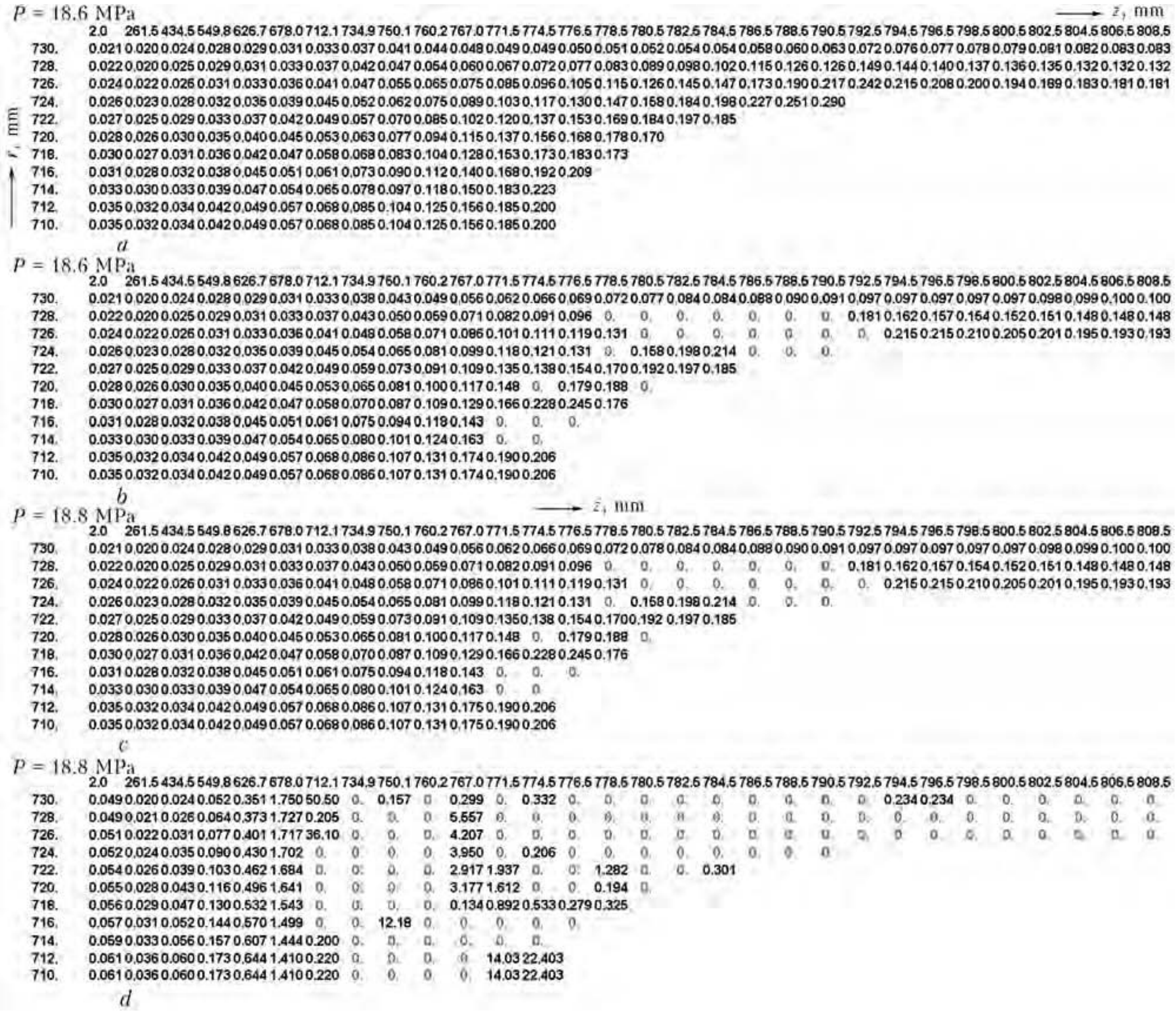

$P = 18.6$ MPa

	2.0	261.5	434.5	549.8	626.7	678.0	712.1	734.9	750.1	760.2	767.0	771.5	774.5	776.5	778.5	780.5	782.5	784.5	786.5	788.5	790.5	792.5	794.5	796.5	798.5	800.5	802.5	804.5	806.5	808.5
730.	0.021	0.020	0.024	0.028	0.029	0.031	0.033	0.037	0.041	0.044	0.048	0.049	0.049	0.050	0.051	0.052	0.054	0.054	0.058	0.060	0.063	0.072	0.076	0.077	0.078	0.079	0.081	0.082	0.083	0.083
728.	0.022	0.020	0.025	0.029	0.031	0.033	0.037	0.042	0.047	0.054	0.060	0.067	0.072	0.077	0.083	0.089	0.098	0.102	0.115	0.126	0.126	0.149	0.144	0.140	0.137	0.136	0.135	0.132	0.132	0.132
726.	0.024	0.022	0.026	0.031	0.033	0.036	0.041	0.047	0.055	0.065	0.075	0.085	0.096	0.105	0.115	0.126	0.145	0.147	0.173	0.190	0.217	0.242	0.216	0.208	0.200	0.194	0.189	0.183	0.181	0.181
724.	0.026	0.023	0.028	0.032	0.035	0.039	0.045	0.052	0.062	0.075	0.089	0.103	0.117	0.130	0.147	0.158	0.184	0.198	0.227	0.251	0.290									
722.	0.027	0.025	0.029	0.033	0.037	0.042	0.049	0.057	0.070	0.085	0.102	0.120	0.137	0.153	0.169	0.184	0.197	0.185												
720.	0.028	0.026	0.030	0.035	0.040	0.045	0.053	0.063	0.077	0.094	0.115	0.137	0.156	0.168	0.178	0.170														
718.	0.030	0.027	0.031	0.036	0.042	0.047	0.058	0.068	0.083	0.104	0.128	0.153	0.173	0.183	0.173															
716.	0.031	0.028	0.032	0.038	0.045	0.051	0.061	0.073	0.090	0.112	0.140	0.168	0.192	0.209																
714.	0.033	0.030	0.033	0.039	0.047	0.054	0.065	0.078	0.097	0.118	0.150	0.183	0.223																	
712.	0.035	0.032	0.034	0.042	0.049	0.057	0.068	0.085	0.104	0.125	0.156	0.185	0.200																	
710.	0.035	0.032	0.034	0.042	0.049	0.057	0.068	0.085	0.104	0.125	0.156	0.185	0.200																	

a

$P = 18.6$ MPa

	2.0	261.5	434.5	549.8	626.7	678.0	712.1	734.9	750.1	760.2	767.0	771.5	774.5	776.5	778.5	780.5	782.5	784.5	786.5	788.5	790.5	792.5	794.5	796.5	798.5	800.5	802.5	804.5	806.5	808.5
730.	0.021	0.020	0.024	0.028	0.029	0.031	0.033	0.038	0.043	0.049	0.056	0.062	0.066	0.069	0.072	0.077	0.084	0.084	0.088	0.090	0.091	0.097	0.097	0.097	0.097	0.097	0.098	0.099	0.100	0.100
728.	0.022	0.020	0.025	0.029	0.031	0.033	0.037	0.043	0.050	0.059	0.071	0.082	0.091	0.096	0.	0.	0.	0.	0.	0.	0.	0.181	0.162	0.157	0.154	0.152	0.151	0.148	0.148	0.148
726.	0.024	0.022	0.026	0.031	0.033	0.036	0.041	0.048	0.058	0.071	0.086	0.101	0.111	0.119	0.131	0.	0.	0.	0.	0.	0.	0.	0.215	0.215	0.210	0.205	0.201	0.195	0.193	0.193
724.	0.026	0.023	0.028	0.032	0.035	0.039	0.045	0.054	0.065	0.081	0.099	0.118	0.121	0.131	0.	0.158	0.198	0.214	0.	0.	0.									
722.	0.027	0.025	0.029	0.033	0.037	0.042	0.049	0.059	0.073	0.091	0.109	0.135	0.138	0.154	0.170	0.192	0.197	0.185												
720.	0.028	0.026	0.030	0.035	0.040	0.045	0.053	0.065	0.081	0.100	0.117	0.148	0.	0.179	0.188	0.														
718.	0.030	0.027	0.031	0.036	0.042	0.047	0.058	0.070	0.087	0.109	0.129	0.166	0.228	0.245	0.176															
716.	0.031	0.028	0.032	0.038	0.045	0.051	0.061	0.075	0.094	0.118	0.143	0.	0.	0.																
714.	0.033	0.030	0.033	0.039	0.047	0.054	0.065	0.080	0.101	0.124	0.163	0.	0.																	
712.	0.035	0.032	0.034	0.042	0.049	0.057	0.068	0.086	0.107	0.131	0.174	0.190	0.206																	
710.	0.035	0.032	0.034	0.042	0.049	0.057	0.068	0.086	0.107	0.131	0.174	0.190	0.206																	

b

$P = 18.8$ MPa

	2.0	261.5	434.5	549.8	626.7	678.0	712.1	734.9	750.1	760.2	767.0	771.5	774.5	776.5	778.5	780.5	782.5	784.5	786.5	788.5	790.5	792.5	794.5	796.5	798.5	800.5	802.5	804.5	806.5	808.5
730.	0.021	0.020	0.024	0.028	0.029	0.031	0.033	0.038	0.043	0.049	0.056	0.062	0.066	0.069	0.072	0.078	0.084	0.084	0.088	0.090	0.091	0.097	0.097	0.097	0.097	0.097	0.098	0.099	0.100	0.100
728.	0.022	0.020	0.025	0.029	0.031	0.033	0.037	0.043	0.050	0.059	0.071	0.082	0.091	0.096	0.	0.	0.	0.	0.	0.	0.	0.181	0.162	0.157	0.154	0.152	0.151	0.148	0.148	0.148
726.	0.024	0.022	0.026	0.031	0.033	0.036	0.041	0.048	0.058	0.071	0.086	0.101	0.111	0.119	0.131	0.	0.	0.	0.	0.	0.	0.	0.215	0.215	0.210	0.205	0.201	0.195	0.193	0.193
724.	0.026	0.023	0.028	0.032	0.035	0.039	0.045	0.054	0.065	0.081	0.099	0.118	0.121	0.131	0.	0.158	0.198	0.214	0.	0.	0.									
722.	0.027	0.025	0.029	0.033	0.037	0.042	0.049	0.059	0.073	0.091	0.109	0.135	0.138	0.154	0.170	0.192	0.197	0.185												
720.	0.028	0.026	0.030	0.035	0.040	0.045	0.053	0.065	0.081	0.100	0.117	0.148	0.	0.179	0.188	0.														
718.	0.030	0.027	0.031	0.036	0.042	0.047	0.058	0.070	0.087	0.109	0.129	0.166	0.228	0.245	0.176															
716.	0.031	0.028	0.032	0.038	0.045	0.051	0.061	0.075	0.094	0.118	0.143	0.	0.	0.																
714.	0.033	0.030	0.033	0.039	0.047	0.054	0.065	0.080	0.101	0.124	0.163	0	0																	
712.	0.035	0.032	0.034	0.042	0.049	0.057	0.068	0.086	0.107	0.131	0.175	0.190	0.206																	
710.	0.035	0.032	0.034	0.042	0.049	0.057	0.068	0.086	0.107	0.131	0.175	0.190	0.206																	

c

$P = 18.8$ MPa

	2.0	261.5	434.5	549.8	626.7	678.0	712.1	734.9	750.1	760.2	767.0	771.5	774.5	776.5	778.5	780.5	782.5	784.5	786.5	788.5	790.5	792.5	794.5	796.5	798.5	800.5	802.5	804.5	806.5	808.5
730.	0.049	0.020	0.024	0.052	0.351	1.750	50.50	0.	0.157	0	0.299	0.	0.332	0.	0.	0.	0.	0.	0.	0.	0.	0	0.234	0.234	0.	0.	0.	0.	0.	0.
728.	0.049	0.021	0.026	0.064	0.373	1.727	0.205	0.	0.	0	5.557	0.	0.	0.	0.	0.	0.	0.	0.	0.	0.	0.	0.	0.	0.	0.	0.	0.	0.	0.
726.	0.051	0.022	0.031	0.077	0.401	1.717	36.10	0.	0.	0.	4.207	0.	0.	0.	0.	0.	0.	0.	0.	0.	0.	0.	0	0.	0.	0.	0.	0.	0.	0.
724.	0.052	0.024	0.035	0.090	0.430	1.702	0.	0	0.	0	3.950	0.	0.206	0	0.	0.	0.	0.	0.	0.	0.									
722.	0.054	0.026	0.039	0.103	0.462	1.684	0.	0.	0.	0.	2.917	1.937	0.	0.	1.282	0.	0.	0.301												
720.	0.055	0.028	0.043	0.116	0.496	1.641	0.	0.	0.	0.	3.177	1.612	0	0.	0.194	0.														
718.	0.056	0.029	0.047	0.130	0.532	1.543	0.	0.	0.	0.	0.134	0.892	0.533	0.279	0.325															
716.	0.057	0.031	0.052	0.144	0.570	1.499	0.	0.	12.18	0.	0	0.	0.	0																
714.	0.059	0.033	0.056	0.157	0.607	1.444	0.200	0.	0.	0.	0.	0.	0.																	
712.	0.061	0.036	0.060	0.173	0.644	1.410	0.220	0.	0.	0.	0	14.03	22.403																	
710.	0.061	0.036	0.060	0.173	0.644	1.410	0.220	0.	0.	0	0.	14.03	22.403																	

d

Figure 6. The same as in Figure 5 but for $\kappa_k = \int d\varepsilon_i^p = \sum (d\varepsilon_i^p)^{(k)}$ value

Three variants of geometrical defects from Table 2 were studied. The Table shows the results of calculation of allowable pressures $[P]$ for considered thinning defects. Figures 5 and 6 illustrate the result of calculation of the limiting pressure at which spontaneous fracture takes place for variant 1. Similar data are given for variants 2 and 3. Respectively, Table 2 also shows information about limiting $P_{\rm lim}$ and safety factors $n_{\rm saf} = P_{\rm lim}/[P]$.

Matching of calculation limiting loads on the results of given work, i.e. considering pore formation, with calculation allowable loads from work [7], obtained based on broad experiment, related with fracture of full-scale specimens through the safety factor in the range of $n_{\rm saf} = 2.0$–2.5, shows their good compliance.

CONCLUSIONS

1. Mathematical modelling of the limiting state for steel pressure vessels involving geometrical defects of wall thinning requires more general models for description of not only deformation process (for example, considering larger deformation), but fracture process as well after developed plastic flow stage (for example, pore formation).

2. It is shown that the attraction of sufficiently known physical models of pore formation at plastic flow results in certain «embrittlement» effect of fracture zone at that sufficiently reducing the limiting calculation loading (per 20–70 % and more).

3. The results of matching of limiting calculation loads from Table 2 on procedure of this study with that allowable on work [7] based on the broad experiment show that the safety factor $n_{\rm saf} \approx 2.0$–2.5 specified at that has good enough correspondence with data of Table 2 as a rule.

1. Romanova, V.A. (2008) *Modeling of deformation and fracture processes in three-dimensional structur-*

ally heterogeneous materials*: Syn. of Thesis for Dr. of Techn. Sci. Degree. Tomsk.

2. Karzov, G.P., Margolin, B.Z., Shvetsova, V.A. (1993) *Physical-mechanical modeling of fracture processes*. St.-Petersburg: Politekhnika.
3. Rybin, V.V. (1986) *High plastic strains and fracture of metals*. Moscow: Metallurgiya.
4. (1986) *Static strength and fracture mechanics of steels*. Ed. by V. Dal, V. Antonov. Moscow: Metallurgizdat.
5. Makhnenko, V.I. (1976) *Computational methods for investigation of kinetics of welding stresses and strains*. Kiev: Naukova Dumka.
6. Makhnenko, V.I., Velikoivanenko, O.A., Pozynka, G.P. et al. (2009) Stressed state in zone of thinning defects of thin-wall pipes. In: *Problems of service life and service safety of structures, buildings and machines*. Ed. by B.E. Paton. Kyiv: PWI.
7. (2000) *Fitness-for-service*: American Petroleum Institute recommended practice 579. 1st ed.

INFLUENCE OF WELDING THERMAL CYCLE ON STRUCTURE AND PROPERTIES OF MICROALLOYED STRUCTURAL STEELS

V.A. KOSTIN, G.M. GRIGORENKO, V.D. POZNYAKOV, S.L. ZHDANOV, T.G. SOLOMIJCHUK, T.A. ZUBER and **A.A. MAKSIMENKO**

E.O. Paton Electric Welding Institute, NASU, Kiev, Ukraine

Influence of welding thermal cycle on microstructure and properties of HAZ metal in new steels with carbide and carbonitride type of strengthening, namely 06GBD, 10G2FB, 15KSATYuD, was studied. It is shown that under the influence of welding thermal cycle an optimum complex of ferritic-bainitic structures forms in a rather broad range of cooling rates ($w_{6/5}$ = 10–30 °C/s), which is characterized by values of strength, ductility and cold resistance on the level of requirements made of base metal of strength class C440.

Keywords: *arc welding, structural steels, carbonitride strengthening, welding thermal cycle, Gleeble 3800, microstructure, bainite, MAC-phase, mechanical properties*

At present transportation engineering and building industry of Ukraine are the main users of higher strength steels with yield point of up to 400 MPa. Today, however, they no longer satisfy, by a number of objective factors, the requirements of high-speed traffic or modern concepts of urban planning, both by the level of strength and impact toughness.

Over the recent years, PWI in cooperation with metallurgists developed a number of new steels with 440–590 MPa yield point, based on the principle of carbide and carbonitride strengthening [1, 2].

As welding is the main technological process of fabrication of structures from these steels, improved performance of the new steels (by strength and impact toughness level) should be preserved also in the welded joints. However, HAZ formation in the metal being welded leads to deterioration of mechanical properties under the impact of welding thermal cycle (WTC), both as a result of grain growth, and in connection with formation of quenching structures. Wide introduction of new steels should be preceded by profound comprehensive investigation of these steels reaction to WTC.

Disembodied published data on the features of structural changes in the new steels with carbide and carbonitride strengthening under WTC conditions are obviously insufficient [3, 4].

In addition, the clearly increased requirements to impact toughness of new steels of strength class C345–440 (KCU_{-40} = 39 J/cm^2, KCU_{-70} = 34 J/cm^2 to GOST 27772–88) require studying WTC effect on strength and impact toughness levels in HAZ metal.

The objective of this work consisted in investigation of the features of formation of HAZ metal structure under WTC impact and assessment of microstructure influence on mechanical properties and impact toughness in this zone, in order to select optimum welding modes, ensuring high performance of the welded joint.

Table 1 gives the composition of the studied steel grades. Steels 10G2FB and 06GBD belong to steels with carbide strengthening type, and 15KhSATYuD steel is of carbonitride strengthening type. Mechanical properties of steels in as-delivered condition are given in Tables 2 and 3.

In order to evaluate WTC effect on the structure of welded joint HAZ metal, investigations were conducted on model samples in Geeble 3800

© V.A. KOSTIN, G.M. GRIGORENKO, V.D. POZNYAKOV, S.L. ZHDANOV, T.G. SOLOMIJCHUK, T.A. ZUBER and A.A. MAKSIMENKO, 2012

Table 1. Composition of studied steels, wt.%

Steel grade	C	Si	Mn	Cr	Ti	Nb
15KhSATYuD (δ = 12 mm, strength class C345 to GOST 27772–88)	0.145	1.12	0.76	0.56	0.03	–
10G2FB (δ = 18.7 mm, strength class K60 to TU 1381-009-47966425–2007)	0.079	0.25	1.57	0.04	–	0.05
06GBD (δ = 20 mm, strength class C390 to TU U 27.1-05416923-085:2006)	0.066	0.19	1.23	0.22	–	0.03

Table 1 (cont.)

Steel grade	Mo	Cu	V	Al	N	S	P
15KhSATYuD (δ = 12 mm, strength class C345 to GOST 27772–88)	–	0.31	–	0.041	0.015	0.029	0.026
10G2FB (δ = 18.7 mm, strength class K60 to TU 1381-009-47966425–2007)	0.19	≤0.02	0.05	0.032	0.006	0.007	0.013
06GBD (δ = 20 mm, strength class C390 to TU U 27.1-05416923-085:2006)	0.13	0.22	–	–	0.006	0.009	0.010

system for simulation of welding thermodeformational cycle. For this purpose samples of 6 mm diameter and 86 mm length were heated in a high-speed dilatometer up to the temperature of 1350 °C at the rate of 150 °C/s. After that they were cooled in keeping with the specified thermal cycles, characteristic for basic modes of arc welding of the studied steels at rate $w_{6/5}$ varying from 1 up to 60 °C/s. Dylatometric study results were used to plot diagrams of decomposition of austenite in the studied steels (Figure 1). WTC effect on mechanical properties and impact toughness of the studied steels was assessed by heat treatment of model samples in MSR-75 unit by a procedure developed at PWI [5].

Processing of the results of dylatometric analysis and diagram plotting were performed by the common procedure. Calculation of the ratio of transformation products was conducted by dylatometric curves, using segment approach [6].

Metallographic investigations were conducted using light microscope «Neophot-32». Microstructure was revealed by etching in nital (4 % solution of nitric acid in alcohol). Hardness was measured by Vickers at 50 N load. Structural constituents were calculated by field method to GOST 8233–56.

Microstructural analysis showed that 15KhSATYuD steel in the initial condition has ferritic-pearlitic structure of various dispersity, with varying amount of pearlite and pronounced striation (Figure 2, *a*). Grain size corresponds to point 4 (71–97 μm). Metal of this steel contains a large quantity of nonmetallic inclusions, predominantly manganese sulphides, which are located in ferrite regions.

Table 2. Mechanical properties of studied steels

Steel grade	Along rolling direction				Across rolling direction			
	σ_y, MPa	σ_t, MPa	δ_5, %	ψ, %	σ_y, MPa	σ_t, MPa	δ_5, %	ψ, %
15KhSATYuD	411	564	33.1	64.5	407	560	30.7	52.4
10G2FB	576	660	25.1	62.3	521	608	25.4	64.8
06GBD	400	578	30	84	–	–	–	–

Table 3. Results of impact bend testing of studied steels

Steel grade	Rolling direction	*KCU*, J/cm^2, at temperature, °C			*KCV*, J/cm^2, at temperature, °C		
		20	–40	–60	20	–40	–60
15KhSATYuD	Along	120	72	65	84	26	14
	Across	82	44	40	46	25	15
10G2FB	Along	346	347	324	344	346	345
	Across	345	279	220	323	256	204
06GBD	Along	348	348	–	349	317	–

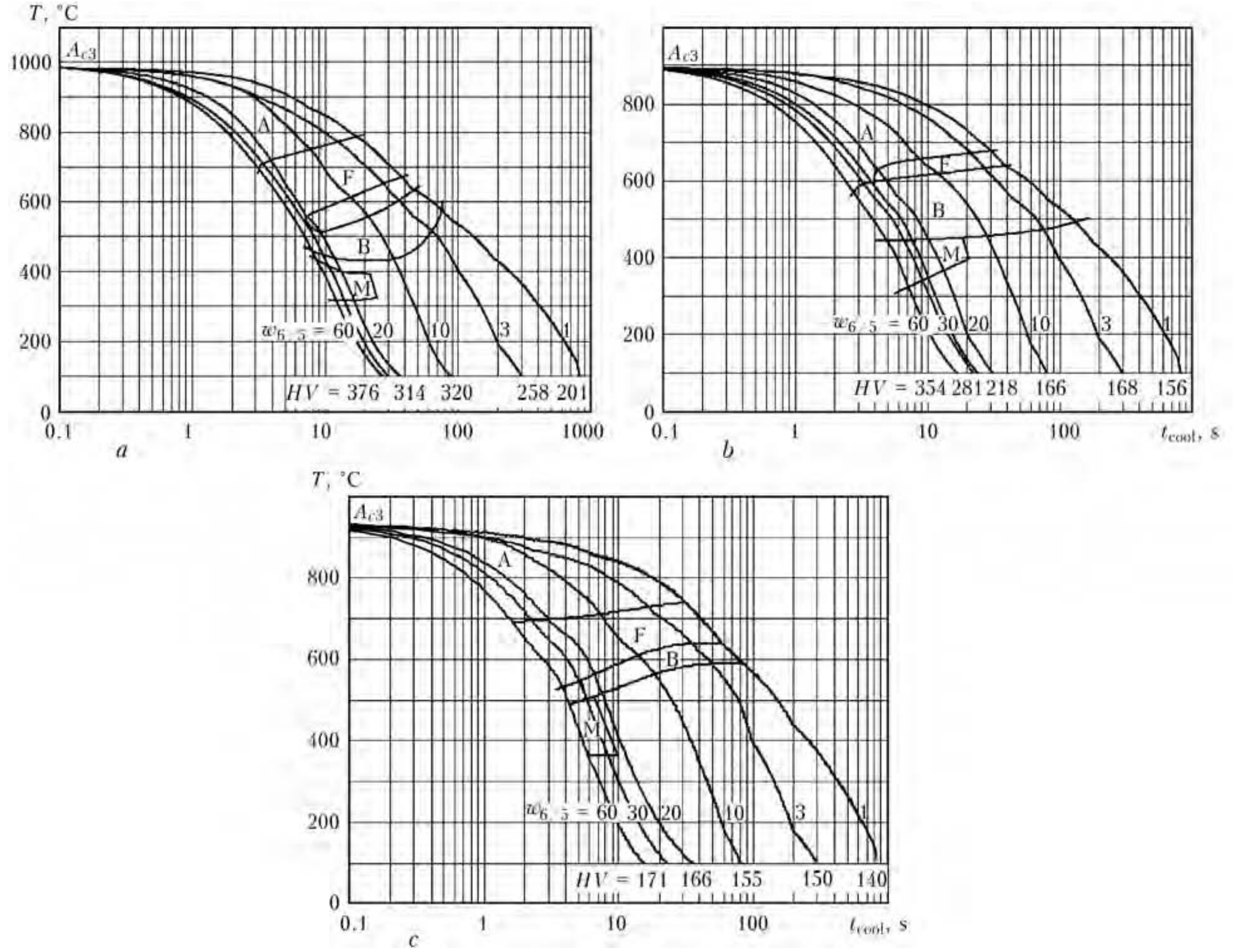

Figure 1. Thermokinetic diagram of austenite decomposition in steels with carbonitride strengthening: *a* — 15KhSATYuD; *b* — 10G2FB; *c* — 06GBD

Microstructure of samples of 10G2FB steel in as-delivered condition is ferritic-bainitic with a small amount of pearlite, obtained as a result of application of rolling stock thermostrengthening technology. Structure consists of sections of polygonal ferrite, tempered bainite and finely-dispersed pearlite (Figure 2, *b*). Grain point is 4–5. Steel 10G2FB is characterized by rolling stock texture and stringer anisometry.

Mictrostructure of samples of 06GBD steel is a finely-dispersed ferritic-pearlitic structure with grain size of 5–15 μm (Figure 2, *c*). A certain anisometry of ferrite grains is found, the dimensions of which correspond to point 4–6 (40–80 μm). Finely-dispersed pearlite is observed in the form of individual isolated sections along the boundaries and at the junction of ferrite grains. A small amount of carbon (0.06 %) and observed differences in pearlite colour allow assuming that individual sections (of lighter colour) are those of martensite-austenite-carbide complexes (MAC-phases). Rolling texture is completely absent from the structure.

Toughness of steels with carbonitride strengthening in as-delivered condition was evaluated on standard sample with U- and V-

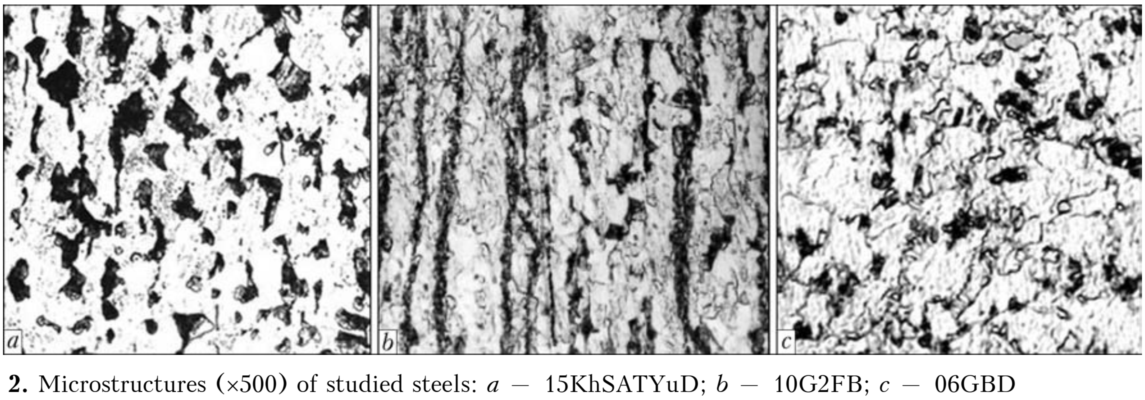

Figure 2. Microstructures (×500) of studied steels: *a* — 15KhSATYuD; *b* — 10G2FB; *c* — 06GBD

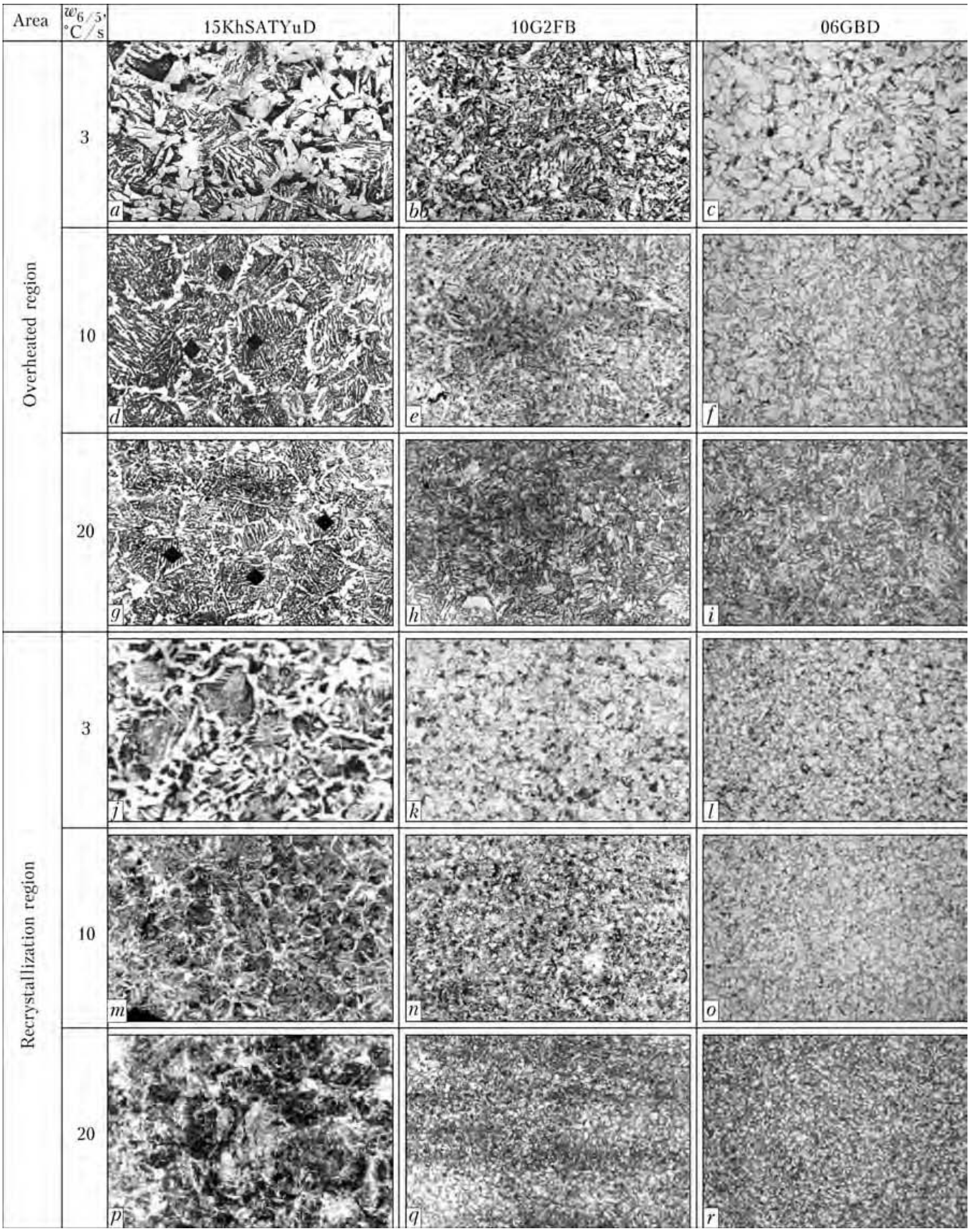

Figure 3. Influence of cooling rate on microstructure (×500) of simulated sections of HAZ metal in overheating and recrystallization zones (for *a*–*r* see the text)

shaped notch for impact bending according to GOST 9454–78. Obtained results are indicative of the fact that in 10G2FB and 06GBD steels toughness margin is much higher than in 15KhSATYuD steel, and brittle transition temperature is below –60 °C (Table 3).

Metallographic analysis of simulation samples of overheating zone from 15KhSATYuD steel showed that austenite transformation at their continuous cooling at the rate of 3 °C/s occurs in the ferritic, pearlitic and bainitic regions. Therefore, this steel structure contains quite a lot of ferrite (Figure 3, *a*). Hypoeutectoid ferrite of polygonal morphology precipitated along austenite grain boundaries, and sections of pealite precipitates are observed at the junction of ferrite grains and inside them. Widmanstatten ferrite is found locally. Inside the austenite grains of these steels the structure was identified as globular bainite. These structural changes lead

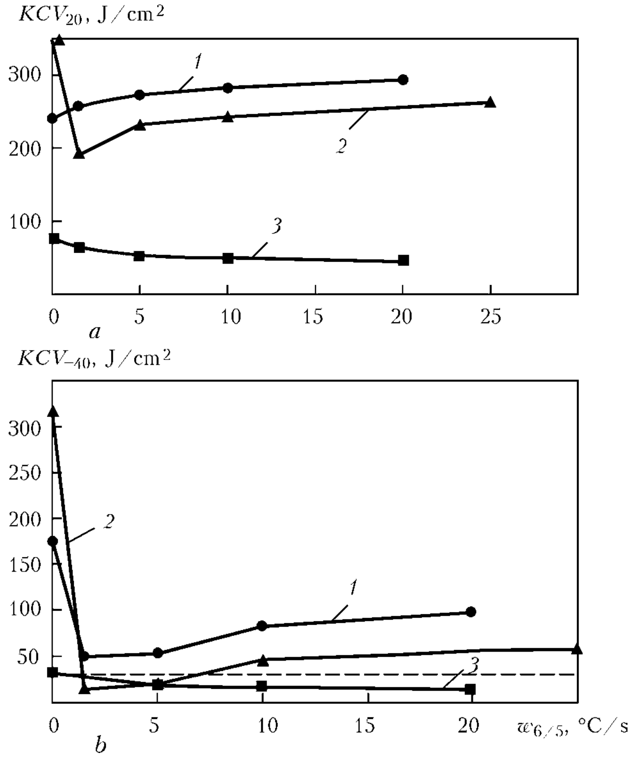

Figure 4. Dependence of impact toughness values KCV of HAZ metal on its cooling rate $w_{6/5}$ at 20 (*a*) and −40 (*b*) °C: *1* — 06GBD; *2* — 10G2FB; *3* — 15KhSATYuD (dash line — strength class C440)

to a monotonic lowering of ductility and impact toughness values at temperature below 0 °C.

The most coarse-grained structure formed in samples of 10G2FB steel at cooling at the rate of 3 °C/s (Figure 3, *b*). Hypoeutectoid polygonal ferrite and pearlite precipitate along the grain boundaries, and bainite of two morphological varieties: high-temperature (low-carbon) with microhardness of 1850–2030 MPa and low-temperature with microhardness of 2140–2430 MPa forms inside the grains. Such a structural change leads to an abrupt drop of HAZ metal cold resistance at temperature of −20 °C and lower (Figure 4), as well as increase of strength values (Figure 5) and lowering of values of relative elongation with a slight increase of values of reduction-in-area (Figure 6).

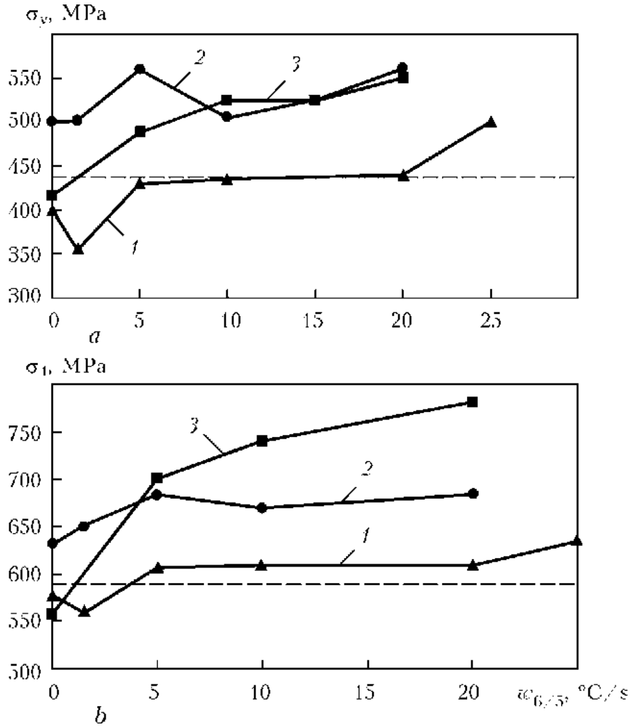

Figure 5. Dependence of strength properties (σ_y and σ_t) of HAZ metal on its cooling rate (designations are the same as in Figure 4)

In 06GBD steel an anisometric ferritic-bainitic structure is found at cooling at the rate of 3 °C/s (Figure 3, *c*). Bainite formation occurs in the sections with higher carbon content (former pearlite grain regions). Relatively coarse ferrite grains (point 8, about 20–22 μm) along the boundaries are surrounded by uniformly distributed finer bainitic grains (point 10, 10 μm). Bainite microhardness is equal to about 1820–1890 MPa.

With increase of cooling rate to 10° C/s the conditions for austenite homogenizing process become less favourable than at $w_{6/5}$ = 3 °C/s. In this connection in the structure of 15KhSATYuD steel the quantity of bainitic component rises abruptly, and quantity of structurally-free bainite and pearlite decreases abruptly (Figure 3, *d*, *m*), thus leading to higher values of HAZ metal strength and lowering of its ductility properties.

Structurally-free hypoeutectoid ferrite precipitates as a net along austenite grain bounda-

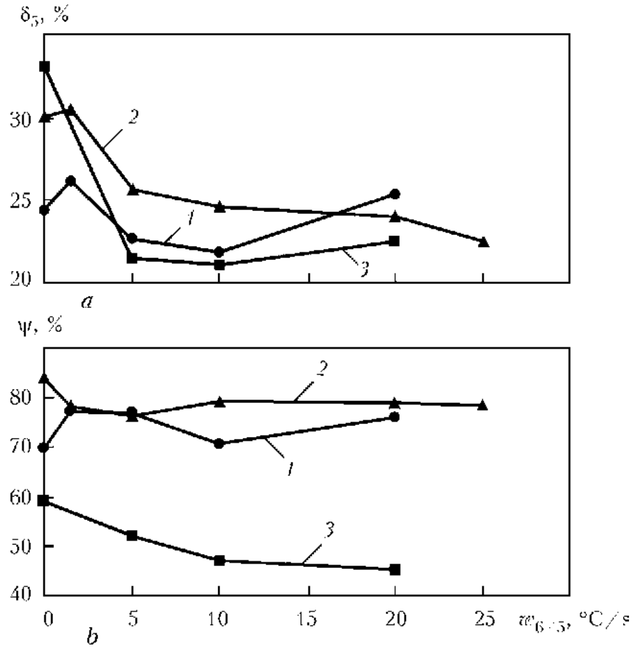

Figure 6. Dependence of ductility properties (δ_5 and ψ) of HAZ metal on its cooling rate (designations are the same as in Figure 4)

ries, whereas pearlite is sometimes found near ferrite grains. Bainite was identified as granular. Size of bainite grains at cooling rate $w_{6/5}$ = = 3 °C/s practically did not change.

Results of metallographic analysis of microstructure of simulation samples from steel 15KhSATYuD, formed at $w_{6/5}$ = 10 °C/s, are indicative of the fact that austenite overcooling becomes greater at increase of cooling rate that results in an increase of its resistance and lowering of transformation temperature of both ferrite from 800 to 750 °C, and bainite from 630 to 550 °C. Amount of bainitic constituent rises. Increase of the amount of bainite in the structure causes an increase of hardness in the complete recrystallization region, as well as of strength values. At the same time, ductility and impact toughness values (Figure 4) decrease.

Cooling of 10G2FB steel at the rate of 10 °C/s leads to narrowing of the region with overheated structure and grain refinement. Compared to cooling rate of 3 °C/s, structural changes in this case promote a reduction of the amount of hypoeutectoid polygonal ferrite and low-carbon bainite, and increase of the amount of high-carbon bainite (Figure 3, *e*, *n*). Pearlitic transformation at this rate is almost completely absent. Temperatures of ferrite and bainite transformation decrease to a smaller degree than in 15KhSATYuD steel. Such a nature of microstructure leads to a small increase of impact toughness values (see Figure 4), values of strength and reduction in area are on base metal level (Figures 5 and 6), whereas values of relative elongation decreased to 21 % (Figure 6).

Results of metallographic analysis of 06GBD steel formed at $w_{6/5}$ = 10 °C/s show that it consists of ferrite, bainite and small regions of MAC-phase precipitates (about 1 %, Table 4).

Bainite grains are observed in the form of elongated plates of upper bainite, formed both along ferrite grain boundaries, and of preserved equiaxed regions of granular bainite (Figure 3, *f*, *o*) With increase of cooling rate to $w_{6/5}$ = = 10 °C/s, microhardness of bainitic structure rises up to 2190 MPa, mainly due to increase of the quantity of its high-temperature species. MAC-phase distribution in the structure is uniform. Change of phase transformation temperature turns out to be negligible (lowering by approximately 20–30 °C).

Analysis of microstructure of simulation samples from 15KhSATYuD steel formed as a result of cooling at the rate of $w_{6/5}$ = 20 °C/s (Figure 3, *g*, *p*) showed a complex combination of bainite of granular and plate-like morphology, as well as hypoeutectoid ferrite and a small quantity of acicular ferrite. Bainite microhardness changes from 2150–2200 (for granular bainite) to 1930–1980 MPa (for plate-like bainite).

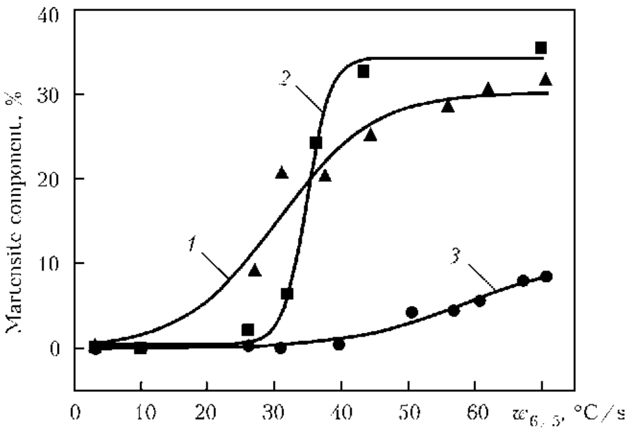

Figure 7. Influence of cooling rate on fraction of martensite component in the studied steels: *1* — 15KhSATYuD; *2* — 10G2FB; *3* — 06GBD

Microstructure of samples from steel 10G2FB formed as a result of cooling at the rate of $w_{6/5}$ = = 20 °C/s revealed further narrowing of the region simulating the overheating zone, at reduction of grain size. In the simulated region structure hypoeutectoid polygonal ferrite is seldom found along grain boundaries. Main components of such metal structure are low-temperature bainite (granular, with microhardness of 2100 to 2360 MPa) and to a smaller extent — high-temperature bainite (1850–2030 MPa) (Figure 3, *h*, *q*). Values of strength, ductility and cold resistance almost did not change.

Cooling of 06GBD steel at the rate of $w_{6/5}$ = = 20 °C/s leads to further increase of the amount of products of intermediate transformation (bainite and MAC-phases, Table 4). Microhardness of bainitic component rises up to 2220–2390 MPa (Figure 3, *i*, *r*). Strength and impact toughness values in 06GBD steel remain on the level of 10G2FB steel.

Further increase of cooling rate (above 30 °C/s) in 15KhSATYuD and 10G2FB steels leads to formation and increase of the fraction of martensite component in the total complex of microstructures (Figure 7) that abruptly lowers their impact toughness and ductility values. In 06GBD steel the martensite component practi-

Table 4. Fraction of structural constituents in 06GBD steel at different cooling rates, %

Cooling rate, °C/s	Ferrite	Bainite	MAC-phase
3	94.10	5.90	–
10	79.29	19.51	1.20
20	68.09	27.76	4.15

cally does not form, because of low carbon content (0.06 %) that is in good agreement with mechanical testing results.

Comparison of mechanical testing results of samples, simulating the HAZ of the studied steels (see Figures 4–6) shows that increase of cooling rate leads to gradual increase of yield point and strength, as well as ductility lowering due to increase of martensitic component. WTC has the greatest effect on impact toughness at below zero temperatures (see Figure 4, *b*). In 10G2FB steel KCV_{-40} impact toughness decreases from 320 to 25 J/cm^2, in 06GDB steel — from 170 to 50 J/cm^2, and in 15KhSATYuD steel — from 46 to 22 J/cm^2 already at the cooling rate of 1 °C/s. Such an abrupt drop of toughness of steels with carbide strengthening can be associated with partial dissolution of the carbide phases during WTC [7]. At further increase of cooling rate from 1 up to 30 °C/s, sample toughness slightly rises due to a change in bainitic structure morphology from plate-like to granular one.

At impact bend testing of standard samples with U-shaped notch all the studied steel demonstrated a good toughness ($KCU_{-40} \geq 50$ J/cm^2). At impact bend testing of standard samples with a sharp V-shaped notch impact properties at below zero temperatures (to −40 °C) correspond to the requirements of GOST 27772–88 for steels of strength class C345–440 only for steels with carbide strengthening 10G2FB and 06GBD at cooling rates of 10–25 °C/s.

Impact toughness of simulation samples of 15KhSATYuD steel with a sharp notch KCU_{-40} at cooling rate of 10 °C/s is equal to 20 J/cm^2, and at 25 °C/s it is only 12 J/cm^2 that is related to the features of arrangement of carbonitride particles during secondary precipitation [8]. Investigations reveal the need for correction of the composition of 15KhSATYuD steel, in order to improve its toughness at WTC impact.

Results of these investigations were a scientific basis for application of new 06GBD steel in construction of a motor road bridge across the entrance to the Bay of Podol Bridge Crossing in Kiev [9] and application steel of 10G2FB type in the arch structure of the roofing of a new stadium in Kazan (Russia).

CONCLUSIONS

1. Under the conditions of WTC simulation at cooling rates of 1–60 °C/s, austenite transformation in the studied steels 15KhSATYuD, 10G2FB and 06GBD occurs in the ferritic, bainitic and martensitic regions.

2. At impact bend testing of standard samples with U-shaped notch all the studied steels 15KhSATYuD, 10G2FB and 06GBD demonstrated high performance (according to GOST $KCU_{-60} > 29.4$ J/cm^2). At testing of standard samples with a sharp V-shaped notch only steels 10G2FB and 06GBD with carbide strengthening at cooling rates up to 1 and 10–25 °C/s correspond to the requirements (according to GOST $KCU_{-40} > 39$ J/cm^2).

3. Optimum values of mechanical properties and impact toughness in samples of steels 10G2FB and 06GBD are achieved due to formation of a ferritic-bainitic structure in them at cooling rates of 10–25 °C/s with a small amount of brittle martensitic phase.

1. Matrosov, Yu.I., Litvinenko, D.A., Golovanenko, S.A. (1989) *Steel for main pipelines*. Moscow: Metallurgiya.
2. Shipitsyn, S.Ya., Babaskin, Yu.Z., Kirchu, I.F. et al. (2008) Microalloyed steel for railway wheels. *Stal*, **9**, 76–79.
3. Gretsky, Yu.Ya., Demchenko, Yu.V., Vasiliev, V.G. (1993) Formation of HAZ metal structure of low-silicon steel with carbonitride strengthening. *Avtomatich. Svarka*, **9**, 3–5, 22.
4. Zakharova, I.V., Chichkarev, E.A., Vasiliev, V.G. et al. (2001) Structure and properties of HAZ metal of low-alloyed pipe steels modified with calcium. *The Paton Welding J.*, **8**, 14–17.
5. Sarzhevsky, V.A., Sazonov, V.Ya. (1981) Unit for simulation of welding thermal cycles on the base of MSR-75 machine. *Avtomatich. Svarka*, **5**, 69–70.
6. Steven, W., Mayer, G. (1953) Continuous-cooling transformation diagrams of steels. Pt 1. *J. Iron and Steel Institute*, **174**, 33–45.
7. Livshits, L.S. (1979) *Metals science for welders (welding of steels)*. Moscow: Mashinostroenie.
8. Zmienko, D.S., Stepanova, I.A., Yaropolova, E.I. et al. (2008) Identification of nanoparticles of niobium carbide in steel 10Kh13G12S2N2D2B. *Zavod. Laboratoriya. Diagn. Mater.*, 74(**6**), 40–42.
9. Sineok, O.G., Gerasimenko, A.M., Ryabokon, V.D. et al. (2010) Application of current welding consumables and technologies for welding of improved strength rolled metal. *Visnyk Dnipropetr. Nats. Untu Zalizn. Transporty im. Akad. V. Lazaryana*, Issue 33, 245–250.

RESIDUAL STRESSES IN CIRCUMFERENTIAL BUTT JOINTS IN THE MAIN GAS PIPELINE AT LONG-TERM SERVICE IN THE NORTH

N.I. GOLIKOV and **V.V. DMITRIEV**
V.P. Larionov Institute of Physico-Technical Problems of the North, SD RAS, Yakutsk, RF

Fields of residual welding stresses in circumferential butt joints of the main pipeline of 530 mm diameter with 7 mm wall thickness after long-term service under the North conditions were experimentally studied. It is shown that a high level of tensile residual welding stresses is preserved in circumferential welded joints of the main gas pipeline after 40 years of service. In sites of corrugation formation the residual welding stresses may reach 87 % of base metal yield point. They should be taken into account at calculation of residual life of welded main pipelines.

Keywords: *main welded gas pipelines, circumferential butt joints, HAZ, residual tensile welding stresses, corrugation, residual life*

Service period of some sections of operating main gas pipelines Kysyl–Syr–Mastakh–Berge–Yakutsk, which were put into operation in 1967–1988, is up to 40 years. Acquisition and treatment of statistical data on failures of the main gas pipeline have been performed since the moment of its putting into operation. Analysis of the most characteristic causes for gas pipeline failures revealed that more than 50 % of failures are in circumferential welds with formation of a through-thickness crack. Studying the causes for formation of blowholes showed that the main sites of fracture are defects of welding the root weld (lacks-of-penetration, pores, slags) which are stress raisers [1].

It is known that during welding of field butt joints of pipelines a stress-strain state forms which is induced by a field of residual welding stresses (RWS). One of the features of welding circumferential welds of cylindrical shells is development of weld «sagging», i.e. radial displacements leading to narrowing of pipe diameter in the section of welded joint. This results in lowering of hoop RWS (σ_θ), and at a certain combination of welding modes, metal properties and shell rigidity parameters σ_θ in the weld can even be close to 0. Axial stresses σ_z from the shell inner side turn out to be tensile because of bending, and on the metal surface from the outer side they are compressive [2, 3]. Level of tensile RWS from the inner side of shell wall can reach the base metal yield point [4]. In study [5] circumferential residual strains of a welded butt joint of a pipe from austenitic steel 10Kh18N10T were measured using strain gauges (10 mm base). Proceeding from the obtained data tensile residual welding strains were found in 25–30 mm zone from the weld center on the pipe inner and outer surface. Thus, tensile RWS of circumferential butt joints of pipes are one of the factors strongly influencing appearance of through-thickness brittle cracks in welds.

It is known that at considerable elastoplastic deformations a practically complete relaxation of RWS takes place. In this connection, in the field of quasi-static failures RWS do not affect the cyclic strength of the welded joint. At loading of the corresponding regions of low-cycle fatigue, RWS relaxation usually proceeds quite intensively during the first several cycles [6]. At the same time, data of investigation of RWS relaxation at long-term operation of structures are practically absent. In service the fields of RWS distribution in pipe welded butt joints change as a result of an abrupt temperature gradient, structural changes and elastoplastic deformation. In this connection RWS were studied in circumferential butt joints of the main gas pipeline of 530 mm diameter, 7 mm wall thickness, which was in operation for about 40 years.

RWS measurements in the subsurface layers of the pipe on the inner and outer sides were conducted using a portable X-ray stress determination unit.

The first coil of a pipe fragment with a circumferential butt joint was cut out of a section of the main gas pipeline Berge–Yakutsk, because of formation of a corrugation in it in service. Mechanical characteristics of pipe base metal were $\sigma_t = 501$ MPa, $\sigma_y = 383$ MPa and $\delta = 24.9$ %. By the results of mechanical testing and spectral

© N.I. GOLIKOV and V.V. DMITRIEV, 2012

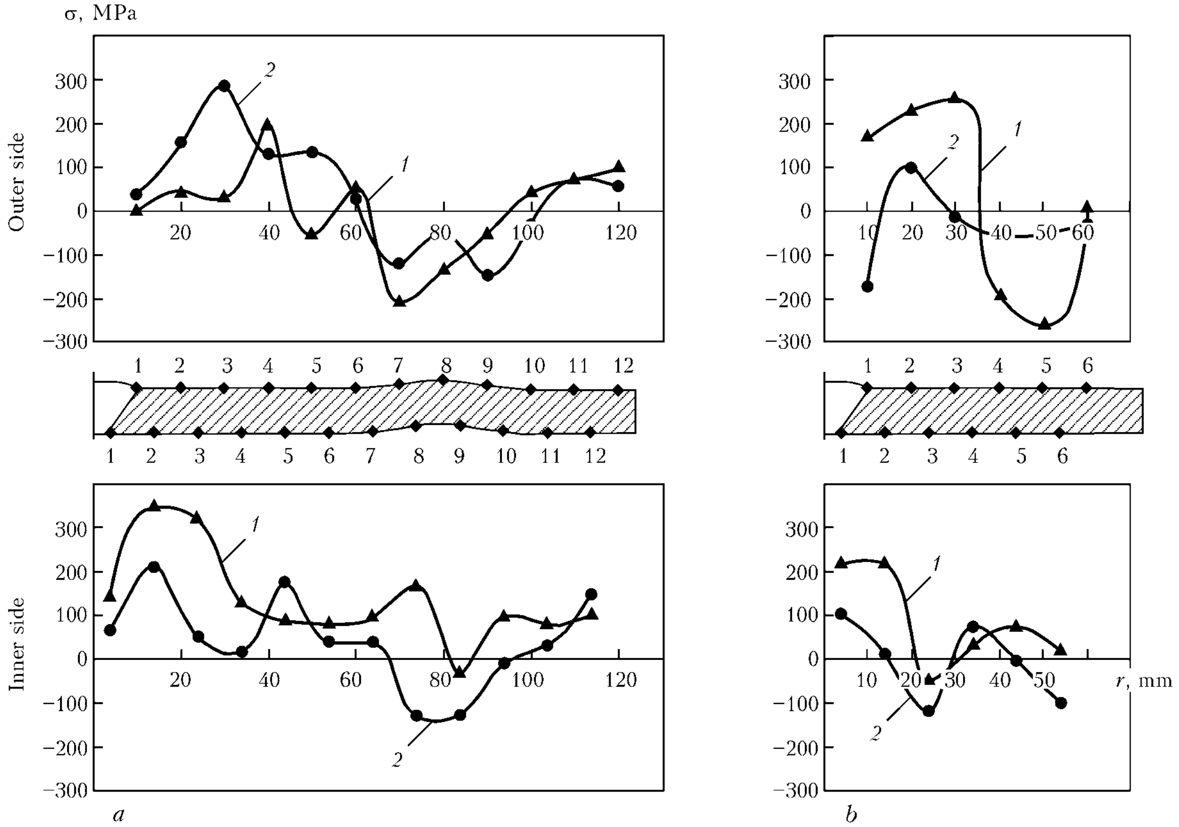

Figure 1. Distribution of residual welding stresses of circumferential butt joint of the first coil of 530 mm diameter gas pipeline from the corrugation side (*a*) and undeformed section (*b*): *1* — axial; *2* — hoop stresses

analysis, pipe metal corresponds to low-alloyed steel of 09G2S grade.

Modes of welding the main gas pipeline are given in the monograph of Prof. V.P. Larionov [7]. Welding was performed in three layers with application of Sv-10G2 welding wire (2 mm diameter) and AN-348A flux, baked at the temperature of 250–300 °C for 1.5 h, in the following modes: I_w = 440–500 A, U_w = 38–42 V, v_w = = 32–35 m/h. This ensured heat input level in the range of 1600–1900 kJ/m that is optimum to produce a welded joint with the required heat resistance. Weld reinforcement was equal to 2–3 mm with a smooth transition to base metal, weld width was 18–20 mm.

Figure 2. General view of fracture of the main gas pipeline Berge–Yakutsk

In gas pipeline service a corrugation of 520 mm length and 7 mm height formed at 80 mm distance from the welded joint. RWS measurements were conducted in the corrugation section, as well as in undeformed section from the pipe opposite side. By the results of measurements from the pipe outer side it was established (Figure 1, *a*) that considerable tensile stresses are found at 30 mm distance from weld center, reaching 300 MPa in the circumferential direction, and up to 200 MPa in the axial direction (at 40 mm distance). Near the corrugation the nature of stress variation is as follows: considerable compressive stresses are found in the circumferential and axial directions, reaching 150–200 MPa. On the inner surface of pipe wall in the near-weld zone a high level of tensile RWS is found in the axial direction, reaching 350 MPa. In points near the corrugation, compressive stresses are found in the circumferential direction (up to 150 MPa) and negligible stresses are observed in the axial direction.

Thus, corrugation formation results in appearance of considerable tensile stresses in the HAZ of the weld on the inner and outer subsurface layers.

In the section from the opposite side on pipe outer surface (Figure 1, *b*) a high level of tensile and compressive stresses is found in the axial direction, reaching 250 MPa at maximum. On the pipe inner surface RWS level at 15 mm distance is equal to 230 MPa.

Second coil was cut out of the main gas pipeline section, where the accident occurred. It consists of complete opening of metal along the pipeline from the outer side with numerous branches of the crack in the site of field circumferential joint (Figure 2). After the accident fracture fragment of the total length of 2160 mm were collected. Circumferential weld was broken in the transverse direction into four individual sections: 1010; 235; 315; 127 mm, respectively. Total weld length around the perimeter is equal to 1687 mm. Fracture was of explosive nature without ignition. Cracks propagated by tearing mechanism in the sites of crack arresting, developing into the shear mechanism with ductile components.

Investigation of pipe fracture surface showed that the fracture nucleus is located on the pipe inner side, normal to the circumferential weld in the HAZ in the site of joining of base metal and weld, and has a considerable extent and length of time of crack growth. Fracture surface is indicative of long-term propagation of the crack.

Crack stopped at transition to base metal that is demonstrated by the transition zone. Then the crack started moving in-depth of base material, where radial scars were observed, originating from this zone and later on going into the main crack which had a chevron pattern. Crack propagated for a longer time and more uniformly in the direction normal to base metal, under the impact of maximum tensile stresses, which are characterized by fatigue ridges. It stopped directly in the weld that is indicative of sufficient resistance of weld metal to crack propagation, compared to base metal.

As fracture nucleus is located from the pipe inner side normal to the circumferential weld, RWS in the pipe inner near-surface layers were studied in the HAZ. Fracture ran through the gas pipeline upper part, so that a sample of 600 × × 700 m size was cut out of the section with the circumferential weld remaining in the trench. By measurement results the level of circumferential RWS at 15 mm distance from weld center reaches 210 MP, that is equal to 65 % of the yield point. Chemical analysis of pipe steel revealed that steels of two different grades 09G2S (pipe 2) and 17G1S (pipe 1) were used. As is seen from Figure 3, RWS distribution relative to weld center is nonsymmetrical. Unsymmetry of RWS distribution is attributable to different chemical composition of the pipes.

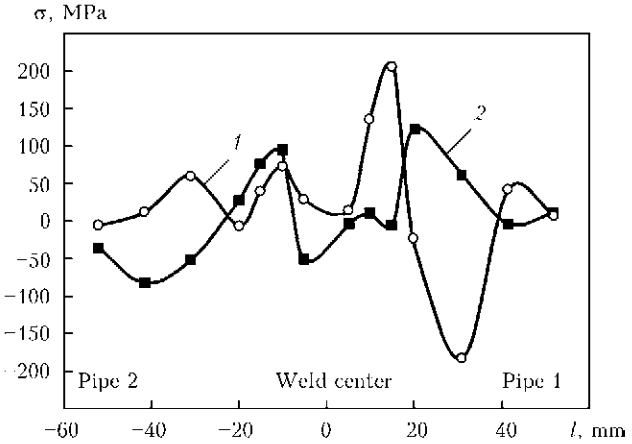

Figure 3. RWS distribution in circumferential butt joint in the second coil of 530 mm diameter pipeline: *1* — hoop; *2* — axial stresses

Thus, conducted investigations showed that in circumferential welded joints of the main gas pipeline of 530 mm diameter a high level of tensile stresses is preserved after its 40 year service. In the sites of corrugation formation RWS can reach 87 % of base metal yield point. Maximum level of hoop stresses in the sample cut out of the section of main gas pipeline, where the accident occurred, reaches 65 % of the yield point. Therefore, RWS should be taken into account at calculation of the residual life of circumferential welded joints of the main pipelines, and the degree of their influence on fatigue strength depends on pipe material.

The study was performed under the project of fundamental research conducted by SD RAS together with UrD RAS in 2012–2014, Project No.27.

1. Lyglaev, A.V., Levin, A.I., Kornev, I.A. et al. (2001) Operation of main pipelines under the North conditions. *Gaz. Promyshlennost*, **8**, 37–39.
2. Vinokurov, V.A., Grigoriants, A.G. (1984) *Theory of welding strains and stresses*. Moscow: Mashinostroenie.
3. Makhnenko, V.I. (1976) *Computational methods for investigation of kinetics of welding stresses and strains*. Kiev: Naukova Dumka.
4. Ammosov, A.P., Golikov, N.I. (1999) Diagnostics of welded joints of above-ground main pipelines operating under the North conditions. *Kontrol. Diagnostika*, **9**, 13–17.
5. Makhnenko, V.I., Velikoivanenko, E.A., Shekera, V.M. et al. (1998) Residual welding stresses in the zone of circumferential butt welded joints of austenitic steel pipelines. *Avtomatich. Svarka*, **11**, 32–39.
6. Ignatieva, V.S., Kulakhmetiev, R.R., Larionov, V.V. (1985) Effect of residual stresses on fatigue crack propagation in welded butt joint zone. *Ibid.*, **1**, 1–4.
7. Larionov, V.P. (1986) *Electric arc welding of structures of the Northern version*. Novosibirsk: Nauka.

FORMATION OF SPINEL IN MELT OF THE $MgO–Al_2O_3–SiO_2–CaF_2$ SYSTEM AGGLOMERATED WELDING FLUX AND ITS EFFECT ON VISCOSITY OF SLAG

I.A. GONCHAROV[1], **V.E. SOKOLSKY**[2], **A.O. DAVIDENKO**[2], **V.I. GALINICH**[1] and **D.D. MISHCHENKO**[1]
[1]E.O. Paton Electric Welding Institute, NASU, Kiev, Ukraine
[2]Taras Shevchenko National University, Kiev, Ukraine

X-ray examinations of structure of agglomerated flux of the $MgO–Al_2O_3–SiO_2–CaF_2$ system in solid and molten states evidence that in a temperature range above 1200 °C the Al_2MgO_4 hard spinel phase with a melting temperature of 2105 °C forms in the slag melt. It determines physical-chemical properties of the melt and, in particular, the smooth character of viscosity changes in a temperature range of 1180–1540 °C. By manipulating proportions and concentrations of spinel-forming components Al_2O_3 and MgO, it is possible to achieve the optimal values of the temperature dependence of viscosity of the slag melt and, on this base, develop welding fluxes with predictable technological properties.

Keywords: *welding, agglomerated flux, structure of slag melts, viscosity, diffraction examinations, spinel*

Conventional-strength steels have been gradually replaced lately by increased- and high-strength steels. To weld such steels it is necessary to use a number of appropriate metallurgical processes and consumables.

Welding of conventional-strength steels is performed by using the $MnO–SiO_2–CaF_2$ slag system fluxes characterised by good welding-technological properties. The latter are achieved due to the fact that structure of the melts of these fluxes is determined by a silicate skeleton of a differing polymerisation degree, which, in turn, determines physical-chemical properties of slag in the molten state at temperatures of existence of the weld pool. To provide formation of the defect-free welds in submerged-arc welding the slag pool should damp oscillations of the metal pool. Therefore, slags must be characterised by a smooth increase in viscosity with decrease in temperature, i.e. they must be «long» [1]. However, despite good technological properties, the manganese-silicate fluxes have limited possibilities in terms of affecting the values of mechanical properties of the weld metal, and impact toughness in particular. This is explained by the fact that welding by using these fluxes involves the processes of formation of silicate non-metallic inclusions and reduction of silicon in the weld metal, which are undesirable for increased-strength steels. To achieve required mechanical properties in welding of high-strength steels, normally the use is made of high-basicity fluxes with an increased content of calcium oxide and fluoride. However, they fail to provide stability of the welding process and quality formation of the welds in multi-arc welding of pipes at a speed of more than 100 m/h, as they are «short», unlike the manganese-silicate fluxes.

Agglomerated fluxes are finding growing application in welding of high- and increased-strength steels. This is attributable to their wider metallurgical possibilities of affecting the weld pool metal. In general, the problems of submerged-arc welding of low-alloy high-strength steels by using agglomerated fluxes are considered in detail in studies by I.K. Pokhodnya [2], D. Olson [3], T. Eagar [4], etc. At the same time, there are almost no studies dedicated to the fundamental research of structure, physical-chemical properties of the slag melts in connection with technological properties of the welding fluxes.

There are several theories describing structure of the welding slag melts. But all of them apply to the equilibrium processes of metallurgy [5–8] characterised by complete remelting of slag components and formation of the liquid slag phase. Unlike the metallurgical processes, the welding processes are rapid. They feature substantial temperature gradients in different zones of the weld pool and, hence, are far from being equilibrium. Moreover, in melting during the welding process the majority of the agglomerated fluxes used now

© I.A. GONCHAROV, V.E. SOKOLSKY, A.O. DAVIDENKO, V.I. GALINICH and D.D. MISHCHENKO, 2012

are not a homogeneous liquid, like the fused fluxes, but a heterogeneous mixture of different phases, some of which are crystalline. At present, there are no slag theories describing the liquid-crystalline structure of a slag, which does not allow theoretical estimation of the effect of the crystalline component of the slag on the processes occurring in the weld pool.

Coarse crystallites present in the matrix of a liquid part of the slag must have a considerable effect on viscosity and, hence, welding-technological properties of the flux. Therefore, one of the purposes of this study was to qualitatively reveal the effect of the crystalline inclusions on viscosity of the slag.

For a number of years we have been developing agglomerated welding fluxes based on the $MgO-Al_2O_3-SiO_2-CaF_2$ slag system. The results obtained prove the possibility of developing a new generation of welding fluxes based on the above system. Study [9] describes investigations of structure of a welding flux of the given system with a low MgO content (10 wt.%), and study [10] — investigations of the processes of melting and solidification of fluxes of the above slag system. As established in study [11], increase in the content of magnesium oxide in fluxes of the $MgO-Al_2O_3-SiO_2-CaF_2$ system leads to decrease in thermodynamic activity of SiO_2 in the slag melt. This fact is very important in terms of metallurgy of welding of high-strength steels, as it makes it possible to reasonably suppress the undesirable processes of silicon reduction and formation of silicate non-metallic inclusions in the weld metal.

Experimental conditions and analysis of experimental data. X-ray examinations of structure of molten and solid slags were carried out at the Physical Chemistry Chair of the Taras Shevchenko National University by using the upgraded X-ray diffractometer for examinations of melts. Monochromatisation of MoK_α-radiation was performed by using a pair of balanced differential filters Zr–Y. Earlier, the diffactometer was used to advantage for examination of fused fluxes in glassy and solid states [12]. After upgrading, this diffractometer allows the diffraction examinations of specimens to be performed both in the liquid and solid states in a temperature range of 100–1700 °C. After granulation and drying of a flux, it was ground into a powder and subjected to X-ray analysis (CuK_α-radiation, diffractometer DRON-3M). Also, investigations were carried out with a solid specimen of the slag after holding at 1500 °C on the sides of the crucible bottom and surface.

The E.O. Paton Electric Welding Institute studied the temperature dependence of viscosity of the investigated flux and a number of model fluxes of the same slag system in order to determine the effect of the solid phase in a liquid slag melt on physical-chemical properties. Viscosity of slags was measured by using the rotational viscometer in the Tamman furnace in a purified argon flow.

Scanning electron microscope JSM-7700F with the X-ray spectral microanalyser was used for obtaining images of the initial and remelted fluxes, and for local chemical analysis of microinclusions.

The powdered specimen of the flux on a graphite substrate and the solidified specimen of the slag produced from it by remelting in the molybdenum crucible at a temperature of 1500 °C in the high-purity helium atmosphere were subjected to electron optical examinations. The slag specimen was examined on the side of both bottom and surface of the molybdenum crucible. To prevent the effect of charging of the specimen by the electron beam, a 3 nm thick layer of pure platinum was sprayed on the specimen surface.

Filming of the flux specimen was carried out at temperatures of 600, 800, 1000, 1200, 1300, 1400 and 1500 °C in a high-temperature vacuum chamber in the high-purity helium atmosphere.

Chemical composition of the specimens was controlled by the X-ray fluorescent analysis method.

Structural software Powdercell and Mercury, data bases Match and Retrieve, which are disseminated free of charge through the Internet, were used to interpret the X-ray analysis data. The software developed in-house was used in calculations for investigation of the slag melt [12].

Investigations at room temperature. The calculated contents of the main components of the flux, i.e. MgO, Al_2O_3, SiO_2 and CaF_2, are given in Table 1. Liquid glass Na–K was added to the refined mechanical mixture in the granulator. After granulation, the flux was held for 24 h at a temperature of 20 °C, and then was baked for 1 h at 500 °C. The actual chemical composition of the flux, according to the X-ray fluorescent analysis data, is also given in Table 1.

Results of electron microscopic examinations of the powdered agglomerated flux indicate that

Table 1. Composition of welding flux, wt.%

Type of analysis	MgO	Al_2O_3	SiO_2	CaF_2	Na_2O	K_2O	Fe_2O_3
Calculated	30	25	20	25	–	–	–
Actual	25.8	18.7	28.4	22.2	1.58	0.8	1.88

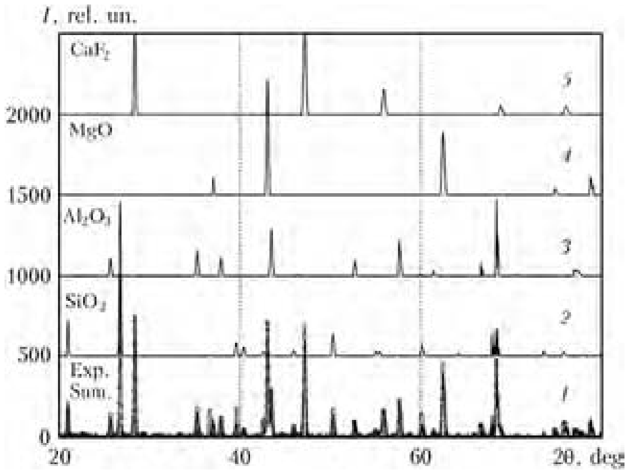

Figure 1. Diffraction patterns of agglomerated flux ground into a powder (points) and summation curve after upgrading of profile based on elementary cells of SiO_2, Al_2O_3, MgO and CaF_2 according to Powdercell (solid line) (*1*), α-quartz (*2*), corundum (*3*), periclase (*4*), and fluorite (*5*)

particles of initial components MgO, Al_2O_3, SiO_2 and CaF_2 hardly undergo any changes as a result of granulation and subsequent baking at a temperature of 500 °C.

X-ray phase analysis (Figure 1) showed that after granulation and drying the specimen contained only the initial components, such as α-quartz, trigonal Al_2O_3, and cubic MgO and CaF_2. No primary products of solidification of the components based on the liquid glass were detected.

Figures 2–5 show microstructures and data of microanalysis of the bottom and surface of the specimen after remelting in the molybdenum crucible. Microstructures on the crucible surface and bottom sides differ to some extent. The crystalline phases formed on the bottom side are finer (Figure 2, spectrum 3). It can be clearly seen that the continuous matrix of one of the phases (the lightest one) contains inclusions of other, finer phases. It is practically impossible to identify this phase as one compound. Most probably, this phase was formed as a result of melting of low-melting point components of the flux and dissolution of some solid components in the melt. If we discard impurities the content of which is less than 2 at.% and ignore a too high concentration of fluorine, the darker phase at the centre (Figure 2, spectra 2 and 4) can be identified as Mg_2SiO_4. The magnified part of image 1 (in black frame) is illustrated as electron image 2 in Figure 3, where spinel Al_2MgO_4 in crystallites looking like octahedron, and CaF_2 in the form similar to spherulites can be clearly seen (spectra 3 and 6). On the bottom side, X-ray spectral analysis fixed no regions with sodium oxide inclusions.

Examinations conducted on the remelted flux surface side evidence a more complicated character of interactions between the components, compared to the bottom side. Inclusions heavily saturated with impurities (Figure 4, spectrum 5)

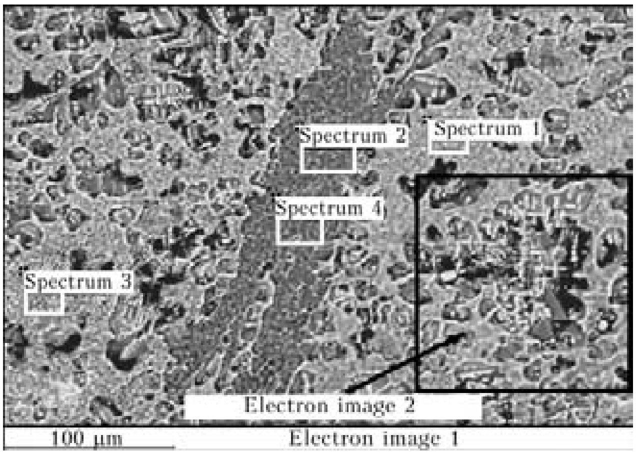

Spectrum	O	F	Mg	Al	Si	Ca
1	55.4	13.2	7.5	3.9	10.1	10.0
2	54.4	6.2	25.5	0.9	11.6	1.4
3	55.3	13.0	7.4	4.3	10.3	9.7
4	54.3	6.6	25.0	1.4	11.2	1.5

Figure 2. Microstructure of remelted flux (crucible bottom, image 1), and results of X-ray spectral analysis (at.%). Spectra 2 and 4 can be identified as Mg_2SiO_4

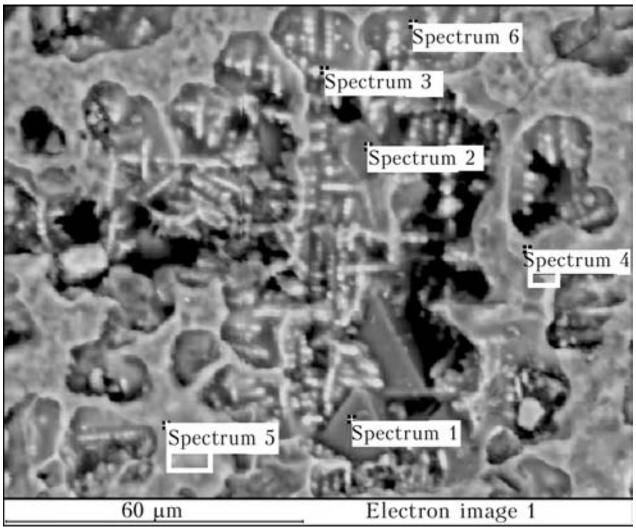

Spectrum	O	F	Mg	Al	Si	Ca
1	65.5	1.1	12.8	20.2	0.3	0.2
2	58.3	3.9	14.0	22.2	0.9	0.8
3	44.3	32.8	4.0	2.1	5.4	11.3
4	59.6	14.6	7.2	3.0	8.6	7.0
5	56.7	12.5	6.8	3.8	10.9	9.3
6	44.1	33.3	3.5	2.0	5.0	12.1

Figure 3. Microstructure of remelted flux (crucible bottom, image 2, see Figure 2), and results of X-ray spectral analysis (at.%). Spectra 1 and 2 can be identified as Al_2MgO_4, and spectra 3 and 6 – as CaF_2

can be detected on the surface. It should be noted that sodium is concentrated particularly on this type of the inclusions. Spectrum 2 can be interpreted as $(MgCa)_2SiO_4$, probably with the aluminium cation impurities, the concentration of fluorine being ignored. Spectrum 3 is closest to CaF_2, but with an excess of oxygen. Spectra 1 and 4 in Figure 4 seem to form on a base of the partially solidified low-melting point phase, like spectra 1 and 3 in Figure 2. However, they differ in composition both from each other and from similar images on the bottom side.

Of notice is the fact that fluorine in considerable amounts is present almost in all reflections, while oxygen exceeds stoichiometric compositions of the identified phases (see Figures 2–5). Spinel crystallites contain the least amounts of impurities, although the Al/Mg ratio is about 1.58 on the bottom side and 1.50 on the surface side (in stoichiometric spinel the Al/Mg ratio is equal to 2). Almost all the specimens contain no sodium. Most probably, it is concentrated in sites of accumulation of impurity oxides (Figure 4, spectrum 5), or along the crystalline grain boundaries. It should be noted that spectra of the close phases on the bottom side differ from those on the surface side (Figure 5).

The X-ray pattern of the surface side of a specimen remelted at a temperature of 1500 °C is shown in Figure 6. The main phases on the crucible surface side are cubic spinel (space group *Fd–3m* (227), $a = 0.8100$ nm), cubic CaF_2 (space group *F4/m–32/m* (225), $a = 0.546$ nm) and Mg_2SiO_4. It is reported that the Mg_2SiO_4 phase can exist in several modifications. The cubic modification of this phase (of the spinel type) with parameter $a = 0.806–0.811$ nm is very close to the classic spinel. Diffraction reflections of the spinel form of Mg_2SiO_4 almost fully coincide with the spinel reflections, providing that they have identical lattice parameters. It is noteworthy that reflection (440) both for spinel and for Mg_2SiO_4 is localised in a region of 65.25° to 2θ. However, this reflection is not the most intensive one for these two phases. X-ray phase analysis (see Figure 6) confirms the presence of an orthorhombic phase (*Pbnm*) of Mg_2SiO_4 with $a = 0.4822$, $b = 1.1108$ and $c = 0.6382$ nm. Also, there is a phase close to the spinel one for Al_2O_3. However, the lattice parameter of this spinel is much lower compared to the magnesium aluminate one ($a = 0.7932$ nm). It is likely that at the beginning, as the temperature is increased, the corundum-like lattice of Al_2O_3 transforms into the cubic form close to the spinel one, diffusion of MgO into such a lattice considerably grows, and the normal spinel phase forms. The relative intensity of this reflection for phases of the spinel type does not exceed 70 % (or much lower) of 100 % reflection (311) in a region of 36.85°. In our case the most intensive reflection is (440).

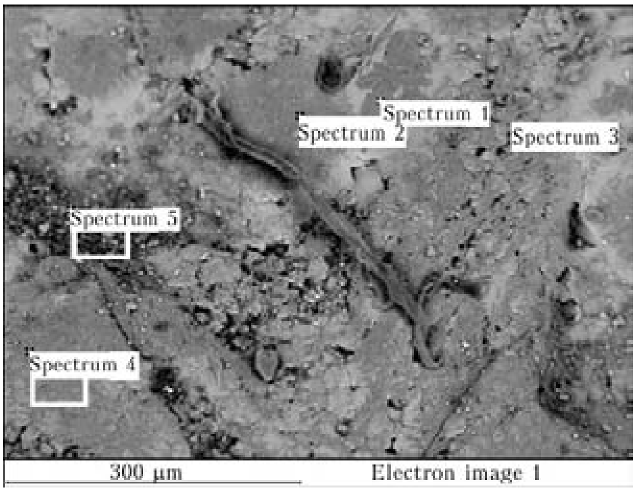

Spectrum	O	F	Na	Mg	Al	Si	Ca
1	59.5	10.3	–	11.8	6.2	8.1	4.09
2	55.1	7.7	–	17.2	4.4	10.6	4.92
3	44.3	32.8	–	4.0	2.1	5.4	11.30
4	56.5	14.8	–	15.5	2.6	7.2	3.36
5	58.6	17.9	1.3	7.0	2.5	3.8	7.90

Figure 4. Microstructure of products of solidification of the low-melting point phase of remelted flux (crucible surface), and results of X-ray spectral analysis (at.%)

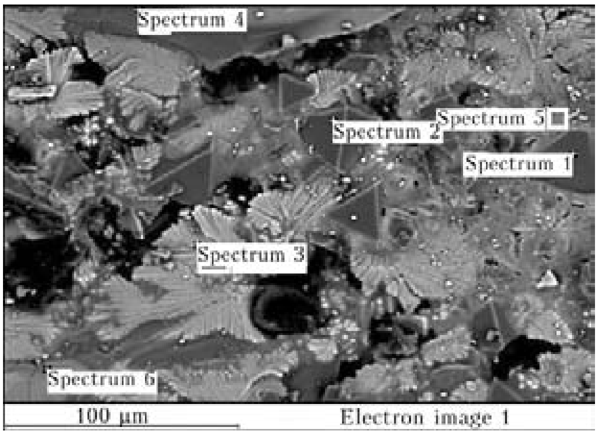

Spectrum	O	F	Mg	Al	Si	Ca
1	66.8	–	13.2	19.8	0.1	0.1
2	73.5	–	10.7	15.6	0.1	0.1
3	24.1	51.7	1.5	1.5	3.7	17.5
4	65.6	1.3	21.7	0	11.0	0.3
5	67.3	–	13.0	19.5	0.1	0.1
6	67.5	–	12.9	19.4	0.1	0.1

Figure 5. Microstructure of products of solidification of the main part of remelted flux (crucible surface), and results of X-ray spectral analysis (at.%). Spectra 1, 2, 5 and 6 can be identified as Al_2MgO_4, and spectrum 4 — as Mg_2SiO_4

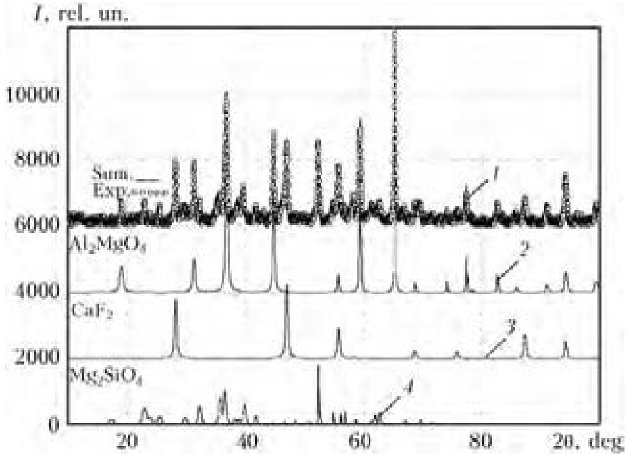

Figure 6. Diffraction patterns of the flux remelted at 1500 °C on the surface side: *1* — experiment and summation curve of spinel Al_2MgO_4, calcium fluoride and Mg_2SiO_4; *2–4* — upgraded profiles, according to PCW, of spinel Al_2MgO_4 (*2*), CaF_2 (*3*) and Mg_2SiO_4 (*4*)

It seems that this possibility exists when at first one of the phases forms, and when the other phase starts growing epitaxially on one of its faces, or, which is more probable, when in formation of the liquid phase together with the crystalline spinel its crystallites become oriented in a certain direction relative to the melt surface. It should be added that the Al_2MgO_4 spinel crystallites in the form of black octahedrons are unambiguously interpreted by electron microscopy analysis (see Figures 3 and 5), and the phase close to spinel Mg_2SiO_4 is not solidified in the form of octahedrons. X-ray spectral analysis confirms the presence of Mg_2SiO_4, probably in the $(CaMg)_2SiO_4$ form (see Figures 2 and 4).

Spinel is not the main phase on the bottom side. Moreover, it was difficult to detect spinel on the bottom side because of its low concentration. Figure 2 shows probably the only spinel phase found at the bottom, and in Figure 3 it is shown on an increased scale. Spectra 1 and 3 (see Figure 2) are characterised by a marked presence of all the elements, and they are hard interprete unambiguously. It is likely that this is the phase that formed from the melt and had no time to solidify by preserving a partially amorphous state. No phases with a close composition were fixed in the diffraction patterns. Therefore, the spinel octahedrons (see Figure 3, spectra 1 and 2), Mg_2SiO_4 (see Figure 2, spectra 2 and 4), CaF_2 in the formations looking like spherulites and the liquid-type phase were unambiguously interpreted on the bottom side.

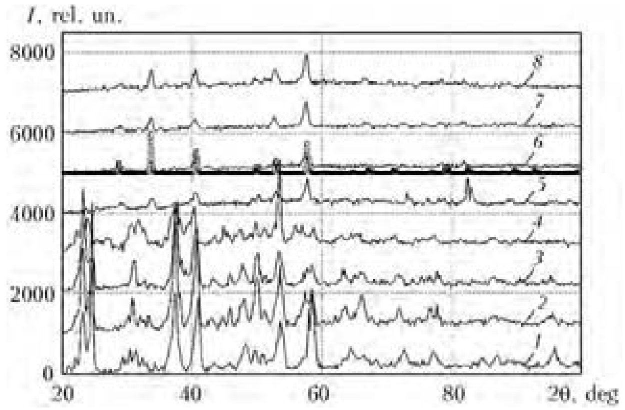

Figure 7. Diffraction patterns of the flux (MoK_α-radiation) at room temperature (*1*), 600 (*2*), 800 (*3*), 1000 (*4*), 1200 (*5*), 1300 (*6*), 1400 (*7*) and 1500 (*8*) °C. Diffraction pattern of pure spinel (points) is superimposed on diffraction pattern at 1300 °C. Diffusion background is fully removed

The X-ray pattern of the remelted flux on the bottom side is hard to interpret. Almost every peak has strong asymmetry on the side of small scattering angles, this evidencing a poor phase formation on the bottom side. For example, the phases close in structure, i.e. the spinel form of aluminium dioxide, Mg_2SiO_4, and high- and low-temperature spinels, which have the same structural type of lattice parameters a, i.e. $Fd{-}3m$, but can range from 7.90 to 8.20 nm, persist on the bottom side. In general, the phases appearing on the bottom side are poorly formed and hard to distinguish. X-ray analysis confirms the presence of spinel Al_2MgO_4, Mg_2SiO_4 and CaF_2.

High-temperature X-ray solid-state examinations. To trace the sequence of solid-state reactions, the ceramic flux ground into a powder was placed into a molybdenum crucible, which was mounted on a work table inside a high-temperature vacuum chamber of the diffractometer for examinations of melts [12], and subjected to high-temperature X-ray phase analysis. As shown by the analysis, structural changes in a specimen occur over the entire temperature range (Figure 7). Up to 1200 °C, they take place in the solid phase. At low temperatures, the structural changes are slow and occur mainly inside the phases. For example, the most intensive peak corresponding to the 100 % intensity of hexagonal α-quartz dramatically decreases already at 600 °C. At the same time, there appear the peaks corresponding to other modifications of silica.

Solid-state interactions between the phases begin at higher temperatures. It should be taken into account that the main components in the agglomerated flux are contained in the matrix of a binding material (Na–K liquid glass annealing product). Formation of vacancies in the matrix during evaporation of water will lead to the fact that the inter-phase interaction will take place due to diffusion of atoms of the flux components into the matrix at a rather high rate. Probably, nuclei of the new phases, which can partially dissolve at the initial stage of melting of some flux components in the molten phase, or, on the contrary, can accumulate due to intensified interaction with the molten phase, will start forming in the matrix on a base of the liquid glass remainders. Below 1200 °C, the melts preserve the main components, although, as can be seen from Figure 7, intensive decrease in their peaks and, hence, destruction of the initial structures take place. At 1200 °C, the diffraction patterns show practically no reflections corresponding to the initial flux components. The flux melts. However, a new crystalline phase, i.e. spinel Al_2MgO_4, forms against the background of the molten component.

The diffraction pattern of pure spinel is superimposed on the diffraction pattern of a specimen at a temperature of 1300 °C (see Figure 7). Then the spinel reflections in a temperature range of 1200–1500 °C coincide in location with the specimen reflections. The relative intensity of the reflections is in some disagreement with the tabular data. This can be the case if the crystallites of spinel in the melt are oriented with a certain plane relative to the melt surface, rather than being chaotically located. As the melt surface is saturated with spinel to a much greater degree, and the bottom — to a lesser degree, it can be assumed that the spinel is lighter than the liquid phase and, as such, it floats to the surface.

Discussion of results. The insignificant additions the content of which is not in excess of 1 wt.% being ignored, to interpret the results obtained it is necessary to use a complex constitutional diagram of $Na_2O–Al_2O_3–MgO–SiO_2–CaF_2$. But this oxide-fluoride diagram is not available in the scientific literature. The closest, well-studied constitutional diagram for the four-component system is $CaO–MgO–Al_2O_3–SiO_2$ [13]. As discovered in investigation of the agglomerated flux of the calculated MgO (10 wt.%)–Al_2O_3 (25 wt.%)–SiO_2 (40 wt.%)–CaF_2 (25 wt.%) composition, CaF_2 at least partially transforms into an oxide [9, 14]. It was established for this flux that the main phase has the form of anorthite, i.e. $CaAl_2Si_2O_8$, where calcium has the oxide form. Probably, MgF_2 forms in small amounts. Spinel Al_2MgO_4 does not form in this case. The spinel fields appear in the $CaO–MgO–Al_2O_3–SiO_2$ diagram already in a section of 15 wt.% Al_2O_3. In the $MgO–Al_2O_3$ binary constitutional diagram the spinel is almost stoichiometric at low temperatures, and features a wide range of homogeneity at high temperatures. Earlier the spinel was not distinguished from the cubic modification of Al_2O_3. Solid solutions based on spinel MgO and Al_2O_3 are found in the entire concentration range of the constitutional diagram at a temperature of up to 2000 °C. Investigations of the solid solutions of Al_2O_3 in the spinel show that they have cation vacancies, which are readily filled up from external sources. Reaction of formation of the spinel in the solid phase from aluminium oxide begins approximately at 750 °C [15]. According to [13], the initial stage of formation of the spinel occurs by the surface diffusion of alumina into MgO, which is followed by the volume diffusion of atoms (ions) of magnesium and aluminium through the oxygen sub-lattice to transform the hexagonal arrangement of this sub-lattice in corundum into the cubic one (probably, the corundum itself first forms the cubic lattice of the spinel type). A high melting temperature of spinel and physical-chemical properties of the slag melts it determines arouse considerable interest in the spinel when developing a new generation of welding fluxes. The spinel phase persists after remelting of the flux during the welding process and its transformation into a slag crust.

Therefore, the presence of spinel is an experimental fact, and it is necessary to reveal all advantages and drawbacks of the presence of a solid spinel phase in the melt, as well as its effect on the welding process. It is possible to distinguish four moments which can be affected by formation of the crystalline spinel, although, in general, there may be much more of such moments.

1. If the thermal expansion coefficients of spinel and liquid phase solidification products differ greatly at the temperatures of detachment of the slag crust from the weld metal (250–500 °C), this will induce microstresses in the matrix of the former liquid phase, thus creating preconditions for good detachability of the slag crust from the surface of the metal welded.

2. The presence of the crystalline phase in the liquid slag melt at a temperature of about 1100–2000 °C will have a considerable effect on viscosity of the melt. Increase in the content of the crystalline spinel in the molten slag may lead to increase in viscosity and make the molten slag «longer», this being a positive factor in terms of the technological properties of the flux, which was already noted at the beginning of the article.

3. The general decrease in the content of electricity carriers in the slag during formation of the spinel phase due to decrease in the quantity and mobility of elementary particles (ions and electrons) may lead to a substantial decrease in electrical conductivity. This also is a positive factor, as it will allow mitigating the effect of

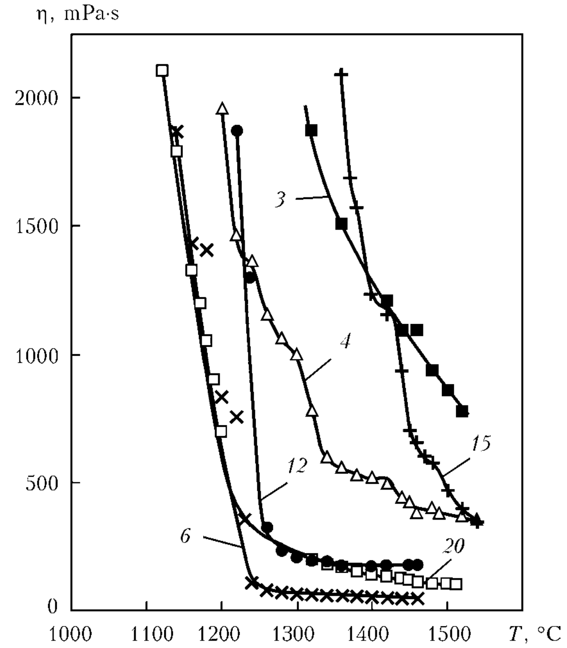

Figure 8. Temperature dependence of viscosity of model slags of the MgO–Al_2O_3–SiO_2–CaF_2 system (numbers of curves correspond to numbers of fluxes in Table 2)

shunting of the current through the slag and improving stability of the process in case of multi-arc welding.

4. The presence of the solid phase in the slag melt will reduce thermodynamic activity of some components of the flux and, hence, affect its metallurgical properties, as was confirmed by the investigations [11].

The most important factor in terms of ensuring the required technological properties of the welding flux is a temperature dependence of its viscosity. Several model agglomerated welding fluxes of the investigated system were made for further investigations of viscosity. The calculated compositions of the fluxes are given in Table 2, and the viscosity measurement results are shown in Figure 8. It was found that the intensity of reflection of the crystalline spinel decreases from specimen to specimen in the following order: 3 → → 15 → 4 → 12, this being in correlation with decrease in sum of the spinel components, i.e. MgO + Al_2O_3 (see the last column in Table 2). In our opinion, the sum of the spinel components in the first approximation can serve for quantitative evaluation of the spinel until the other criterion is found, which can correlate with the content of the crystalline spinel in a specimen. In specimens 6 and 20, no spinel was detected because of the absence of Al_2O_3, and its content in specimen 12 is too low because of a low content of Al_2O_3.

Table 2. Calculated compositions of model welding fluxes, wt.%

Flux number	MgO	Al_2O_3	SiO_2	CaF_2	MgO + Al_2O_3
3	40	30	15	15	70
4	30	25	20	25	55
6	40	0	35	25	–
12	40	10	40	10	50
15	40	25	10	25	65
20	35	0	40	25	–

It was established that fluxes (6, 12 and 20) with the content of magnesium and silicon equal to 35–40 % and aluminium oxide equal to 10 % are characterised by a jump-like change in viscosity in a temperature range of 1150–1250 °C. These are the so-called «short» fluxes. Fluxes 3 and 15 with 40 wt.% of magnesium oxide and 25–30 wt.% of aluminium oxide are characterised by a high viscosity over the entire range of the studied temperatures. The absence of the flat part on the viscosity curve is indicative of an incomplete melting of these slags and presence of a large number of solid particles in the melt, which could be observed in the course of the experiment. Most probably, this phase is Al_2MgO_4. Flux 4 investigated here has a somewhat lower calculated content of magnesium oxide (30 wt.%), and the content of aluminium oxide in it is 25 wt.% (see Tables 1 and 2). This flux is characterised by a rather smooth change in viscosity over the entire temperature range (see Figure 8; flux 4 in Table 2). In this case the curve comprises some «steps», which can be explained by solidification of extra portions of the Al_2MgO_4 solid phase from the melt. As to the character of the temperature dependence of viscosity, flux 4 is close to manganese-silicate flux AN-60. Welding-technological tests of the fluxes indicated in Table 2 showed that flux 4 has the best properties. Therefore, it is the presence of the solid phase in the slag melt, in our opinion, that determines the character of the temperature dependence of viscosity. It is likely that by manipulating with the proportions and concentrations of spinel components Al_2O_4 and MgO it is possible to achieve the required viscosity values and character of the temperature dependence, and, on this base, develop fluxes with the controllable viscosity and predictable technological properties. We believe that fluxes, in the melts of which the crystalline spinel forms, will combine good technological and metallurgical properties.

CONCLUSIONS

1. X-ray examinations of structure of the MgO–Al_2O_3–SiO_2–CaF_2 system agglomerated flux in the initial, molten and solid states, after holding at 1500 °C, were carried out. Images of the initial

and remelted flux were obtained by using scanning electron microscope JSM-7700F fitted with the X-ray spectral microanalyser, and local chemical compositions of the microinclusions were determined. Viscosity of the slags was measured by using the rotational viscometer in a purified argon flow inside the Tamman furnace.

2. The examinations conducted evidence a complex character of interactions taking place in the agglomerated flux before formation of the molten slag phase. The main structural changes in heating the flux to 1200 °C occur due to the solid-phase interactions in a product formed by a cake of the liquid glass with the adjacent main components of the flux.

3. Formation of the liquid phase begins in a temperature range of about 1200 °C due to melting of the cake of the liquid glass with the main components and complex unstable compounds. The solid Al_2MgO_4 spinel phase having a melting temperature of 2105 °C forms in this case in the melt. Full melting of the flux of the investigated composition does not take place in a temperature range of up to 1500 °C. This phase persists in the slag crust after remelting of the flux during the welding process. The presence of the solid Al_2MgO_4 phase in the slag melt of the $MgO–Al_2O_3–SiO_2–CaF_2$ system determines its physical-chemical properties, in particular the smooth character of viscosity changes in a temperature range of 1180–1540 °C.

4. It is an established fact that by manipulating the proportions and concentrations of spinel-forming components Al_2O_3 and MgO it is possible to achieve the optimal values of the temperature dependence of viscosity of the slag melt and, on this base, develop welding fluxes with controllable technological properties.

The authors express their gratitude to Company «Tokyo Boeki» and personally to Dr. Tinkov V.A. for conducting electron microscopy examinations and assistance in interpretation of the obtained results.

1. Podgaetsky, V.V., Lyuborets, I.I. (1984) *Welding fluxes*. Kiev: Tekhnika.
2. Pokhodnya, I.K., Yavdoshchin, I.R., Shvachko, V.I. et al. (2004) *Metallurgy of arc welding. Interaction of gases with metals*. Ed. by I.K. Pokhodnya. Kiev: Naukova Dumka.
3. Olson, D.L. (1983) The investigation of the influence of welding flux on the pyrometallurgical, physical and mechanical behavior of weld metal. In: *Final report of Center for welding research Colorado school of mines Golden Colorado*.
4. Eagar, T.W. (1991) Thermochemistry of joining. In: *Proc. of Elliot Symp. on Chemical Process Metallurgy*.
5. Herasymenko, P., Speigth, G.E. (1950) Ionic theory of slag-metal equilibrium. *J. Iron and Steel Inst.*, **166**, 169–183, 289–303.
6. Tyomkin, M.I. (1946) Mixtures of molten salts as ionic solutions. *Zhurnal Fizich. Khimii*, Issue 1, 105–110.
7. Kozheurov, V.A. (1955) *Thermodynamics of metallurgical slags*. Sverdlovsk: Metallurgizdat.
8. Esin, O.A. (1961) About the nature of molten silicates. *Tr. Ural. Polytechn. In-ta*, Issue 122, 29–39.
9. Sokolskii, V.E., Roik, A.S., Davidenko, A.O. et al. (2012) X-ray diffraction and sem/edx studies on technological evolution of the oxide-fluoride ceramic flux for submerged arc-surfacing. *J. Min. Metall. B*, **48**, 101–113.
10. Duchenko, A.N., Mishchenko, D.D., Goncharov, I.A. et al. (2011) Study of the process of melting and solidification of fluxes of the $Al_2O_3–MgO–SiO_2–CaF_2$ slag system. In: *Proc. of 13th Rus. Conf. on Structure and Properties of Metallic and Slag Melts*. Vol. 3: Experimental investigation of slag melts, metal-slag interaction (Ekaterinburg, 2011), 136–139.
11. Goncharov, I.A., Galinich, V.I., Mishchenko, D.D. et al. (2011) Prediction of thermodynamic properties of melts of $MgO–Al_2O_3–SiO_2–CaF_2$ system. *The Paton Welding J.*, **10**, 2–4.
12. Shpak, A.P., Sokolsky, V.E., Kazimirov, V.P. et al. (2003) *Structural peculiarities of oxide system melts*. Kiev: Akademperiodika.
13. Berezhnoj, A.S. (1970) *Multi-component oxide systems*. Kiev: Naukova Dumka.
14. Sokolsky, V.E., Roik, A.S., Davidenko, A.O. et al. (2010) On phase transformations in agglomerated flux of salt-oxide slag system at heating. *The Paton Welding J.*, **12**, 9–14.
15. Pashchenko, A.A., Myasnikov, A.A., Myasnikova, E.A. et al. (1986) *Physical chemistry of silicates*: Manual. Ed. by A.A. Pashchenko. Moscow: Vysshaya Shkola.

EFFECTIVENESS OF VARIOUS VARIANTS OF ELECTRODYNAMIC TREATMENT OF AMg6 ALLOY AND ITS WELDED JOINTS

L.M. LOBANOV, N.A. PASHCHIN, O.L. MIKHODUJ, A.V. CHERKASHIN, A.N. MANCHENKO, I.P. KONDRATENKO and **A.V. ZHILTSOV**
E.O. Paton Electric Welding Institute, NASU, Kiev, Ukraine

Influence of various variants of discharge circuits on effectiveness of electrodynamic treatment (EDT) of aluminium alloy AMg6 and its welded joints was studied. It is established that maximum EDT effectiveness is achieved at simultaneous impact of pulsed electric current and dynamic load on the treated metal, while minimum effectiveness is achieved at the impact of just the pulsed current. Deformation wave parameters were studied at EDT of AMg6 alloy welded joints.

Keywords: *welded joints, aluminium alloy, residual stresses, electrodynamic treatment, deformation wave, flat inductor, capacitive energy storage, treatment effectiveness*

Methods of treatment of metallic materials and their welded joints by applying pulsed electromagnetic fields to them are becoming ever wider accepted at regulation of the stressed state of welded structure elements [1, 2].

One of such methods is electrodynamic treatment (EDT) based on simultaneous impact of electric current and dynamic load on the electric contact point. Electrodynamic impact on the metal (welded joint) is produced at discharge of capacitive energy storage through electric contact of working electrode with the metal surface. Investigations were conducted earlier on evaluation of the influence on treatment effectiveness of such parameters of electrodynamic impact, as charging voltage, storage capacitance, and amplitude values of pulsed current [3]. During current discharge passage electric pulse and dynamic processes are initiated in the treated material, determined by electroplasticity mechanism [4] and generation of deformation waves in the material, respectively. Interaction of electroplastic and dynamic components of EDT at passage of pulsed current through the treated item determines its effectiveness.

The objective of this work is assessment of electroplastic effect and dynamic force load, determining the effectiveness of EDT of AMg6 aluminium alloy and its welded joints.

The work was performed using an EDT system, the principle of operation of which is described in [5], and design features of discharge circuit elements providing the electrodynamic impact on the treated metal are given in [3]. The system (Figure 1, *a*) consists of capacitive storage C, flat inductor L, electrode *2* and disc *3* from nonferromagnetic material. Electric power in the storage device C in the form of a current pulse is transferred into treated metal *1* at the moment of closing of contactor K. At current passage through inductor L a pulsed magnetic field is excited in it, which induces eddy current in the disc. Its interaction with the magnetic field generates an electromagnetic force. Force impact is transferred from the disc to the electrode, which transfers the electrodynamic impact to the metal. Thus, the capacitive storage discharge ensures interaction of two mechanisms — dynamic force impact of the electrode with simultaneous passage of pulsed electric current through the material being treated.

Influence of various variants of discharge circuit (Figure 1) on parameters of electrodynamic impact at EDT was studied, including amplitude values of pulsed current I and dynamic loads P during the time of capacitive storage discharge. Measurements of I and P were performed in the instrumentation complex, the principle of operation of which is set forth in [3]. Values of pulsed current I were recorded by contactless method of Rogowski loop, parameters of dynamic load P were recorded by a piezoelectric pressure sensor, and a cylindrical sample from an aluminium alloy was used as the treated material.

Four circuit variants were studied. In the first (basic) variant (see Figure 1, *a*) discharge current flowed through inductor L, disc *3*, electrode *2* and treated metal *1*. In this case, parameters I and P were determined by electrodynamic interaction of such circuit elements as «inductor +

© L.M. LOBANOV, N.A. PASHCHIN, O.L. MIKHODUJ, A.V. CHERKASHIN, A.N. MANCHENKO, I.P. KONDRATENKO and A.V. ZHILTSOV, 2012

disc» and «electrode + metal». In the second variant (Figure 1, *b*), inductor *L* was removed from the disc to distance h = 10 mm, but was included into the circuit. This eliminated the factor of dynamic pressure of the inductor on the disc at preservation of equality of discharge circuits (see Figure 1, *a*, *b*). In the third variant inductor *L* was completely excluded from discharge circuit (Figure 1, *c*) that allowed assessment of the influence of its resistance on values of parameters *I* and *P*, as well as their rise speeds. The circuits embodied in variants shown in Figure 1, *b*, *c* allow assessment of the influence of pulsed current on electrodynamic impact at EDT. In the fourth variant (Figure 1, *d*) discharge circuit was closed to inductor *L* that eliminated current flowing through treated metal and allowed assessment of the contribution of dynamic load *P* resulting from interaction of «disc + electrode» elements of the circuit to electrodynamic impact at EDT.

Calculation of parameters *I* and *P* (Figure 2) was conducted by the procedure of [6] at implemented variants of discharge circuit, shown in Figure 1. Figure 2, *a* gives calculated values of pulses of current and load at discharge of capacitive storage of 6600 μF capacitance charged up

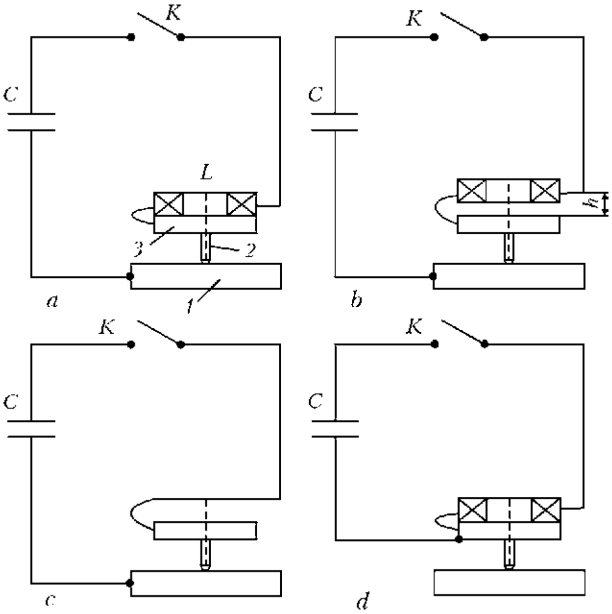

Figure 1. Variants of discharge circuit in EDT system: *a* — current discharge runs through flat inductor *L*, disc *3*, electrode *2* and metal sample *1*; *b* — similar to *a*, but air gap *h* is provided between flat inductor and disc; *c* — current discharge runs through the disc, electrode and metal sample, flat inductor is eliminated; *d* — current discharge runs through the flat inductor and disc

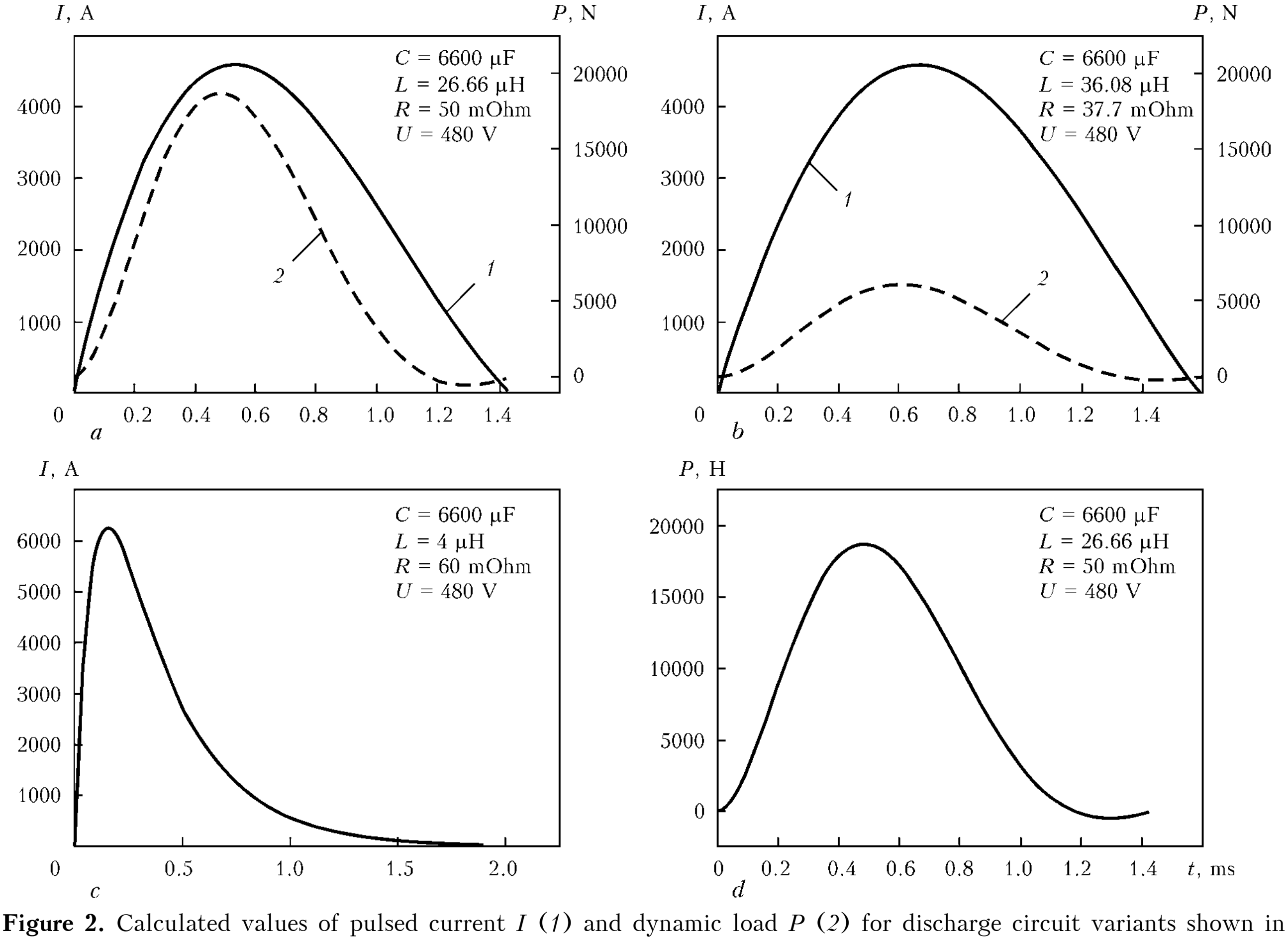

Figure 2. Calculated values of pulsed current *I* (*1*) and dynamic load *P* (*2*) for discharge circuit variants shown in Figure 1, *a*–*d*, respectively

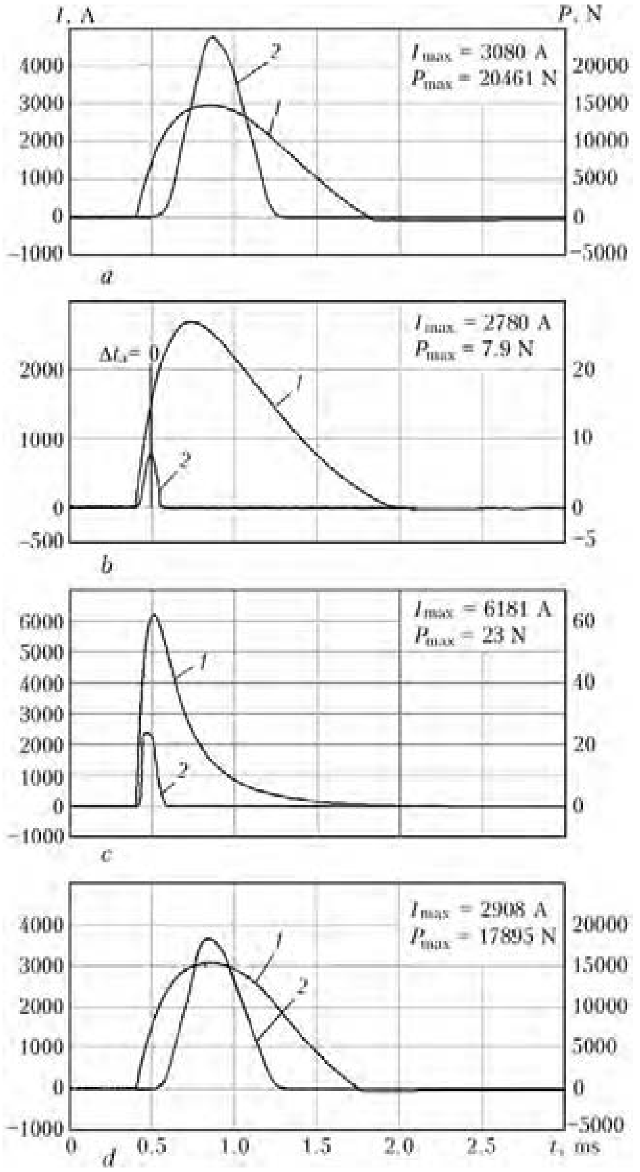

Figure 3. Experimental values of pulsed current I (*1*) and dynamic load P (*2*) at different variants of discharge circuit shown in Figure 1, *a*–*d*, respectively

to 480 V voltage, to inductance of 22.66 μH mounted in the electrode system with a minimum gap between the coil and disc that corresponds to the circuit in Figure 1, *a*. It is seen from the Figure that dynamic load reaches its maximum value before current has reached its highest value. This ratio changes only slightly at increase of inductance from 26.66 to 36.08 μH, obtained by increasing the gap between the coil and disc (Figure 2, *b*) that corresponds to the circuit in Figure 1, *b*. It should be noted that at any values of capacitance and inductance the maximum calculated value of dynamic load is achieved before current has reached its highest value.

Calculated values of current and load, reached at capacitive storage discharge by the circuits shown in Figure 1, *c*, *d* are given in Figure 2, *c*, *d*, respectively. At removal of inductor from the discharge circuit, the current pulse is formed by storage capacitance and parasitic inductance of wires, assumed to be equal to 4 μH in calculations, and reaches its maximum value at 6200 A at the moment of time of 0.125 ms. Leading edge of the pulse is shortened approximately 4 times, compared to the variant shown in Figure 2, *a*, *b*, while the dynamic load pulse is absent. Contrarily, when current passage through the treated metal is eliminated at minimum gap between the disc and inductance, a dynamic load is created (Figure 2, *d*) reaching its maximum at 18,000 N at 0.5 ms duration (inductance L is equal to 26.66 μH). The amplitude does not differ from the variant shown in Figure 2, *a*.

Investigations of the influence of various discharge circuits on parameters P and I were conducted at the value of charging voltage U of capacitive storage device, equal to 480 V. Total capacitance of storage battery of EVOX RIFA 2200 model, included into the discharge circuit, was 6600 μF. Error of measured parameters of electrodynamic impact did not exceed 5 %.

Experimentally derived oscillograms of pulsed current I and dynamic load P at different variants of discharge circuit are given in Figure 3. Figure shows that when basic circuit (see Figure 1, *a*) was used and just the dynamic load (see Figure 1, *d*) was applied, I_{max} values were in the range of 2908–3080 A (Figure 3, *a*, *d*), which can be assumed to be close. Experimental values of I_{max} are below the calculated values, that is attributable to contact resistances of discharge circuit elements, allowing for which is a rather complicated task, going beyond the scope of this study. On the other hand, if maximum value of dynamic load P_{max} for basic variant (Figure 1, *a*) was equal to 20,461 N (Figure 3, *a*), for the variane in which the treated material is excluded from discharge circuit and subjected to just dynamic loading (Figure 1, *d*), P_{max} did not exceed 17,895 (Figure 3, *d*) that is by 15 % lower than the basic one. Experimental P_{max} values are quite close to calculated values that is seen from Figure 2, *a*, *d*. Increased values of P_{max} for the circuit shown in Figure 1, *a*, compared to Figure 1, *d*, are attributable to simultaneous electrodynamic impact on the treated metal of such discharge circuit elements as «inductor + disc» and «electrode + metal». In the variant shown in Figure 1, *d*, action of «inductor + disc» pair is eliminated and metal is exposed to the impact of just the dynamic load. Periods of the time of impact of parameters I and P on the metal for the two considered variants of the circuit were comparable and did not exceed 1.42 and 0.87 ms, respectively (see Figure 3, *a*, *d*).

A different pattern of distribution of I and P values was observed in the absence of dynamic load in those variants of the circuit, when inductor was removed to a distance from the disc (see Figure 1, *b*), as well as completely eliminated from the circuit (see Figure 1, *c*). Periods of action of pulsed current I in the considered circuit variants were close to calculated ones of 1.6–1.8 ms (see Figure 3, *b*, *c*), but in the absence of the inductor maximum value of current amplitude I_{max} was higher, and the speed of its rise and drop was steeper, that can be seen at comparison of curves *1* in Figure 3, *b*, *c*, as well as calculated curves (Figure 2, *b*, *c*). If at inductor removed from the disc (see Figure 1, *b*) maximum current value I_{max} was equal to 2780 A, then at its elimination from the circuit I_{max} value was 6181 A that is close to the calculated value. This is attributable to lower circuit resistance, because of the absence of inductance element. Speeds of current rise and drop in the case of a distanced inductor (Figure 1, *b*) were 8687 and 2138 A/ms, respectively, and at its elimination from the circuit (see Figure 1, *c*) they were 61,810 and 4578 A/ms. Thus, decrease of the considered circuit inductance and storage device energy, respectively, leads to an increase of the speed of pulsed current rise by more than 7 times, and that of its drop — by more than 2 times. Maximum values of dynamic loads P_{max} in the variants of inductor removed to a distance and its elimination reached 7.9 and 23 N, respectively, while the period of their action was 0.16 ms (Figure 3, *b*, *c*, curves *2*). Values of speeds of P rise/drop in Figure 3, *b* (corresponds to the circuit in Figure 1, *b*) were equal to 79 N/ms, and for the circuit in Figure 3, *c* (corresponds to the circuit in Figure 1, *c*) they were 255 N/ms, that corresponds to P_{max} values for the considered circuit variants.

At implementation of circuit variants shown in Figure 1, *b*, *c* (dynamic load is absent), electrodynamic impact is determined by «electrode + metal» pair. In this case, maximum values of pulsed current I_{max}, initiating the electroplasticity mechanisms, correspond to dynamic loads $P = 0$ at inductor L placed at a distance from the disc (see Figure 3, *b*, curves *1*, *2*) and $P = 0.5P_{max}$ with inductor eliminated from the circuit (see Figure 3, *c*, curves *1*, *2*). This results in earlier impact of dynamic load P_{max} relative to current I_{max} at electrodynamic impact, that is in agreement with calculations (Figure 2, *b*, *c*).

At comparison of periods of time $t(I_{max})$ and $t(P_{max})$, corresponding to maximum values of current and load on curves *1* and *2* (see Figure 3, *a*, *d*), a difference from calculated curves is found (Figure 2, *a*, *d*), expressed in delaying of dynamic load impact P_{max} relative to current load I_{max}. Calculated and experimental values of speeds of P rise and drop for circuit variants shown in Figure 1, *a*, *d*, were equal to 37,000 and 40,000 N/ms, respectively, that shows that at the above-mentioned electrical parameters of the circuit the actual load rise is comparable with the calculated values. It should be noted that real ratios of P_{max} and I_{max} in the time scale (Figure 3, *a*, *d*) provide synchronizing of the components of electrodynamic impact on the treated material. Delaying of real rise of dynamic load P compared to the calculated value is related to plastic deformation of the treated surface at its contact interaction with the spherical tip of the electrode at the moment of capacitive storage discharge.

For a more detailed evaluation of electrodynamic impact on the effectiveness of EDT process, treatment was applied to pre-stretched flat samples of aluminium alloy AMg6 and its welded joints with working area dimensions of 150 × × 30 × 4 mm. Samples were loaded in the rupture machine of «rigid» type with maximum tensile force of 98,000 N at deformation rate of 0.1 mm/s and temperature of 293 K. EDT was performed by series of five current discharges at pulse ratio of 60 s in the mode, taken for investigations of discharge circuit variants (see Figure 3).

Influence of electrodynamic impact on lowering of material resistance to deformation, $\Delta\sigma$, was evaluated at different variants of the circuit. Initial value of tensile stress σ_0 was taken equal to 150 MPa, at which, according to the data of [7], maximum values of EDT effectiveness — $\Delta\sigma/\sigma_0$ — are achieved at the above-mentioned mode parameters.

Three variants of discharge circuit were used (Figure 4). In the first variant (Figure 4, *a*) EDT effectiveness was determined by interaction of such circuit elements as «inductor + disc» and «electrode + metal sample». In the second variant of the circuit (Figure 4, *b*) $\Delta\sigma/\sigma_0$ values were determined by electrodynamic interaction of element pair of «electrode + metal samples», and in the third variant (Figure 4, *c*) — by electrodynamic interaction of «inductor + disc» elements.

Values $(\Delta\sigma/\sigma_0)\cdot 100$ % after EDT of samples of AMg6 alloy and its welded joints, implemented with different variants of discharge circuit, are shown in Figure 5, from which it is seen that action of just the pulsed current (curves *1* and *1′* correspond to the circuit in Figure 4, *b*)

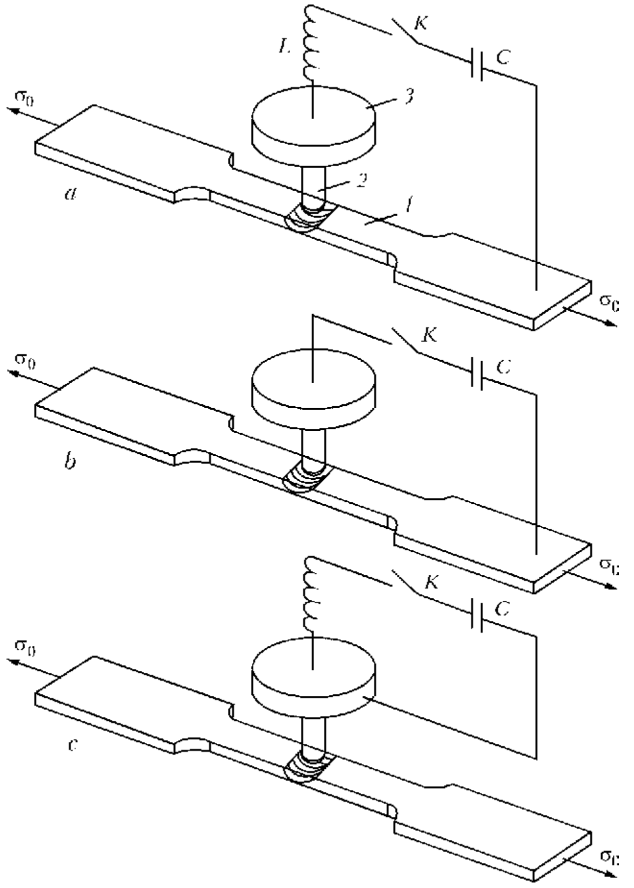

Figure 4. Circuits of EDT of AMg6 alloy and its welded joints (for *a*–*c* see the text)

does not have any significant influence on deformation resistance, and, consequently, on EDT effectiveness. At comparison of $(\Delta\sigma/\sigma_0)\cdot100$ % values, resulting from EDT under the conditions of dynamic load (curves *2* and *2′* correspond to the circuit in Figure 4, *c*), and at interaction of pulsed current and dynamic load (curves *3* and *3′* correspond to the circuit in Figure 4, *a*), one can see that EDT effectiveness at dynamic load has lower values. EDT of base metal is less effective compared to EDT of welded joints that is seen from comparison of curves *1*–*3* and *1′*–*3′*. This is related to presence of residual stresses in welded joint samples, and in [7] it is shown that effectiveness of electrodynamic impacts depends on values of elastic tensile stresses in the material, subjected to EDT.

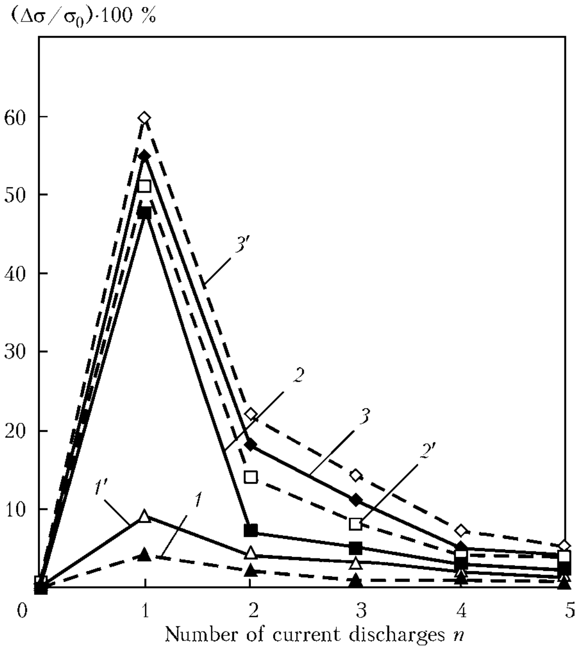

Figure 5. Influence of discharge circuit on relative effectiveness of EDT $(\Delta\sigma/\sigma_0)\cdot100$ % of AMg6 alloy and its welded joints (for designations see the text)

Increase of EDT effectiveness at interaction of current and dynamic components, compared to dynamic load, is attributable to interaction of conduction electrons with dislocation clusters during the action of current pulse [8]. Dynamic load, value of which at the above-given charging voltage is equal to 20,460 N, creates the conditions for dislocation clusters overcoming the barriers. Pulsed current provides dislocation displacement by the electron flow at its impact on the metal. Thus, the impact of just the pulsed current without the influence of dynamic load is capable of unpinning the dislocation clusters from stoppers in the material microvolume, but is insufficient for initiating a jump of stresses $\Delta\sigma$ over the entire cross-section of the sample (Figure 5, curves *1* and *1′*). Dynamic load (Figure 5, curves *2* and *2′*) promotes dislocation clusters overcoming the barriers over the entire section of the sample during the first current discharge ($n = 1$ in Figure 5), but its effectiveness essentially decreases at subsequent discharges. This is attributable to the fact that at $n = 1$ the dynamic impact energy ensures overcoming of barriers for dislocation clusters of finite density. The metal preserves stable dislocation groups, the density of which exceeds the energy capabilities of dynamic load that makes low-effective the current discharges $n = 2$–5 in Figure 5. At the same time, dynamic impact is characterized by the required potential for dislocation unpinning from the stoppers, but is insufficient for their displacement. This assumption is supported by the difference in effectiveness data in the sections of curves *2*–*2′* and *3*–*3′* at $n = 2$–5 in Figure 5. Pulsed current promotes displacement of dislocations unpinned from the stoppers by dynamic load at $n = 2$–5 that enables exceeding $(\Delta\sigma/\sigma_0)\cdot100$ %. This is seen at comparison of curves *3*–*3′* and *2*–*2′*. If dynamic load does not provide dislocation unpinning from the stoppers after the first current discharge ($n = 1$), then curves *2*–*2′* and *3*–*3′* coincide during the entire treatment cycle, i.e. at $n = 1$–5 in Figure 5. Thus, pulsed current is not the only parameter determining EDT effectiveness. This mechanism is described in [9] for the case of jump-like deformation of aluminium.

For evaluation of dynamic loads initiated by electrodynamic impact, distribution of longitudinal deformation waves was studied at different variants of the discharge circuit corresponding to those shown in Figure 4, *a*, *b*. Investigations were performed using a flat sample of welded joint of AMg6 alloy, on the surface of which a strain gauge with 10 mm base was placed along the central longitudinal axis at 70 mm distance from the center of the sample, the surface of which was treated by single current discharge in the mode corresponding to charging voltage of 480 V. Sensor readings were recorded with two-channel digital oscillograph PCS Welleman at 0.1 ms scan.

Values of deformation waves ε_{EDT} initiated by dynamic load (without current impact) and electrodynamic impact are given in Figure 6. From the Figure one can see that maximum range of wave amplitude, which is equal to 0.0042, corresponds to electrodynamic impact (curve *2*). No residual plastic deformation was recorded in the strain gauge measurement zone. This is confirmed by the results given in [7], where it is stated that the region of plastic deformation at EDT is localized in the zone of electrodynamic impact.

As is seen from Figure 6, the periods of rise of primary deformation wave for the two variants of the circuit, are equal to each other, being 0.05 ms. Here, the speed of deformation wave rise at dynamic load (curve *1*) is equal to 0.04 ms, and at electrodynamic impact (curve *2*) it reaches 0.049 ms. Higher speed of wave rise achieved under the conditions of current flowing through the sample, ensures maximum values of tensile deformations of 0.0024 (curve *2*). At sample exclusion from discharge circuit stress value was not higher than 0.002 (curve *1*). More noticeable is the influence of pulsed current in the flat region of primary wave drop, where the difference of values of tensile deformations on curves *1* and *2* was up to 0.0007 during 0.12 ms.

Results of conducted investigations lead to the conclusion that pulsed current treatment has the smallest influence on lowering of residual stresses in welded joints of AMg6 alloy. More effective is the impact of dynamic load realized without pulsed current passage through the treated material. The highest effectiveness of EDT is found at pulsed current passage through the material, at its simultaneous action with the dynamic load on samples with welded joint. Thus, such an impact is preferable at EDT of welded joints of sheet structures from aluminium alloys.

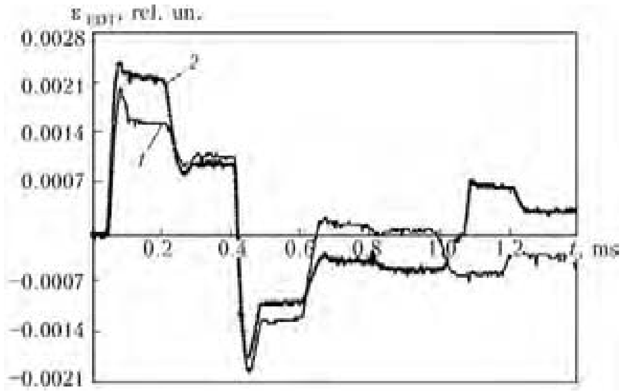

Figure 6. Values of deformation waves ε_{EDT} initiated by dynamic load (*1*) and electrodynamic impact (*2*)

1. Lobanov, L.M., Pashchin, N.A., Loginov, V.P. et al. (2005) Application of electric pulse treatment of structural elements to extend their service life (Review). *The Paton Welding J.*, **11**, 19–23.
2. Stepanov, G.V., Babutsky, A.I., Mameev, I.A. et al. (2011) Redistribution of residual welding stresses after treatment by pulsed electromagnetic field. *Problemy Prochnosti*, **3**, 123–131.
3. Lobanov, L.M., Pashchin, N.A., Cherkashin, A.V. et al. (2012) Efficiency of electrodynamic treatment of aluminium alloy AMg6 and its welded joints. *The Paton Welding J.*, **1**, 2–6.
4. Baranov, Yu.V., Troitsky, O.A., Avramov, Yu.S. et al. (2001) *Physical principles of electric pulse and electric plastic treatments and new materials*. Moscow: MGIU.
5. Lobanov, L.M., Pashchin, N.A., Skulsky, V.M. et al. (2006) Influence of electrodynamic treatment on the stress-strain state of heat-resistant steels. *The Paton Welding J.*, **5**, 8–11.
6. Aleksandrov, G.N. (1985) *Theory of electric apparatuses*. Moscow: Vysshaya Shkola.
7. Lobanov, L.M., Pashchin, N.A., Loginov, V.P. et al. (2007) Change of the stress-strain state of welded joints of aluminium alloy AMg6 after electrodynamic treatment. *The Paton Welding J.*, **6**, 7–14.
8. Strizhalo, V.A., Novogrudsky, L.S., Vorobiov, E.V. (2008) *Strength of materials at cryogenic temperatures taking into account the action of electromagnetic fields*. Kiev: IPP.
9. Bobrov, V.S., Lebedkin, M.A. (1989) Electric effects at low-temperature jump deformation of aluminium. *Fizika Tv. Tela*, 31(**6**), 120–124.

PECULIARITIES OF LASER-ARC WELDING OF TITANIUM ALLOYS

V.D. SHELYAGIN, V.Yu. KHASKIN, S.V. AKHONIN, V.Yu. BELOUS, I.K. PETRICHENKO, A.V. SIORA, A.N. PALAGESHA and **R.V. SELIN**
E.O. Paton Electric Welding Institute, NASU, Kiev, Ukraine

Methods were developed, and parameters were selected for hybrid laser-arc welding. It was established that hybrid laser-arc welding allows producing joints on low and medium titanium alloys with properties that are not inferior to those of the base metal. Impact toughness of the hybrid laser-arc welded joints on high titanium alloy T110 is much higher than that of the laser welded joints.

Keywords: *hybrid laser-arc welding, laser radiation, tungsten-electrode arc, titanium alloys, experiments, parameters, metallography, structures, mechanical properties*

At present titanium alloys are applied for fabrication of critical structures operating in aerospace engineering, chemical industry, instrument making and ship building. They are used to manufacture such critical parts as stringer panels for aircraft, rocket components, tanks for chemical industry, casing parts, etc. [1]. Often the design solutions these parts are based on require the use of welding processes. In practice, more than 90 % of all the welds are made by argon-arc and electron beam welding [2].

However, these welding methods have drawbacks of both technological (low power density in the arc discharge plasma) and economical character (high cost even at small dimensions of the majority of vacuum chambers for electron beam welding). Laser welding has been gaining acceptance lately, which is due to its advantages, such as high power density in the laser beam, high productivity and precision of processing [3]. A substantial drawback of the process of laser welding is a high cost of the equipment involved. As shown in study [4], one of the ways of reducing this indicator is partial replacement of the laser power by the arc one. Moreover, laser welding also has some technological limitations related to a high reflection power of surfaces of many structural metals and alloys. However, it can be overcome by using the hybrid laser-arc process.

The work on hybrid laser-arc welding of steels and aluminium alloys has been performed for about three decades (e.g. [5]). The discussions are underway for the last ten years concerning the possibility of applying it for titanium alloys [6], and corresponding experimental data have been accumulated. The issue of the highest current importance is determination of the effect of the thermal cycle of hybrid laser-arc welding on properties of the joints on high-strength titanium alloys, for example, such as T110. In particular, under conditions of the experiment described in study [7], laser welding of alloy T110 led to deterioration of its mechanical properties compared to the base metal.

The purpose of the present study was to investigate peculiarities of laser-arc welding of joints on titanium alloys, such as low titanium alloy VT6 and high-strength alloy T110, as well as to evaluate mechanical properties of the resulting welded joints.

To solve this problem, the authors implemented the flowchart of the hybrid laser-arc welding process shown in Figure 1. The radiation source was Nd:YAG-laser DY 044 (Rofin Sinar, Germany) with a power of up to 4.4 kW and wavelength of 1.06 μm, and the welding current source was power supply VDU-601 UZ for automatic TIG welding. According to this flowchart, the tungsten electrode is located ahead of the laser beam. This combination of laser and TIG welding makes it possible to increase the penetrating power of the welding process and permits a simple feed of the filler wire to the welding zone. To implement this flowchart, a welding head was developed to provide feed of laser beam *1* focused by the lens (focal distance — 300 mm) and tungsten electrode *7* (diameter — 5 mm, sharpening angle — 30°) to a certain point on the surface of specimen *5* being welded. The distance from the electrode tip to the surface of the welded specimen was set at about 3 mm. The distance from the exit section of the lower part of the welding head to the specimen was the same. Deepening of the focal plane of the laser

© V.D. SHELYAGIN, V.Yu. KHASKIN, S.V. AKHONIN, V.Yu. BELOUS, I.K. PETRICHENKO, A.V. SIORA, A.N. PALAGESHA and R.V. SELIN, 2012

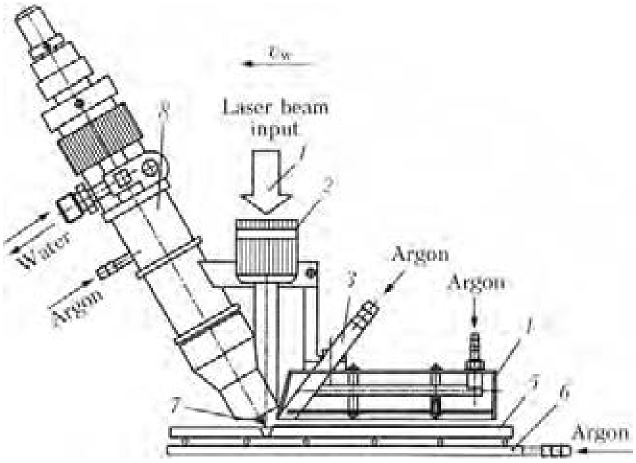

Figure 1. Flowchart of the hybrid laser-arc welding process: *1* — laser beam; *2* — focusing device; *3* — device for additional feed of shielding gas; *4* — device for shielding of the welding zone and cooling weld and HAZ metals; *5* — welded specimen; *6* — device for shielding of reverse side of the joint; *7* — tungsten electrode; *8* — welding head for TIG welding of titanium

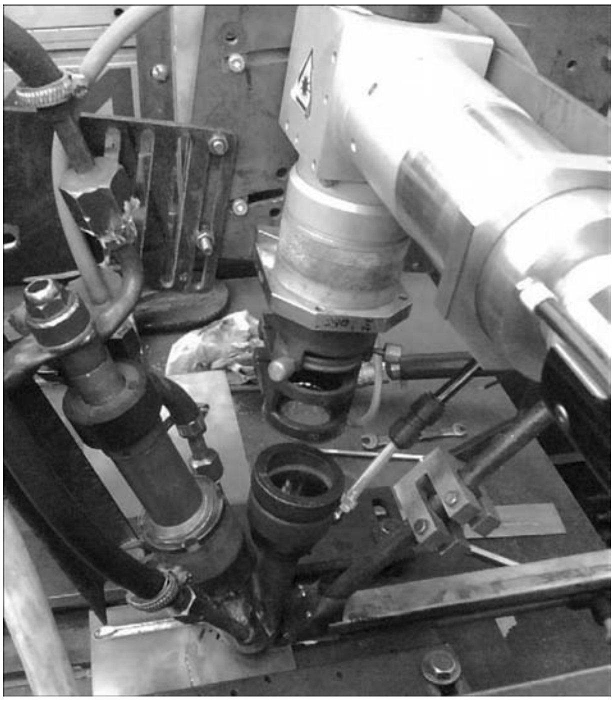

Figure 2. Appearance of the welding head for laser-arc welding of titanium alloys

beam to under the surface of the welded specimen was varied within 0–5 mm, depending on its thickness. The angles between the normal to the surface welded and axes of the laser beam and electrode were chosen to be as small as possible. The experiments showed that to provide the hybrid effect in welding the distance between the laser beam axis and the electrode tip should be 1.0–1.5 mm. Melting and fracture of the tungsten electrode tip take place at a distance between the laser beam axis and the electrode tip less than 1 mm. If this distance is more than 3 mm, after the effect exerted by the tungsten electrode arc the solidified weld metal is subjected to repeated penetration by the laser beam, no substantial increase in the penetrating power of the laser-arc process being fixed in this case.

Increase in the penetration depth was achieved when the tungsten electrode welding arc was the first in the direction of welding (Figure 2), which provided augmentation of the laser radiation absorbed by metal, as the molten metal has a better absorptive capacity than the cold one [8]. In the experiments the welding current was varied within 200–450 A, the radiation power of the Nd:YAG-laser being 4.4 kW. Titanium alloys VT1, VT6 and T110 with thickness δ = 10–13 mm were used as specimens. The shielding gas (argon) was fed both from top and bottom of a specimen. To ensure quality shielding of the welding zone, the welding head was fitted with a device for additional blowing of the tailing part of the weld pool with argon (Figure 1, pos. *3* and *4*).

The experiments conducted made it possible to establish that the laser-arc method can be applied to weld 12 mm thick titanium alloys with through penetration at a speed of 22–24 m/h, radiation power of 4.4 kW, welding current of 400 A and voltage of 12–14 V (Figures 3, *a*; 4, *a*; 5, *a*). The weld bead deposited on the same alloys under the above conditions separately by the laser and arc methods had a depth of about 6 and 5 mm, respectively (Figures 3, *b*; 4, *b*; 5, *b*). Comparison of cross section areas of these welds with the welds made by the hybrid method allows a conclusion that the hybrid effect takes

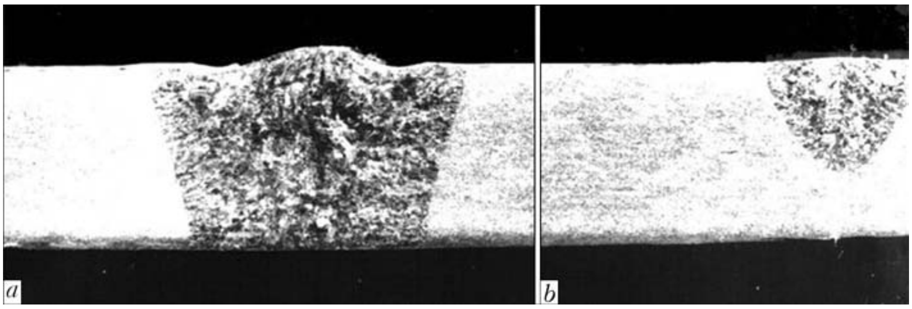

Figure 3. Macrostructures of welds on titanium alloy VT6 (δ = 10 mm): *a* — laser-arc welding; *b* — laser welding

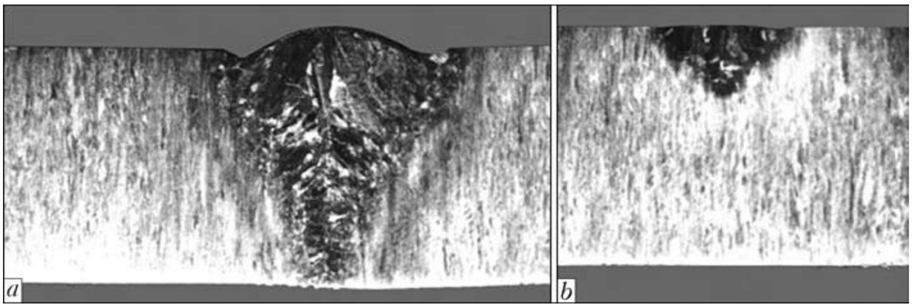

Figure 4. Macrostructures of welds on titanium alloy VT6 (δ = 13 mm): *a* — laser-arc welding; *b* — laser welding

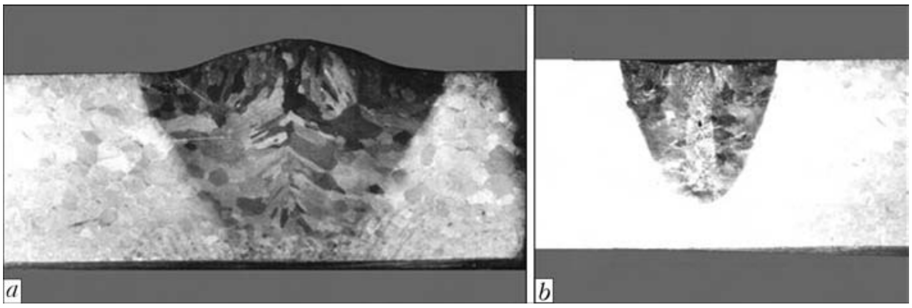

Figure 5. Macrostructures of welds on titanium alloy T110 (δ = 13 mm): *a* — laser-arc welding; *b* — laser welding

place in the laser-arc welding process. It shows up in non-additivity of the sum of the cross section areas of the welds made by the laser and arc methods, compared to the areas of the welds made by the hybrid method. Parameters of the welds on alloys VT6 and T110 in laser and laser-arc welding are given in Table 1.

Main drawbacks of the methods of laser and hybrid laser-arc welding of titanium alloys include the probability of formation of internal pores in the cast weld metal and unsatisfactory formation of the upper reinforcement bead. The latter defect consists in formation of undercuts on two sides of the weld and some increase in the reinforcement bead proper.

Metallographic examinations of the welds on alloys VT6 and T110 made by laser welding showed a clearly defined dendritic structure with primary β-grains seen against its background, the grains being elongated in a direction of heat removal or equiaxed. The substructure was fixed too. In laser-arc welding of alloys VT6 and T110, mostly β-grains elongated in a direction of heat removal were formed in the weld, while relatively

Table 1. Parameters of the welds and HAZ in laser and laser-arc welding

Alloy	Welding method	Weld shape	Penetration depth, mm	Weld width, mm			HAZ width, mm		
				Upper part	Midsection	Root part	Upper part	Midsection	Root part
VT6	Laser	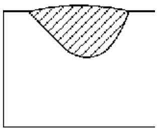	4.0	7.0	2.5	–	1.2	1.8	0.7
	Laser-arc	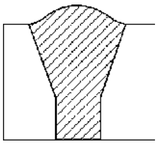	13.0 (through)	12.0	5.0	2.3	1.8	4.3	2.3
T110	Laser	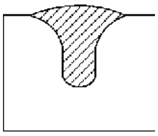	6.9	8.0	1.5	1.9	1.2	3.3	0.9
	Laser-arc	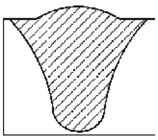	11.0	12.0	5.4	3.4	2.3	4.5	2.5

Table 2. Mechanical properties of alloy VT6 and its laser-arc welded joints

Material	Tensile strength, MPa	Ductility limit, MPa	Elongation, %	Reduction in area, %	Impact toughness, J/cm^2	
					Weld	HAZ
Base metal VT6 (δ = 13 mm)	888	815	13.6	30	39	
Welded joint	911	–	–	–	54	32

Table 3. Mechanical properties of alloy T110 and its laser and laser-arc welded joints

Material	Tensile strength, MPa	Ductility limit, MPa	Elongation, %	Reduction in area, %	Impact toughness, J/cm^2	
					Weld	HAZ
Base metal T110 (δ = 13 mm)	1130	999	6	5	38	
Welded joint:						
laser-arc	1180	–	–	–	15	23
laser	1131	–	–	–	6	13

fine equiaxed grains were fixed only in the upper part of the weld near the surface.

In contrast to the welded joints on alloy T110 made by laser welding, no substructure was detected either in the weld or in the HAZ of the laser-arc welded joints, the microstructure being more homogeneous and uniform. Examination of microstructure of transverse sections of the welded joints showed that the laser welds had pores with a diameter of 0.010–0.035 mm, whereas the laser-arc welds were free from pores.

As shown by mechanical tests, the tensile strength values of the laser and laser-arc welded joints on alloys VT6 and T110 were 2–4 % higher than those of the base metal (Tables 2 and 3), which, in the authors' opinion, can be explained by the presence of the dendritic structure in the weld metal, which is characteristic of a cast metal. Measurements of impact toughness of the laser-arc welded joints on titanium alloy T110 showed the satisfactory values.

Because of peculiarities of laser and laser-arc welding characterised by an evaporating mechanism of the keyhole formation, the welded joints were investigated to determine the content of alloying elements in the cast weld metal and compare it to the content of such elements in the base metal. Investigations of chemical microheterogeneity in specimens of alloy T100 welded by the laser and laser-arc methods were carried out to determine the content of aluminium, niobium, zirconium, molybdenum, vanadium and iron by using CAMECA scanning microscope-microanalyser SX-50. The instrument comprised an electron probe consisting of an electron beam 1 μm in diameter. The volume of the determined mass was 1–3 μm^3, depending on the depth of penetration of the probe into the material studied. It was found that both in laser welding and in hybrid welding the deviation of the content of the investigated elements was within the permissible scatter for alloying elements in the grade composition of the alloy. Therefore, in welding under the indicated conditions there is no risk of burning out of individual alloying elements of the alloy.

CONCLUSIONS

1. The welding head was designed for hybrid laser-arc welding (beam + TIG) of titanium alloys, wherein the laser beam was located behind the welding arc. This welding head provides the satisfactory quality of shielding of the welding zone and cooling weld metal.

2. The use of the proposed flowchart of laser-arc welding at a laser beam power of 4.4 kW and welding current of 400 A was found to provide a twofold increase in the penetration depth, compared to the results of using only laser welding performed at a power of 4.4 kW. Both in laser welding and in laser-arc welding there is no risk of burning out of alloying elements.

3. The technological approaches were developed, and parameters of laser-arc welding were selected to provide through penetration of specimens of titanium alloys VT6 and T110 with thickness of up to 13 mm at a laser beam power of 4.4 kW and welding speed of 22–24 m/h.

4. Tensile strength of the laser and laser-arc welded joints on titanium alloys VT6 and T110 was 2–4 % higher than that of the base metal.

5. Laser-arc welding is characterised by a higher penetrating power compared to welding only with the laser beam, and provides the welded joints on high titanium alloys with satisfactory ductility and impact toughness.

6. As shown by the investigations, hybrid laser-arc welding allows producing the welded joints on low and medium titanium alloys with properties that are not inferior to properties of the base metal.

1. Gurevich, S.M., Zamkov, V.N., Blashchuk, V.E. et al. (1986) *Metallurgy and technology of welding of titanium and its alloys*. Kiev: Naukova Dumka.
2. Nazarenko, O.K., Kajdalov, A.A., Kovbasenko, S.N. et al. (1987) *Electron beam welding*. Ed. by B.E. Paton. Kiev: Naukova Dumka.
3. Paton, B.E., Shelyagin, V.D., Akhonin, S.V. et al. (2009) Laser welding of titanium alloys. *The Paton Welding J.*, **7**, 30–34.
4. Shelyagin, V.D., Khaskin, V.Yu., Garashchuk, V.P. et al. (2002) Hybrid CO_2-laser and CO_2 consumable-arc welding. *Ibid.*, **10**, 35–37.
5. Matsuda, J., Utsumi, A., Katsumura, M. et al. (1988) TIG or MIG arc augmented laser welding of thick mild steel plate. *Joining and Materials*, 1(**1**), 31–34.
6. Brandizzi, M., Mezzacappa, C., Tricarico, L. et al. (2010) Ottimizzazione dei parametri di saldatura ibrida laser-arco della lega di titanio Ti6Al4V. *Rivista Ital. Saldatura*, **2**, 77–85.
7. Topolsky, V.F., Akhonin, S.V., Shelyagin, V.D. et al. (2010) Laser welding of structural titanium alloys. *Teoriya i Praktika Metallurgii*, **5/6**, 22–27.
8. Grigoriants, A.G., Shiganov, I.N. (1988) *Laser technique and technology*: Tutorial. Book 5: Laser welding of metals. Ed. by A.G. Grigoriants. Moscow: Vysshaya Shkola.

CORROSION-FATIGUE STRENGTH OF 12Kh18N10T STEEL T-JOINTS AND METHODS OF ITS IMPROVEMENT

E.V. KOLOMIJTSEV
Ilyich Mariupol Metallurgical Works, Mariupol, Ukraine

Results of fatigue testing the T-joints of stainless steel 12Kh18N10T in air and in corrosion medium are given, and the effect of surface strengthening on improvement of strength properties and fatigue life of welded elements of hydrofoil wing ship assemblies is also determined.

Keywords: *arc welding, MMA welding, TIG welding, stainless steel, welded joints, corrosion medium, fatigue strength, fatigue life, surface strengthening, residual stresses*

The stainless steel of the austenite class of the grade 12Kh18N10T is widely used in manufacture of different welded structures which in process of operation are subjected to influence of the alternate loads. They include foil systems (FS) of foilcrafts (FC), rollers of heating furnaces of metallurgy enterprises, welded components of products of chemical and power machine building.

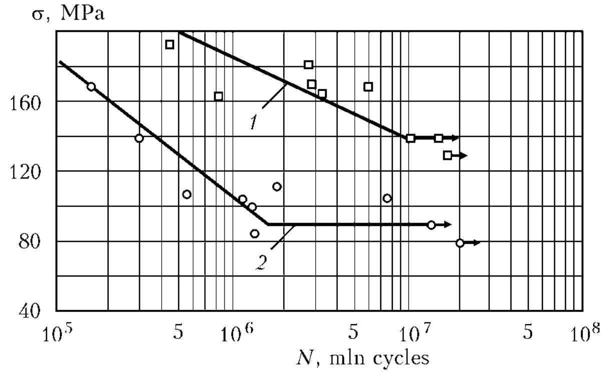

Figure 1. Curves of fatigue of manual welded T-joints: *1* — initial state after welding; *2* — after strengthening using BPS

© E.V. KOLOMIJTSEV, 2012

In this study the results of fatigue tests of T-joints of steel 12Kh18N10T in air and sea water both in as-welded state, as well as after strengthening treatment applying ball-pin strengthener (BPS).

The experience of service of vessels of the type «Kometa» showed [1, 2] that in FS the cracks are formed on the planes of wings, at the places of joining the bracket with the wing plane, in brackets of propeller shafts. During operation under conditions of the Azov sea, the cracks in ships «Kometa» and «Kolkhida» are formed during 1.5–2 months after repair and after 2–3 weeks under the conditions of the Black Sea. They have to be eliminated by grooving and re-welding of defective places that is accompanied by significant expenses connected both with the repair itself, and also at taken the ship from the service in the navigation period.

The fatigue life of FS can be increased by the new constructive solutions or by technological operations, which include in particular the strengthening treatments which create compressive stresses in the surface layers [3, 4].

The purpose of this work is to evaluate the effect of strengthening treatment on the fatigue life and strength of FS of the ships of the «Kometa» type.

For this purpose the specimens with T-joints were manufactured of sheet rolled metal of steel

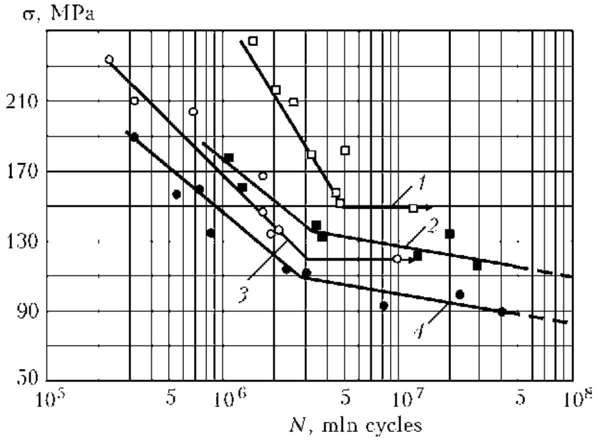

Figure 2. Curves of fatigue of TIG-welded T-joints: *1* — after strengthening applying BPS (air); *2* — after strengthening (sea water); *3* — initial state after welding (air); *4* — initial state (sea water)

12Kh18N10T of 12 mm thickness and welded using manual welding with electrodes EA-400/10U and also argon arc welding with filler wire Sv-04Kh19N11M3.

Steel 12Kh18N10T has the following chemical composition, wt.%: 0.09 C; 1.52 Mn; 0.71 Si; 18.4 Cr; 10.2 Ni; 0.19 Cu; 0.76 Ti; 0.08 S; 0.018 P, and mechanical properties $\sigma_t =$ $= 588$ MPa; $\sigma_y = 363$ MPa; $\delta = 55$ %.

The tests were carried out using resonance installations at console bending by a symmetric cycle. The frequency of loading was 35–45 Hz. The width of test part of the specimens was 100 mm [5]. The base of tests in air was 10^7, in corrosion medium (sea water) — $3\cdot10^7$ cycles. The fatigue strength obtained at this base was extrapolated according to the equation of the second region of a corrosion fatigue curve to base of 10^8 cycles [6].

In total six batches of specimens were tested, ten pieces in each one. Weld and near-weld zone of width of up to 15 mm on the both sides of a weld were subjected to strengthening. The fractured specimens of post-fatigue tests were used to manufacture sections on which the location of a crack as well as depth of strengthened layer were determined. In surface layers subjected to strengthening the microhardness of cold-worked metal was 3220–4240 MPa, whereas of non-cold-worked layer was 2460–3010 MPa, and depth of strengthened layer was 2 mm.

Test results showed the following. The fatigue strength at tests of specimens made by the manual welding in air (Figure 1) increased from 90 to 140 MPa after strengthening, i.e. 1.5 times, the fatigue life at stresses 140–180 MPa increased 14–20 times.

Fatigue strength of specimens, made by argon arc welding, increased from 120 to 150 MPa at tests in the air, i.e. 1.25 times, and fatigue life at stresses 150–230 MPa increased 4–8 times (Figure 2, curves *1*, *3*). The fatigue strength in corrosion medium on base of 10^7 cycles increased from 100 up to 127 MPa, i.e. 1.3 times (Figure 2, curves *2*, *4*), fatigue life at stresses 120–140 MPa increased 4–13 times; on the base of $3\cdot10^7$ cycles — from 93 to 120 MPa (1.3 times), fatigue life — 3–13 times; on base of 10^8 cycles (extrapolation) — from 83 up to 100 MPa (1.35 times), fatigue life at stresses 110–120 MPa — 14–30 times.

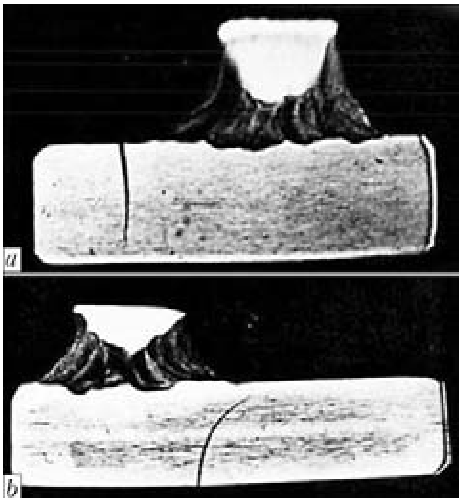

Figure 3. Location of fatigue cracks in welded specimens without strengthening (*a*) and after strengthening using BPS (*b*)

As is seen from Figure 3, on the specimen passed strengthening the crack initiated and propagated not in the place of weld transition to the base metal (as usual), but on the opposite side. Probably this fact was observed for the first time.

The above-given data are differed from those obtained by us earlier [7], i.e. the effect from inducing of compressive stresses in surface layers by plastic deformation is higher manifested on steel 12Kh18N10T than on steel 15G2FB, and on T-joints it was manifested to a larger extent than on the butt ones.

The results, given in this work, allow recommending the ship owners of FC to use the strengthening treatment using BPS to increase fatigue life and strength of FS of ships of «Kometa» type that will decrease the expenses for repair and increase the reliability of ships of this class.

CONCLUSIONS

1. Fatigue strength of T-joints of steel 12Kh18N10T, made by manual and argon arc welding, on base of 10^7 cycles was 90 and 120 MPa, respectively.

2. Corrosion-fatigue strength of 12Kh18N10T steel T-joints, made by argon arc welding, on base of 10^7 cycles was 100, on base of 10^8 — 83 MPa.

3. Plastic deformation using BPS increased the fatigue strength of steel 12Kh18N10T T-joints up to 140 and 150 MPa for manual and argon arc welding, respectively: fatigue life — 4–8 times for TIG-welded joints and 14–20 times for manual welded joints; corrosion-fatigue strength was increased up to 127 MPa on base of 10^7 cycles and up to 110 MPa on base of 10^8 cycles, i.e. 1.3 times; fatigue life at stresses 110–120 MPa was 14–30 times increased.

4. Hardening treatment of FC FS using BPS can be recommended to implementation at ship repair enterprises.

1. Ziganchenko, P.P., Kuzovenkov, B.P., Tarasov, I.K. (1981) *Hydrofoil ships (design and strength)*. Leningrad: Sudostroenie.
2. Kuzovenkov, B.P. (1968) Some informations about damageability of foil systems. In: *Trudy NTO Sudproma*, Issue 101.
3. Stepanov, V.G., Klestov, M.I. (1977) *Surface strengthening of hull structures*. Leningrad: Sudostroenie.
4. Olejnik, N.V., Kychin, V.P., Lugovskoj, A.L. (1984) *Surface dynamic strengthening of machine parts*. Kiev: Tekhnika.
5. Kolomijtsev, E.V., Serenko, A.N. (1985) Experimental evaluation of fatigue resistance of low alloy steel butt joints in corrosion medium. *Avtomatich. Svarka*, **4**, 49–52.
6. Kolomijtsev, E.V., Karpov, I.V. (1986) To choice of test base of hull plates on fatigue corrosion. *Sudostroenie*, **10**, 39–40.
7. Kolomijtsev, E.V., Serenko, A.N. (1990) Influence of ultrasonic and laser treatments on fatigue resistance of welded butt joints in air and corrosive medium. *Avtomatich. Svarka*, **11**, 13–15.

INFLUENCE OF CONTENT OF IRON POWDER AND COMPOUNDS OF ALKALI METALS IN THE COMPOSITION OF ELECTRODE COATING ON THEIR SANITARY-HYGIENIC CHARACTERISTICS

I.K. POKHODNYA, I.R. YAVDOSHCHIN and **I.P. GUBENYA**
E.O. Paton Electric Welding Institute, NASU, Kiev, Ukraine

The dependence of the specific precipitations and chemical composition of a hard component of welding aerosol on content of iron powder in electrode coating was established. The effect of content of potassium compounds in coating of rutile and basic electrodes on their sanitary-hygienic characteristics was considered.

Keywords: *manual arc welding, electrodes, electrode coating, welding aerosol, coating composition, sanitary-hygienic characteristics, hard component, specific precipitations*

The manual arc welding with coated electrodes is challenging today and according to the forecasts of the specialists [1, 2] it will continue its existence due to a number of advantages, such as relatively moderate price of the process and consumable materials, possibility of welding in all positions and in hard-to-access places, lack of rigid requirements to welder skills. At the same time, already more than 50 years the searches for ways to improve the sanitary-hygienic characteristics of electrodes are being continued.

Table 1. Conditions of welding using coated electrodes of DZ series

Electrode index	U_w, V
DZ-0	26–28
DZ-1	26–28
DZ-2	25–27
DZ-3	24–26
Note. Welding current of 180 A.	

The factors were determined influencing the evolution of aerosol [3], which consists of a gas-like component of welding aerosol (GCWA) and a hard component of welding aerosol (HCWA). One of the main factors defining the level of specific precipitations and chemical composition of HCWA is composition of electrode coating as far as during heating and melting it is the main source of aerosol, i.e. 35–70 % of the total volume depending on the type of electrode coating [3, 4].

The iron powder, widely used in production of coated electrodes, allows enhancing labor productivity of welder, decreasing the cost of welding works, improving welding-technological properties of electrodes [5]. The increase of productivity is achieved due to increase of transfer

© I.K. POKHODNYA, I.R. YAVDOSHCHIN and I.P. GUBENYA, 2012

Table 2. Chemical composition of HCWA compounds of ANO-37 series electrodes with rutile coating, wt.%

Electrode index	Na_2O	SiO_2	TiO_2	MnO	Fe_2O_3	CaO	K_2O	Al_2O_3	P_2O_5	SO_3
DZ-0	2.85	18.20	2.91	11.08	50.28	0.53	13.03	0.17	0.60	0.38
DZ-1	2.73	22.38	2.76	8.94	51.87	0.56	9.68	0.18	0.51	0.35
DZ-3	2.65	22.73	2.11	6.50	50.80	0.48	13.60	0.16	0.50	0.50

of a metallic component of the electrode coating into the weld pool.

The investigation of effect of iron powder content in electrode coating on the sanitary-hygienic characteristics was carried out basing on the electrodes ANO-37 with rutile type of coating (the first series of experiments). The four batches of experimental electrodes with content of iron powder of 0, 10, 20, 30 wt.% (index of electrodes DZ-0, DZ-1, DZ-2, DZ-3, respectively) were manufactured.

The welding was carried out in a chamber [4] from the AC power source, i.e. transformer STSh-500 (Table 1). The sanitary-hygienic properties were evaluated in the following way: welding aerosol, formed in the chamber in the process of welding, was precipitated by a complete filtration on filters FPP-15-1.5, which were weighed before and after precipitation. The obtained difference in mass related to the mass of burnt-out part of electrode or time of arc burning represents the specific precipitations (D, g/kg) or intensity of precipitation (G, g/min) of HCWA, respectively.

Also, by precipitation of aerosol on cellulose filter and its mechanic removal into glass vessel the HCWA was additionally sampling for chemical analysis using method of X-ray fluorescent spectrometry (SRM-25) (Table 2, Figure 1).

The results of experiments prove the significant (more than 20 %) decrease of precipitations of HCWA due to adding of iron powder into electrode coating. This is explained by the following factors: change in temperature of a drop at the electrode tip [4], general relative decrease of components of electrode coating, actively participating in formation of welding aerosol (cellulose, ferromanganese, marble) which leads to a considerable decrease (almost twice) in content of toxic compound of manganese in the composition of HCWA (Table 2). The tests of welding technological properties of electrodes were also carried out which gave good results, as the addition of iron powder did not deteriorate the behavior of metal and slag in welding and did not influence the slag removal and metal formation.

The compounds of alkali metals in the composition of electrode coating can be in a form of a binder (water-soluble silicates) and also as a stabilizing component as they have low electronic work function.

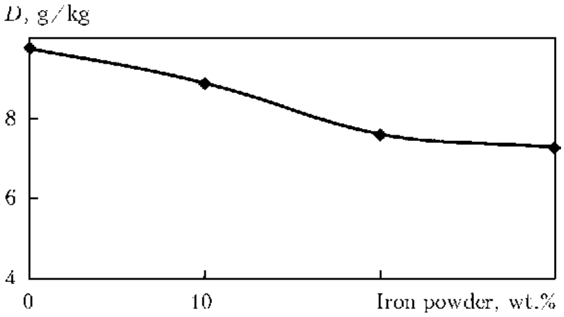

Figure 1. Dependence of specific precipitation of HCWA on the content of iron powder in electrode coating

Table 3. Composition of components in the coating in rutile electrodes, wt.%

Coating components	E1	E2	E3	E4	E5
Potassium titanate	–	–	4	8	12
Iron powder	10	10	6	2	–
Type of liquid glass	Na	K	K	K	K

Table 4. Conditions of welding using coated electrodes of series E

Electrode index	U_w, V
E1	26–28
E2	24–26
E3	21–23
E4	20–22
E5	20–22
Note. Welding current of 185 A.	

Table 5. Chemical composition of HCWA compounds of series E electrodes with rutile coating, wt.%

Electrode index	K_2O	SiO_2	TiO_2	MnO	MgO	CaO	Fe_2O_3
E1	4.46	11.70	2.82	16.30	1.72	0.54	49.10
E2	9.75	16.30	3.44	16	1.72	0.50	48.60
E3	13.04	13.60	3.77	14.70	1.69	0.50	45.60
E4	14.40	15	3.46	13	1.58	0.59	45.90
E5	22.40	11.73	3.43	9	1.51	0.40	47.90

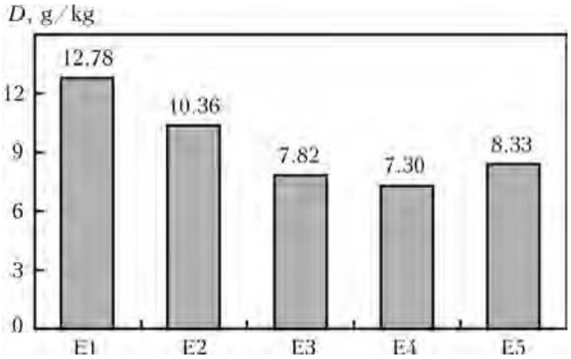

Figure 2. Specific precipitation of HCWA of electrodes with rutile coating

The contents of compounds of potassium and sodium affect greatly the gross precipitation and chemical composition of HCWA, as they are characterized, on one hand, by a high pressure of saturated steam and, on the other, they affect the rated arc voltage and, thus, the temperature conditions in the arc zone.

To determine the effect of content of compounds of alkali metals on sanitary-hygienic characteristics of electrodes with rutile coating, the series of investigations was carried out.

The compounds of alkali metals in the form of potassium titanate were added to the electrode coating of rutile electrodes (series E) by decrease of content of iron powder (Table 3). The content of components used in coating and not given in Table 3 was not changed. Besides, in electrode coatings of this series the silicates of sodium (E1) and potassium (E2–E5) were presented in the composition of dry remnant of liquid glass which is used as a binder. Using electrodes the welding was performed at alternating current from the transformer STSh-500. In the course of welding the specific precipitation of HCWA was determined, and samples were taken for determination of chemical composition of HCWA using the above-described procedure. The changed contents of components of coating are given in Table 3, welding conditions — in Table 4, chemical composition — in Table 5, specific precipitation — in Figure 2.

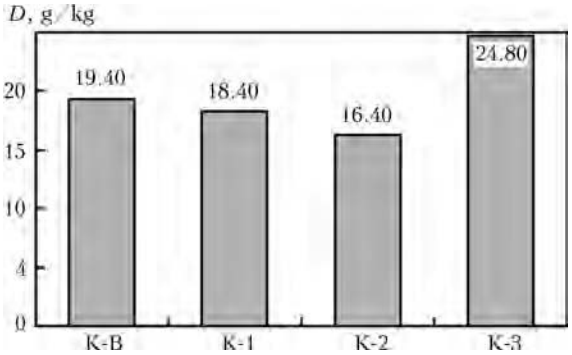

Figure 3. Specific precipitation of HCWA of electrodes with basic coating

Analysis of results of experiment shows that with growth of content of compounds of potassium in the electrode coating, the specific precipitation of HCWA is decreased that can be explained by the decrease in voltage (see Table 4) due to increase in number of ions of potassium in the arc column. This leads to the decrease in power of arc discharge and reduction of intensity of evaporation of molten particles of metal and slag. However, at high content of compounds of potassium (E5) the speed of evaporation is increased in spite of decrease in arc power which leads to the growth of specific precipitation of HCWA, i.e. the factor of growth of concentrations of compounds of potassium in the slag melt operates. The content of K_2O in HCWA is increased and content of toxic compounds of manganese is decreased (see Table 5).

In the second series of experiments (series K) the influence of content of compounds of potassium on sanitary-hygienic characteristics of electrodes with the basic coating was evaluated. As a source of potassium compound the potash (K_2CO_3) was used which was added to the coating in the amounts of 0, 2, 4 and 8 % (Table 6). The content of components, used in the coating and not given in the Table, was not change.

Table 6. Composition of components in coating of basic electrodes, wt.%

Coating components	K-B	K-1	K-2	K-3
Iron powder	30	28	26	22
Potash	–	2	4	8
Type of liquid glass	Na	Na	Na	Na

Table 7. Conditions of welding using coated electrodes of K series

Electrode index	U_w, V
K-B	26–27
K-1	25–26
K-2	24–25
K-3	23–24

Note. Welding current of 190–200 A.

Table 8. Chemical composition of HCWA compounds of electrodes with basic coating, wt.%

Electrode index	Mn	Si	K	Na	Ca	Al	Fe	F
K-B	4.1	1.9	5.2	14.0	15.0	0.33	16.9	23.2
K-1	3.6	1.5	12.0	12.7	11.6	0.35	18.1	18.1
K-2	3.3	1.4	13.8	11.8	10.7	0.27	17.9	18.3
K-3	2.6	1.2	19.6	9.4	9.6	0.20	17.1	20.3

The welding was carried out at direct current of reverse polarity from the rectifier VD-306. The conditions of welding are given in Table 7, the chemical composition of HCWA — in Table 8, specific precipitation of HCWA — in Figure 3.

The results, as in previous series for electrodes with rutile coating, show that increase in content of alkali metals in electrode coating leads firstly to decrease in precipitation of HCWA and at high content of potassium compounds — to the growth of HCWA precipitation. Such dependence is explained by the effect of two opposite acting factors: on the one hand, by decrease in arc power as a result of drop of voltage and, respectively, the decrease in temperature of melts of metal and slag that leads to the reduction in intensity of evaporation, and, on the other hand, by increase in content of compounds of alkali metals with high vapor pressure in slag that leads to the growth of evaporation intensity. At the certain stage (at high content of potassium compounds) the second factor is prevailed and leads to the growth of precipitation of HCWA (K-3).

It was found using X-ray fluorescent analysis of chemical composition of HCWA that with the growth of content of compounds of potassium in the electrode coating of the basic type the content of potassium in HCWA is increased, whereas content of manganese, silicon, sodium and calcium is decreased (Table 8).

The carried out investigations prove the possibility of improvement of sanitary-hygienic characteristics of electrodes due to regulation of composition of coating. The obtained results represent a practical interest and will be used in future development of universal electrodes with coating of a rutile type.

1. Pokhodnya, I.K. (2003) Welding consumables: State-of-the-art and tendencies of development. *The Paton Welding J.*, **3**, 2–13.
2. Makovetskaya, O.K. (2012) Main tendencies at the market of welding technologies in 2008–2011 and forecast of its development (Review). *Ibid.*, **6**, 32–38.
3. Voitkevich, V. (1995) *Welding fumes: formation, properties and biological effects*. Cambridge: Abington Publ.
4. Pokhodnya, I.K., Gorpenyuk, V.N., Milichenko, S.S. et al. (1990) *Metallurgy of arc welding. Processes in arc and melting of electrodes*. Ed. by I.K. Pokhodnya. Kiev: Naukova Dumka.
5. Pokhodnya, I.K., Marchenko, A.E., Bejnish, A.M. (1961) High efficient electrodes with iron powder in coating. *Avtomatich. Svarka*, **10**, 52–68.

MODERN WELDING MARKET OF THE NORTH AMERICA

O.K. MAKOVETSKAYA
E.O. Paton Electric Welding Institute, NASU, Kiev, Ukraine

In the article the statistical data characterizing the state-of-the-art and main trends in development of welding market in the North America are given.

Keywords: *welding equipment, welding consumables, main values, market, statistics*

The market of welding equipment of the North America is one of the largest regional markets in the world (30 % of the world welding market). According to the data of the American Bureau of Statistics, in the USA in 2011 the cost volume of the production of equipment (excluding transformers) and accessories for welding and brazing, such as equipment for arc, resistance, gas, plasma, laser, electron beam, ultrasonic welding; welding electrodes, welding wire (coated and with a core); equipment for brazing (except manual soldering irons) amounted to 4.9 bln USD (2009 — 3.6 bln USD, 2010 — 4.1 bln USD). The volume of import from 76 countries of the world amounted to 1.4 bln USD, and export — 1.8 bln USD (163 countries). Thus, the cost volume of consumption of equipment and materials for welding and brazing in the USA in 2011 amounted to 4.6 bln USD. It should be noted that in spite of 25 % annual growth of production the welding industry of the USA in 2011 did not reach the pre-crisis volume of production which amounted to 5.1 bln USD in 2008 [1].

In Figure 1 the structure of production of the main types of products for welding and brazing in the USA in 2011 is presented.

In the structure of US production 79 % account for the equipment and accessories for welding and brazing and 21 % — materials. The main share of production of welding equipment (about

© O.K. MAKOVETSKAYA, 2012

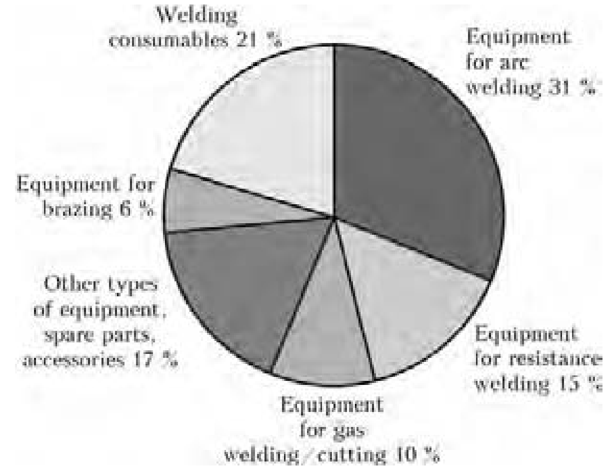

Figure 1. Cost structure of volumes of production of equipment and consumables for welding and brazing per 2011

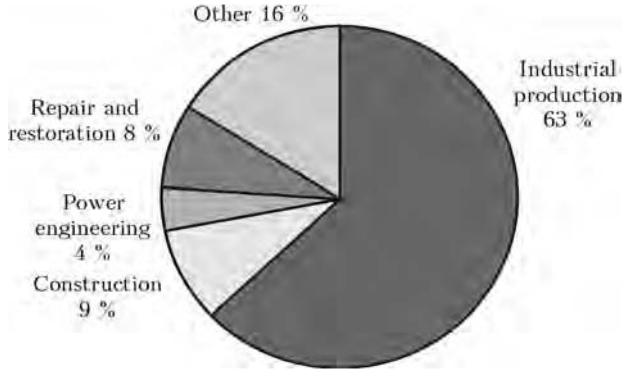

Figure 2. Branch structure of consumption of welding equipment in the USA per 2010

70 %) amounts for machines for arc and resistance welding.

In the structure of welding equipment consumption the equipment for arc and resistance welding also dominates, the share of which is about 70 % of all the volume of consumption.

The structure of consumption of welding consumables the share of welding and filler materials amounts for 73 %, the rest is oxygen and shielding gases. Among the gases used for welding and cutting the consumption of oxygen and acetylene is prevailed. As shielding gases the argon and carbon dioxide are most widely applied [2].

According to the data of «The Japan Welding News for the World», in 2011 the share of countries of the North America (USA and Canada) in the world volume of consumption of welding consumables amounted to 7.2 % (430,000 t): volume of consumption of coated electrodes is 60,200 t, solid wire — 232,200 t, flux-cored wire — 94,600 t, consumables for submerged arc welding — 43,000 t.

In the Table the structure of consumption of the main types of welding consumables in separate regions and countries of the world, including the North America, is given [3, 4].

In the structure of consumption of welding consumables of the countries of the North America the solid and flux-cored wires prevail, the share of which in 2011 amounted to 54 and 22 %, respectively.

The quantitative volume of consumption of equipment for arc and resistance welding in the North America countries in 2010 amounted to 115,000 pcs, among which 94 % are the equipment for arc welding and cost volume was 596 mln USD (78 % — the equipment for arc welding).

In the countries of the North America the level of automation of welding production is growing constantly. In 2011 in the world 43,440 units of welding robots were installed, among which 9000 units — in the North America, that amount 20.7 % of the whole number of welding robots installed in the world. According to the structure of consumption, the share of robots for resistance welding amounts 2/3 and for the arc welding — 1/3 of the whole number of installed welding robots [5].

The branch structure of US welding equipment consumption is presented in Figure 2.

Structure of consumption of basic types of welding consumables in some regions and countries of the world, %

Region/country	Coated electrodes		Solid wire		Flux-cored wire		Consumables for submerged arc welding (wire + flux) and other		In total, thousand tons	
	2008	2011	2008	2011	2008	2011	2008	2011	2008	2011
North America	15	14	58	54	21	22	6	10	520	430
China	60	51	25	29	4	8	11	12	2600	3000
Europe	13	12	64	54	11	19	12	13	680	570
Japan	12	10.4	47	42.8	30	35.3	11	11.5	364.8	285.6
Korea	14	13	37	35	39	40	10	12	260	230
Russia and CIS countries	58	51	27	29	4	6	11	14	240	220
World, in total	44.2	41.1	35.9	35.1	10.0	12.6	9.9	11.2	5784.8	5945.6

According to the estimates of the American Welding Society the growth of consumption of welding equipment in the USA in the nearest years is expected in agricultural machine building, road and bridge construction, railway and communication transport, power engineering, petrochemical industry (including construction of oil and gas pipelines, tankers for transportation of oil and gas).

It is predicted that in 2015 at annual growth by 6.4 % the cost volume of consumption of equipment and consumables for welding and brazing in the USA will reach 7.1 bln USD. In the branches of industry the volume of consumption of welding equipment will amount to 4.4 bln USD, and in construction — 750 mln USD [6].

According to the data of the US Bureau of Statistics about 970,000 of employers and specialists-welders are engaged in the national economy [7].

The basic manufacturers of welding equipment in the USA are:

- Lincoln Electric Holdings Inc. — the leading world manufacturer of equipment and consumables for welding and brazing. It includes the brands like Brastek, Harris. The company has 40 plants in 19 countries of the world and its distribution network comprises more than 160 countries. The volume of sales of the company in 2011 achieved 2.7 bln USD, which amounted to about 50 % of the total volume of sales at the market of the USA and 16 % at the world market of welding equipment. By the end of 2011 the company occupied the 1st place in the rating of the largest world manufacturers of welding equipment [8];
- Illinois Tool Works — the largest diversified company. It comprises the brands like ITW, Miller Electric, Hobart, Bernard, Weldcraft, Jetline, Elga, Tian TVai, WIA. The production capacities and distribution network are located in 57 countries of the world. The volume of sales in 2010 amounted to 15.9 bln USD, among which 12 % cover welding consumables and equipment. According to the data of [9] it occupied the 3rd place in the rating of the largest world manufacturers of welding equipment;
- Thermadyne Holdings — the leading manufacturer of gas-flame equipment in the USA. It comprises the brands like Thermadyne Industries, Thermadyne Dynamics, Victor, Tweco, Arcair, Thermal Arc, Stoody, Turbo Torch, Firepower and Cigweld. The production capacities and distribution network are located in the America, Europe and Asia. The volume of sales amounted to 487.4 mln USD in 2010. According to the data of [10] it occupied the 7th place in the rating of the largest world manufacturers of welding equipment.

1. Value of shipments for product classes: 2010 and earlier years. Annual Survey of Manufactures. U.S. Census Bureau. *http*://www.census.gov
2. Welding and soldering equipment manufacturing industry in the U.S. and its International Trade. Rep. *www*.Reportlinker.com
3. (2011) Worldwide demand for welding consumables. Worldwide demand for welding machines. *The Japan Welding News for the World*, 15(**55**), 5–6.
4. (2009) Worldwide demand for welding consumables. Worldwide demand for welding machines. *Ibid*., 13(**47**), 7.
5. (2012) General description for welding robots market. *Ibid*., 165(**56**), 6–7.
6. (2011) US demand for welding equipment & consumables to exceed $7 Billion (USD) in 2015. *Daily News*, November, 11.
7. Occupation employment statistics. 51-4121 Welders. cutters. solders and brazers. 51-4122. Welding. soldering and brazing machine setters. operators and tenders. U.S. Census Bureau. *http*://www.census.gov
8. Lincoln Electric Holdings. Inc. 4Q 2011. Financial results conference call. Febr. 17. 2012. *http*://www.lincolnelectric.com
9. ILLINOIS TOOL WORKS INC. 2011 Annual Report. *http*://www.itw.com
10. Thermadyne Holdings Corporation. Investor presentation. Aug. 2011. *http*://www.thermadyne.com

OPENING OF LASER CENTER IN KIROV, RF

Vyatka Laser Innovative-Technological Center (VLITC) was opened in Kirov in October 16, 2012 in scope of special international agreement on scientific-and-technical cooperation between Germany and Russia in the field of laser and optical technologies (2004). The main peculiarity of this Center is that the equipment and training of technical staff for its servicing were provided by German side, represented by TRUMPF and KUKA, to Russian side free of charge. In turn a special area for German equipment as well as necessary communications, energy carriers and servicing staff were given by the Russian side.

VLITC was opened on the basis of «Machine tool plant Termit» Ltd. Significant assistance in its creation was rendered by director of the plant A.A. Tyuftin. The point is that a laser area equipped with 1 kW power disc laser of TruDisk 1000 model from TRUMPF and two 3D portal type manipulators had been already present for some time on the territory of indicated enterprise. This area was created in 2011 and represented the first step of VLITC development in the scope of Russian-German uncommercial relationships. Signing of Intergovernmental Russian-Germany Agreement on modernization of production engineering in the RF in 2005 made a basis for creation of partnership. The German government on the basis of this Agreement realized the first delivery of laser equipment in Kirov. It was recently additionally equipped by more powerful industrial complex.

Thus, laser technological complex TruLaser Robot 5020 was added to the equipment of newly developed VLITC. The complex includes 4 kW power laser of TruDisk 4001 model from TRUMPF and anthropomorphous robot with six degrees of freedom from KUKA. Any welding, cutting or surfacing head up to 30 kg weight can be moved in the operating field of this complex, representing itself area of 1400 × 800 × 1200 mm (width × height × depth), with ±0.1 mm accuracy.

A series technological developments are in the plans of Dr. A.M. Chirkov, the director of VLITC, in particular:

- laser welding of high pressure fittings for internal combustion engines;
- laser welding of thin sheet (around 3 mm) aluminum alloys using no filler materials;
- welding of gears of vehicular transmission using successive tandem of two laser beams;
- manufacture of drawing punches by method of laser pulse seam welding, laser welding of threaded rod with ball from ShKh-15 steel for compressor of household refrigerator;
- laser welding of hydraulic tappet from 12KhN3A steel;
- laser welding of different type bellows assemblies;
- restoration of geometric dimensions of turbine blades that were under operation;
- repair of crossings of locomotives by laser surfacing method;
- laser-plasma hardening of cutting faces of teeth of cutoff cutters;
- laser deposition of protective polymer nanocomposite coatings over threads of pump-and-compressor tubing allowing approximately one time increase of their service life;

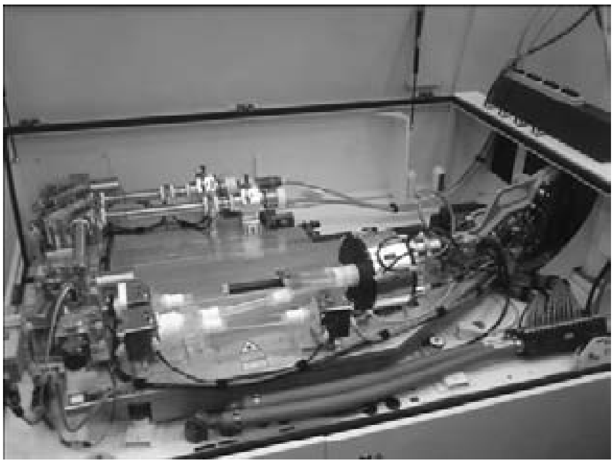

Structure of disk laser of TruDisk 4001 model

Internal view of area of safety camera of laser technology complex TruLaser 5020 equipped by the KUKA anthropomorphous robot-manipulator

Demonstration of possibilities of 3D portal manipulator, equipped by the TRUMPF optical head with irradiation scanning system

ВЛИТЦ
Некоммерческое партнерство
...ий лазерный инновационно- технологический центр»
LZH
TruLaser Robot 5020

Signing of Agreement about cooperation between VLITC and Vyatka State University (*at the table on the left* — A.M. Chirkov, Director of VLITC, *on the right* — V. Pugach, Rector of Vyatka State University)

TRUMPF
LASER
TruDisk 4

Disk laser of TruDisk 4001 model

- laser-plasma technology of carburization of steel surfaces;
- laser-plasma polishing under atmospheric conditions;
- laser-plasma refining of surfaces;
- laser-plasma cleaning of surfaces.

In present time several tens of technologies including such universal as laser welding of steel with high carbon equivalent, laser-plasma refining of steels under atmospheric conditions, laser-plasma polishing of surface, laser-plasma spraying were patented and worked through under the leadership and direct assistance of A.M. Chirkov. Contracts for repair of turbine blades of aircraft engines, turbine blades of gascompressor stations and rolls of mills by laser surfacing method are in development stage.

Representatives of TRUMPF and KUKA and C.D. Novitsky, Chief of department of business communication of development of Hanover International Laser Center, visited opening of VLITC from German side. The Russian side was presented by N. Belykh, Governor of Kirov region, F. Yusupov, Chief Federal Inspector, V. Bykov, Mayor of Kirov, V. Pugach, Rector of Vyatka State University and representatives of companies-manufacturers as well as laser innovation-and-technology centers from other regions of Russia. Bilateral agreement about cooperation and training of students was solemnly signed by VLITC director and rector of Vyatka State University.

Prof. V.Yu. Khaskin, PWI

INTERNATIONAL SPECIALISED EXHIBITION OF WELDING CONSUMABLES, EQUIPMENT AND TECHNOLOGIES «WELDEX/ROSSVARKA 2012»

The 12th International Specialised Exhibition WELDEX/ROSSVARKA 2012 took place in Moscow at the «Sokolniki» Culture and Exhibition Centre from 23 till 26 October 2012. Traditionally, this Exhibition serves as a site for bringing new welding technologies to the market, presentation of products, and a venue for meeting of manufacturers, suppliers and customers. The Exhibition opens up new prospects for business to its participants, allows the visitors to get acquainted with development trends in the metalworking industry, and helps to establish new business contacts.

About 250 participants presented at the Exhibition the advanced welding technologies, new consumables and equipment for welding, cutting, brazing, surfacing and deposition of protective coatings. Participating in the Exhibition were the companies — world leaders in the industry, such as Lincoln Electric (USA), ESAB (Sweden) and Messer Eutectic Castolin (Germany). Among the new participants in the Exhibition 2012 were such companies as Kjellberg Finsterwalde Plasma and Machines (Germany), Hyundai Welding (South Korea), Hoganas (Sweden), Redbo (China), the Ural Electrode Factory, Eurolux Group, VEKPROM Industrial Group, TERMOKAT, TD TOS (Russia), and many others.

Compared to the Exhibition 2011, geography of this year Exhibition expanded to present companies from 19 countries of the world — Austria, Belarus, Great Britain, Germany, Italy, Kazakhstan, China, Korea, Latvia, Poland, Portugal, Russia, USA, Turkey, Uzbekistan, Ukraine, France, Switzerland and Sweden.

The strong advertising campaign attracted a substantial quantity of visitors representing the most diverse enterprises from different industries of Russia, other CIS countries, as well as other countries of the world. It promoted the maximal disclosure of potential of the Exhibition, increase in attendance, and widening of the possibilities for establishing of cooperation.

The ceremony of opening of WELDEX/ROSSVARKA 2012 began with the welcoming addresses by M.E. Basheleishvili, Director General of the International Exhibition Company (IEC), V.I. Lavrukhin, Chairman of the Moscow Chamber of Industry and Commerce, Yu.K. Podkopaev, President of the Moscow Intersectoral Association of Chief Welders (MIACW), O.I. Steklov, President of the Russian Scientific and Technical Welding Society (RSTWS), and V.A. Frolov, representative of the Quality Department of ROSKOSMOS and Rector of the Russian State Technological Universitys-MATI.

The speakers noted that the welding technology enables forming the products that make up about 50 % of costs of the gross output in the developed countries. This adds a high importance to communication of specialists in this industrial segment. The Exhibition, undoubtedly, gives a powerful incentive to application of advanced technologies. Also, there is an evident trend to expansion of the range of countries participating in the Exhibition. Today, this event is regarded as number three in the world as to the scope of the participants, exposition floor area, and well-deserved authority.

The entire spectrum of the materials joining and cutting technologies was exhibited on a floor area of more than 9000 m^2 in pavilions 4 and 4.1 of the «Sokolniki» Culture and Exhibition Centre, where the leading manufacturers demonstrated their products. Exposition of Russian enterprises (168 booths) was the most repre-

ROBUR
www.robur.ru
Контактная сварка

sentative at the Exhibition. Among them were the known manufacturers of welding equipment, such as Avtogenmash, Ryazan State Instrument-Making Plant, Engineering and Technological Service, Iskra, PKTBA, Plazer, Plazmamash, Tehnotron, Tor, Uraltermosvar and Storm, as well as manufacturers of welding consumables, such as Welding Consumables Factory (Berezovsky, Sverdlovsk Region), Losinoostrovsky Electrode Factory, Metallurgical Works Elektrostal, Spetzelektrod, Sudoslavsky Factory of Welding Consumables, Urals Electrode Factory, and Cherepovetzk Factory of Welding Consumables.

The world-known brands of a number of the leading companies were represented by their branches in Russia — Weld DMS of Bohler Welding, Kemppi, EWM (Germany), Blue Weld (Italy), Translas (The Netherlands), Fubag (Germany), LLL Tena, and AOUT Representatives.

Ukraine at the Exhibition was represented by booths of the Kramatorsk Factory Donmet, Navkotekh, and the Pilot Plant for Welding Equipment and «Avtomaticheskaya Svarka» (Automatic welding) Journal of the E.O. Paton Electric Welding Institute.

It is noteworthy that the Exhibition included wide expositions of a number of the leading research, technological and engineering centres of Russia, such as the Welders Alliance of St.-Petersburg and North-West Region, NITI Progress, Prometey, Kontur-97, K.E. Tsyolkovsky Russian State Technological University-MATI, RSTWS, Portal Engineering, etc.

As usually, welding equipment for various methods of arc welding of metals accounted for the main volume of exhibits. The persisting trends were those to development of inverter circuits with microprocessor program synergic control providing such functions as hot start, antistick and arc force, substantial power saving, decrease in requirements to welders' skill with assurance of the proper welding quality, and insensitivity to mains voltage fluctuations (which is especially important for welding in building industry).

Transfer to the fully digital inverter pulse technology in equipment circuits provides reproducibility of the welding results with an almost absolute elimination of spatters of the molten metal.

In general, of the intense interest among the specialists visiting the Exhibition were the ex-

hibits corresponding to the state-of-the-art in welding engineering and in equipment for thermal cutting methods (gas, plasma, etc.).

Characteristic features of the majority of specialised exhibitions held in Moscow and St.-Petersburg are that most booths demonstrated activities and ranges of the goods and services offered by trading companies, such as Company Avan, AVG Technologies, Weber Comechanics, Alex (Moscow), TD Argus (Nizhny Novgorod), Dukon (St.-Petersburg), and many others.

It should be noted that Lincoln Electric demonstrated for the first time ever at the exhibitions in Russia the new development in the field of training of welders. The virtual welding simulator was demonstrated in real application all days long during the Exhibition. All those who wished could take part in the competition, test their skills and receive an objective mark.

The business program of the Exhibition included:

- Scientific and Practical Conference «Innovative Contribution to Upgrading of Welding Production at the Aerospace Complex of Russia» (three-hours Workshop, 23 October, organiser — RSTWS);
- Conference «Topicality and Spheres of Application of Thermal Spraying and Cladding Technology» (one-day workshop, 24 October, organiser — Plackart);
- Scientific and Practical Conference in the «Business Meeting Club» format at the field session of MIACW (24 October, MIACW);
- Seminar «Modern Advertisement and Public Relations Methods for Companies Involved in Welding Engineering (25 October, Right People);
- Competitions: «Virtual Welders» (23–26 October, organiser — Lincoln Electric), «Best Welder-2012» and «Best Welding Engineer-2012» (24 October, organisers — IEC, ELSVAR), «Miss Welding of Russia-2012» (25 October, IEC and ELSVAR).

Also arranged was the demonstration of artistic-decorative pieces made by the welding and forging methods, «Welding in Fine Art», which could be visited in all days of the Exhibition.

The Exhibition was attended by over 5 thousand people, including official persons, managers, chief welders and specialists of enterprises.

It is the opinion of many visitors that WELDEX/ROSSVARKA 2012 became a unique business platform for welding professionals, promoting successful realisation of commercial plans. During the days of working of the Exhibition many participants found purchasers and made contracts for future supplies. Visitors and specialists of the industry could establish many helpful contacts for development of their business and receive topical information on market trends for the next year.

In 2013, Exhibition WELDEX/ROSSVARKA will be held from 8 till 11 October at the «Sokolniki» Culture and Exhibition Centre.

Prof. V.N. Lipodaev, PWI

INDEX OF ARTICLES FOR TPWJ'2012, Nos. 1–12

50 Years at the Head of the National Academy of Sciences of Ukraine **2**

BRIEF INFORMATION

Effect of the shape of tungsten carbide particles on their microhardness, chemical heterogeneity and wear resistance of the composite deposited metal (Zhudra A.P.and Dzykovich V.I.) **2**

Influence of surfactants on phase formation during production of Al–Cu–Fe system powders for thermal coatings by the method of mechanochemical synthesis (Burlachenko A.N. and Borisov Yu.S.) **1**

Thesis for a scientific degree **1, 2, 5**

INDUSTRIAL

Agglomerated fluxes in local welding production (Review) (Golovko V.V.) **2**

Application of thermal barrier coatings for internal combustion engines (Review) (Tsymbalistaya T.V.) **6**

Application of welding technologies at realization of European program on new renewable energy sources (Klimpel A.) **3**

At the origins of integrated development of welding production **2**

Automated system for diagnostics and repair of reactor containment shell at Bilibinskaya NPP (Rosert R., Shutikov A.V., Fedosovsky M.E., Lukin E.I. and Karasev M.V.) **7**

«Binzel Ukraine GmbH» – 15 Years of Development: Interview with Yu.A. Didus, Director General **10**

Braze-welding with weld metal peening during its solidification (Pismenny A.S., Pentegov I.V., Kislitsyn V.M., Stemkovsky E.P. and Shejkovsky D.A.) **11**

Capacitor-discharge stud welding in vacuum (Paton B.E., Kaleko D.M., Bulatsev A.R. and Shulym V.F.) **4**

Cladding flux-cored strips (Review) (Zhudra A.P. and Voronchuk A.P.) **1**

Cold resistance and lamellar fracture resistance of welded joints on steel 06GB-390 (Poznyakov V.D., Barvinko A.Yu., Barvinko Yu.P., Sineok A.G. and Yashnik A.N.) **3**

Combined fusion welding technologies (Review) (Lashchenko G.I.) **8**

Comparative analysis of ISO 18841:2005 standard and RF 26389–84 standard on evaluation to hot crack resistance in welding (Yakushin B.F.) **11**

Computer system for calculation of norms of consumption of welding consumables for manufacture and repair of steel pipelines (Ivanov G.A. and Proncheva V.N.) **1**

Control of formation of welded joints in ESW (Review) (Protokovilov I.V. and Porokhonko V.B.) **10**

Corrosion-fatigue strength of 12Kh18N10T steel T-joints and methods of its improvement (Kolomijtsev E.V.) **12**

Developed at PWI **9**

Development of forge-welded combined medium-pressure rotor for 325 MW steam turbine (Tsaryuk A.K., Moravetsky S.I., Skulsky V.Yu., Grishin N.N., Vavilov A.V., Kantor A.G. and Grinchenko E.D.) **8**

Development of surface crack-like defect in welded joints of 06GB-390 steel at cyclic loading (Barvinko A.Yu., Knysh V.V., Barvinko Yu.P. and Yashnik A.N.) **5**

Development of technology of automatic submerged arc welding of armor steels **3**

Development of the technology of manufacturing double-wall welded transformable-shell structure (Lobanov L.M. and Volkov V.S.) **10**

Effect of flux composition on thermal-physical and physical-chemical processes in liquid-metal electroslag surfacing (Kuzmenko O.G.) **9**

Effectiveness of various variants of electrodynamic treatment of AMg6 alloy and its welded joints (Lobanov L.M., Pashchin N.A., Mikhoduj O.L., Cherkashin A.V., Manchenko A.N., Kondratenko I.P. and Zhiltsov A.V.) **12**

Electrode compression drive for resistance spot microwelding (Lankin Yu.N., Semikin V.F., Osechkov P.P. and Bajshtruk E.N.) **2**

Equipment and technology of EBW in finishing smoothing and repair of reverse beads of welds of tubular products (Kravchuk L.A.) **5**

Equipment for heat treatment of welded joints on pipelines (Pantelejmonov E.A.) **4**

Evaluation of quality of technological processes of surfacing of parts of railway rolling stock (Artemchuk V.V.) **7**

Experience in hardfacing of propeller shafts at the PJSC Kherson Shipyard (Goloborodko Zh.G.) **9**

Experience of application of plasma hardening unit UDGZ-200 at enterprises of the Urals region (Korotkov V.A.) **5**

Features of producing sound welds in electron beam welding of thick high-strength steels (Belenky V.Ya., Trushnikov D.N., Mladenov G.M. and Olshanskaya T.V.) **2**

Fields of application of magnetic-pulse welding (Review) (Poleshchuk M.A., Matveev I.V. and Bovkun V.A.) **4**

Improvement of method of plasma surfacing with side feeding of filler wire (Shapovalov K.P., Makarenko N.A. and Granovskaya L.A.) **2**

Improvement of the technology for submerged-arc welding of copper to steel (Koleda V.N.) **3**

Increase of strength characteristics of spirally-welded pipes of structural designation (Pismenny A.S., Prokofiev A.S., Gubatyuk R.S., Pismenny A.A., Polukhin V.V., Yukhimenko R.V. and Gavrik A.R.) **3**

Influence of content of iron powder and compounds of alkali metals in the composition of electrode coating on their sanitary-hygienic characteristics (Pokhodnya I.K., Yavdoshchin I.R. and Gubenya I.P.) **12**

Influence of violations of welding gun axial symmetry on focal spot position (Nazarenko O.K. and Matvejchuk V.A.) **7**

Interview with V.G. Subbotin, Director General of OJSC TURBOATOM **8**

Light-weight welding tractors of the E.O. Paton Electric Welding Institute **5**

Main tendencies at the market of welding technologies in 2008–2011 and forecast of its development (Review) (Makovetskaya O.K.) **6**

Method for manufacture of large-sized forged-cast billets using electroslag welding (Voloshin A.I., Shapovalov K.P., Belinsky V.A., Litvinenko S.N., Yushchenko K.A., Lychko I.I. and Kozulin S.M.) **5**

Modern methods of surfacing the tools of agricultural tillers and harvesters (Review) (Senchishin V.S. and Pulka Ch.V.) **9**

Modern methods of welding aluminium alloys to steels (Review) (Kaleko D.M.) **10**

Modern welding market of the North America (Makovetskaya O.K.) **12**

Multichannel microprocessor controller for data collection from thermocouples (Dolinenko V.V., Skuba T.G., Vashchenko O.Yu. and Lutsenko N.F.) **11**

New technology of electric arc bath welding of rails on tram and crane tracks (Kuzmenko G.V., Kuzmenko V.G., Galinich V.I. and Taganovsky V.M.) **5**

New type of pulse stabilizer of alternating current welding arc (Zaruba I.I., Andreev V.V., Shatan A.F., Moskovich G.N. and Khalikov V.A.) **2**

Peculiarities of laser-arc welding of titanium alloys (Shelyagin V.D., Khaskin V.Yu., Akhonin S.V., Belous V.Yu., Petrichenko I.K., Siora A.V., Palagesha A.N. and Selin R.V.) **12**

Peculiarities of wear and criteria of repairability of drill bits with diamond–hard-alloy cutters (Khorunov V.F., Stefaniv B.E., Sabadash O.M. and Voronov V.V.) **10**

Portable apparatus for consumable-nozzle electroslag welding (Yushchenko K.A., Lychko I.I., Kozulin S.M., Fomakin A.A., Dakal V.A. and Oganisyan E.S.) **8**

Procedure for calculation of dimensions of nozzles in welding using two separate gas jets (Belokon V.M. and Koroteev A.O.) **11**

PWI contribution to post-war revival of industry **6**

Repair explosion cladding of threaded channel of car axles (Lobanov L.M., Illarionov S.Yu., Dobrushin L.D., Pashchin N.A., Tisenkov V.V., Bondarev S.V., Gavrilov S.A., Sergienko N.A. and Kutishenko A.V.) **2**

Repair welding of intermediate cases of aircraft engines from high-temperature magnesium alloy ML10 with application of electrodynamic treatment (Lobanov L.M., Pashchin N.A., Cherkashin A.V., Tkachuk G.I., Savitsky V.V., Mikhoduj O.L., Shiyan K.V., Levchuk V.K., Zhyginas V.V. and Lyashchenko A.P.) **11**

Spatial distribution of magnetic field and its minimization in resistance spot welding (Levchenko O.G., Levchuk V.K. and Goncharova O.N.) **8**

Technological innovations — basis for increase of competitiveness of the U.S. welding production (Makovetskaya O.K.) **11**

Technology and new generation of equipment for flash butt welding of advanced high-strength rails for construction and reconstruction of high-speed railway lines (Kuchuk-Yatsenko S.I., Krivenko V.G., Didkovsky A.V., Shvets Yu.V., Kharchenko A.K. and Levchuk A.N.) **6**

Technology of projection welding of parts of large thicknesses with T-shaped joints (Kuchuk-Yatsenko V.S., Nakonechny A.A., Gavrish V.S. and Chernobaj S.V.) **8**

Technology of repair welding of boiler unit assemblies without postweld heat treatment (Tsaryuk A.K., Ivanenko V.D., Skulsky V.Yu., Moravetsky S.I., Gavrik A.R., Strizhius G.N., Nimko M.A., Mazur S.I., Trojnyak A.A., Odin Yu.V., Derkach O.V. and Kura R.I.) **9**

Tendencies in development of control of metal transfer processes in shielding gases (Review) (Zhernosekov A.M.) **1**

Theory and technology of submerged-arc welding **4**

Thermal spraying of coatings using tips (Murashov A.P.) **10**

Thermal spraying of pseudo-alloy coatings (Review) (Vigilyanskaya N.V., Borisov Yu.S. and Demianov I.A.) **1**

Three-phase inverter power source with direct conversion and increased power factor (Burlaka V.V. and Gulakov S.V.) **7**

INFORMATION

Presentation of technology of arc welding of position butts of pipes of main pipelines **5**

NEWS

Developed at PWI **6, 7, 9**

11th International Conference-Exhibition on Problems of Corrosion and Anticorrosive Protection of Structural Materials «Corrosion-2012» **8**

Experience of application of HF electric welding apparatus EK-300M1 in surgery (Ivanova O.N., Zelnichenko A.T., Kunkin D.D., Perekrest V.V. and Todorenko V.A.) **11**

International Conference «Ti-2012 in CIS» **6**

International Scientific-and-Technical Conference «Surface Engineering and Renovation of Parts» **8**

International Seminar «Materials Science in EU Projects» **10**

International Specialised Exhibition of Welding Consumables, Equipment and Technologies «Weldex/Rossvarka 2012» **12**

News **5, 6**

Opening of Laser Center in Kirov, RF **12**

Our congratulations! **5**

Scientific-Technical Conference «Modern Problems of Metallurgy Technology of Welding and Surfacing of Steels and Non-Ferrous Metals» **11**

Session of Scientific Council on New Materials at Committee on Natural Sciences of International Association of Academies of Sciences **7**

6 Years Anniversary of Russian-German Regional Laser Centres **10**

SCIENTIFIC AND TECHNICAL

Application of powders of cobalt and nickel alloys for plasma surfacing of exhaust valves of internal combustion engines (Pereplyotchikov E.F.) **7**

Application of titanium alloys with submicrocrystalline structure for reconditioning of GTE rotor parts (Ovchinnikov A.V.) **2**

Assessment of hydrogen influence on delayed fracture of welded joints from high-strength low-alloyed steels (Kharbin N.N., Sleptsov O.I., Sivtsev M.N. and Vinokurov G.G.) **6**

Brazing of titanium alloys by using aluminium-base filler alloys (Khorunov V.F., Voronov V.V. and Maksymova S.V.) **11**

Calculation of local stresses in welded joint zones of large-sized space structures (Kyrian V.I., Dvoretsky V.I. and Malgin M.G.) **4**

Chromium-manganese consumables for welding of higher-strength steels without preheating and heat treatment (Kulik V.M., Demchenko E.L., Vasiliev D.V. and Elagin V.P.) **10**

Combined diffusion process of joining bimetal elements of heat exchange system (Khokhlova Yu.A., Fedorchuk V.E. and Khokhlov M.A.) **1**

Combined laser-microplasma cladding with powders of Ni–Cr–B–Si system alloys (Borisov Yu.S., Khaskin V.Yu., Vojnarovich S.G., Kislitsa A.N., Tunik A.Yu., Adeeva L.I., Kuzmich-Yanchuk E.K., Bernatsky A.V. and Siora A.V.) **11**

Consideration of pore formation at estimation of limiting state in zone of pressure vessel wall thinning defect (Makhnenko V.I., Velikoivanenko E.A., Rozynka G.F. and Pivtorak N.I.) **12**

Department for investigations of physical-chemical processes in the welding arc is 50 years (Pokhodnya I.K.) **6**

Dislocation model of hydrogen-enhanced localizing of plasticity in metals with bcc lattice (Ignatenko A.V., Pokhodnya I.K., Paltsevich A.P. and Sinyuk V.S.) **3**

Effect of additions of aluminium to flux-cored wire on properties of high-carbon deposited metal (Krivchikov S.Yu.) **5**

Effect of heat treatment on sensitivity of the HAZ metal on titanium-stabilised austenitic steel to local fracture (Poletaev Yu.V.) **7**

Effect of high-temperature thermal cycling on deposited metal of the type of heat-resistant die steels (Ryabtsev I.A., Kondratiev I.A., Babinets A.A., Gordan G.N., Kajda T.V. and Bogajchuk I.L.) **2**

Effect of palladium on structure and technological properties of Ag–Cu–Zn–Ni–Mn system brazing filler alloys (Khorunov V.F., Maksymova S.V. and Stefaniv B.V.) **9**

Effect of structural-phase transformations in aluminium-lithium alloy 1460 joints on physical-mechanical properties (Markashova L.I., Ishchenko A.Ya., Kushnaryova O.S. and Fedorchuk V.E.) **5**

Efficiency of electrodynamic treatment of aluminium alloy AMg6 and its welded joints (Lobanov L.M., Pashchin N.A., Cherkashin A.V., Mikhoduj O.L. and Kondratenko I.P.) **1**

Efficiency of electrodynamic treatment of welded joints of AMg6 alloy of different thickness (Lobanov L.M., Pashchin N.A. and Mikhoduj O.L.) **3**

Efficiency of the use of protective extension in plasma spraying (Murashov A.P., Grishchenko A.P., Vigilyanskaya N.V., Burlachenko A.N. and Demianov I.A.) **2**

Electron beam welding of thick-wall shells of aluminium AMg6 and M40 alloys (Ternovoj E.G. and Bondarev A.A.) **4**

Experimental review of the welding metallurgy of high-strength aluminium alloy 7025-T6 (Olabode M., Kah P. and Martikainen J.) **4**

Experimental study and modelling of thermal-deformation processes occurring in welded joints on nickel superalloys (Yushchenko K.A., Romanova V.A., Balokhonov R.R., Savchenko V.S., Chervyakov N.O. and Zvyagintseva A.V.) **10**

Experimental study of the mechanism of hydrogen embrittlement of metals with the bcc lattice (Sinyuk V.S., Pokhodnya I.K., Paltsevich A.P. and Ignatenko A.V.) **5**

Flash-butt welding of thick-walled pipes from high-strength steels of K56 strength class (Kuchuk-Yatsenko S.I., Shvets Yu.V., Zagadarchuk V.F., Shvets V.I., Khomenko V.I., Zhuravlyov S.I., Sudarkin A.Ya., Kolikov V.L. and Khomichenko S.A.) **5**

Formation of spinel in melt of the $MgO{-}Al_2O_3{-}SiO_2{-}CaF_2$ system agglomerated welding flux and its effect on viscosity of slag (Goncharov I.A., Sokolsky V.E., Davidenko A.O., Galinich V.I. and Mishchenko D.D.) **12**

Formation of structure and properties of 316 type steel at successive circumferential electroslag surfacing with liquid metal (Polishko A.A., Medovar L.B., Saenko V.Ya., Stepanyuk S.I., Tunik A.Yu., Klochkov I.N. and Berezin I.V.) **2**

Friction welding of PIM heat-resistant steel to steel 40Kh (Zyakhor I.V. and Kuchuk-Yatsenko S.I.) **9**

Growth of corrosion cracks in structural steel 10GN2MFA (Makhnenko V.I., Markashova L.I., Makhnenko O.V., Berdnikova E.N., Shekera V.M. and Zubchenko A.S.) **8**

Heat-protecting properties of thermal spray coatings containing quasi-crystalline alloy of the Al–Cu–Fe system (Borisova A.L., Borisov Yu.S., Astakhov E.A., Murashov A.P., Burlachenko A.N. and Tsymbalistaya T.V.) **4**

Improvement of fatigue resistance of welded joints with accumulated damage under multistage and block loading (Knysh V.V., Solovej S.A. and Kuzmenko A.Z.) **7**

Improvement of reliability of main gas pipelines by using repeated in-pipe flaw detection (Varlamov D.P., Dedeshko V.N., Kanajkin V.A. and Steklov O.I.) **3**

Increasing wear resistance of titanium by argon arc overlaying (Prilutsky V.P., Rukhansky S.B., Akhonin S.V., Gadzyra N.F. and Davidchuk N.K.) **1**

Influence of austenitizing mode on local fracture susceptibility of welded joints of 03Kh16N9M2 steel (Poletaev Yu.V.) **3**

Influence of deposited metal composition on structure and mechanical properties of reconditioned railway wheels (Gajvoronsky A.A., Poznyakov V.D., Markashova L.I., Berdnikova E.N., Klapatyuk A.V., Alekseenko T.A. and Shishkevich A.S.) **8**

Influence of vibration of parts on structure and properties of metal in surfacing (Pulka Ch.V., Shably O.N., Senchishin V.S., Sharyk M.V. and Gordan G.N.) **1**

Influence of welding thermal cycle on structure and properties of microalloyed structural steels (Kostin V.A., Grigorenko G.M., Poznyakov V.D., Zhdanov S.L., Solomijchuk T.G., Zuber T.A. and Maksimenko A.A.) **12**

Inter-influence of defects in welded joint zone at different force loading (Makhnenko V.I., Velikoivanenko E.A., Milenin A.S., Rozynka G.F. and Pivtorak N.I.) **7**

Investigation of factors influencing the formation of weld defects in non-vacuum electron beam welding (Reisgen U., Schleser M., Abdurakhmanov A., Turichin G., Valdaitseva E., Bach F.-W., Hassel T. and Beniyash A.) **2**

Investigations on laser beam welding of high-manganese austenitic and austenitic-ferritic stainless steels (Quiroz V., Gumenyuk A. and Rethmeier M.) **1**

Laser welding of sheet stainless steel by modulated radiation (Lukashenko A.G., Melnichenko T.V. and Lukashenko D.A.) **4**

Manufacture of stainless steel–aluminum transition pieces by vacuum pressure welding method (Kharchenko G.K., Falchenko Yu.V., Fedorchuk V.E., Grigorenko S.G. and Rudenko M.M.) **1**

Mathematical formulation of carbon equivalent as a criterion for evaluation of steel weldability (Kostin V.A.) **8**

Mechanism of electromagnetic degassing of liquid metal in underwater welding (Gorobets O.Yu., Maksimov S.Yu. and Prilipko E.A.) **6**

Microstructural features of fatigue damageability and methods to improve the fatigue life of welded joints from 09G2S steel (Poznyakov V.D., Dovzhenko V.A., Kasatkin S.B. and Maksimenko A.A.) **5**

Modelling of processes of heat-, mass- and electric transfer in column and anode region of arc with refractory cathode (Krikent I.V., Krivtsun I.V. and Demchenko V.F.) **3**

Modification by boron of deposited metal of white cast iron type (Krivchikov S.Yu.) **6**

New capabilities of mechanized arc spot welding using pulse effects (Lobanov L.M., Lebedev V.A., Maksimov S.Yu., Timoshenko A.N., Goncharov P.V., Lendel I.V. and Klochko R.I.) **5**

New system of filler metals for brazing of titanium alloys (Khorunov V.F. and Voronov V.V.) **8**

Peculiarities of structure and mechanical heterogeneity in EB-welded joints of 1201-T alloy (Skalsky V.R., Botvina L.R. and Lyasota I.N.) **7**

Problems of stirring and melting in explosion welding (aluminium–tantalum) (Grinberg B.A., Elkina O.A., Patselov A.M., Inozemtsev A.V., Plotnikov A.V., Volkova A.Yu., Ivanov M.A., Rybin V.V. and Besshaposhnikov Yu.B.) **9**

Residual stresses in circumferential butt joints in the main gas pipeline at long-term service in the North (Golikov N.I. and Dmitriev V.V.) **12**

Risk of failure in thinning of main pipeline wall at the area of circumferential welds in the presence of bending moments along the pipeline axis (Makhnenko V.I., Velikoivanenko E.A., Rozynka G.F., Pivtorak N.I. and Olejnik O.I.) **1**

Structure and properties of welded joints of steel S390 (S355 J2) (Poznyakov V.D., Zhdanov S.L. and Maksimenko A.A.) **8**

Structure and properties of welded joints on titanium alloys containing silicon additions (Markashova L.I., Akhonin S.V., Grigorenko G.M., Kruglenko M.G., Kushnaryova A.S. and Petrichenko I.K.) **11**

Structure and wear resistance of chrome-manganese deposited metal (Malinov V.L. and Malinov L.S.) **7**

Substantiation of «leak-before-break» criterion for vertical cylindrical tanks for oil storage (Knysh V.V., Barvinko A.Yu., Barvinko Yu.P. and Yashnik A.N.) **9**

Technological peculiarities of laser welding of medium-carbon alloyed steel (Kulik V.M., Shelyagin V.D., Savitsky M.M., Elagin V.P., Siora A.V. and Shuba I.V.) **6**

Thermodynamic analysis of slag melts in manufacture of fused welding fluxes (Zhdanov L.A., Duchenko A.N., Goncharov I.A., Galinich V.I., Zalevsky A.V. and Osipov N.Ya.) **11**

To the mechanism of diffusion of chromium and molybdenum in the metal of welded joints of steam pipelines (Dmitrik V.V. and Syrenko T.A.) **10**

Transistor power sources for electric arc welding (Review) (Lebedev A.V.) **9**

Vacuum diffusion welding of γ-TiAl intermetallic alloy to 12Kh18N10T steel (Kharchenko G.K., Ustinov A.I., Falchenko Yu.V., Petrushinets L.V., Grigorenko S.G., Kostin V.A. and Gurienko V.P.) **4**

Welded structures from austenitic steel of 10Kh18N10T type under conditions of radiation-induced swelling (Makhnenko V.I., Makhnenko O.V., Kozlitina S.S. and Dzyubak L.I.) **2**

Welding from one side of clad piping of nuclear power plants (Kasatkin O.G., Tsaryuk A.K., Skulsky V.Yu., Gavrik A.R., Moravetsky S.I., Nimko M.A., Strizhius G.N., Terovets N.V., Byvalkevich A.I., Nemlej N.V. and Kuran R.I.) **10**

Index of articles for TPWJ'2012, Nos. 1–12 **12**

List of authors **12**

LIST OF AUTHORS

Abdurakhmanov A. No.2
Adeeva L.I. No.11
Akhonin S.V. No.1, 11, 12
Alekseenko T.A. No.8
Andreev V.V. No.2
Artemchuk V.V. No.7
Astakhov E.A. No.4

Babinets A.A. No.2
Bach F.-W. No.2
Bajshtruk E.N. No.2
Balokhonov R.R. No.10
Barvinko A.Yu. No.3, 5, 9
Barvinko Yu.P. No.3, 5, 9
Belenky V.Ya. No.2
Belinsky V.A. No.5
Belokon V.M. No.11
Belous V.Yu. No.12
Beniyash A. No.2
Berdnikova E.N. No.8(2)
Berezin I.V. No.2
Bernatsky A.V. No.10, 11
Besshaposhnikov Yu.B. No.9
Bogajchuk I.L. No.2
Bondarev A.A. No.4
Bondarev S.V. No.2
Borisov Yu.S. No.1(1), 4, 11
Borisova A.L. No.4
Botvina L.R. No.7
Bovkun V.A. No.4
Bulatsev A.R. No.4
Burlachenko A.N. No.1, 2, 4
Burlaka V.V. No.7
Byvalkevich A.I. No.10

Cherkashin A.V. No.1, 11, 12
Chernobaj S.V. No.8
Chervyakov N.O. No.10

Dakal V.A. No.8
Davidchuk N.K. No.1
Davidenko A.O. No.12
Dedeshko V.N. No.3
Demchenko E.L. No.10
Demchenko V.F. No.3
Demianov I.A. No.1, 2
Derkach O.V. No.9
Didkovsky A.V. No.6
Dmitriev V.V. No.12
Dmitrik V.V. No.10
Dobrushin L.D. No.2
Dolinenko V.V. No.11
Dovzhenko V.A. No.5
Duchenko A.N. No.11
Dvoretsky V.I. No.4
Dzykovich V.I. No.2
Dzyubak L.I. No.2

Elagin V.P. No.6, 10
Elkina O.A. No.9

Falchenko Yu.V. No.1, 4
Fedorchuk V.E. No.1(1), 5, 7
Fedosovsky M.E. No.7
Fomakin A.A. No.8

Gadzyra N.F. No.1
Gajvoronsky A.A. No.8
Galinich V.I. No.5, 11, 12
Gavrik A.R. No.3, 9, 10
Gavrilov S.A. No.2
Gavrish V.S. No.8
Golikov N.I. No.12
Goloborodko Zh.G. No.9
Golovko V.V. No.2
Goncharov I.A. No.11, 12
Goncharov P.V. No.5
Goncharova O.N. No.8
Gordan G.N. No.1, 2
Gorobets O.Yu. No.6
Granovskaya L.A. No.2
Grigorenko G.M. No.11, 12
Grigorenko S.G. No.1, 4
Grinberg B.A. No.9
Grinchenko E.D. No.8
Grishchenko A.P. No.2
Grishin N.N. No.8
Gubatyuk R.S. No.3
Gubenya I.P. No.12
Gulakov S.V. No.7
Gumenyuk A. No.1
Gurienko V.P. No.4

Hassel T. No.2

Ignatenko A.V. No.3, 5
Illarionov S.Yu. No.2
Inozemtsev A.V. No.9
Ishchenko A.Ya. No.5
Ivanenko V.D. No.9
Ivanov G.A. No.1
Ivanov M.A. No.9
Ivanova O.N. No.11

Kah P. No.4
Kajda T.V. No.2
Kaleko D.M. No.4, 10
Kanajkin V.A. No.3
Kantor A.G. No.8
Karasev M.V. No.5, 7
Kasatkin O.G. No.10
Kasatkin S.B. No.5
Khalikov V.A. No.2
Kharbin N.N. No.6
Kharchenko A.K. No.6
Kharchenko G.K. No.1, 4
Khaskin V.Yu. No.11, 12(2)

Khokhlov M.A. No.1
Khokhlova Yu.A. No.1
Khomenko V.I. No.5
Khomichenko S.A. No.5
Khorunov V.F. No.8, 9, 10, 11
Kislitsa A.N. No.11
Kislitsyn V.M. No.11
Klapatyuk A.V. No.8
Klimenko S.A. No.8
Klimpel A. No.3
Klochko R.I. No.5
Klochkov I.N. No.2
Knysh V.V. No.5, 7, 9
Koleda V.N. No.3
Kolikov V.L. No.5
Kolomijtsev E.V. No.12
Kondratenko I.P. No.1, 12
Kondratiev I.A. No.2
Kopejkina M.Yu. No.8
Kornienko A.N. No.2–6
Koroteev A.O. No.11
Korotkov V.A. No.5
Kostin V.A. No.4, 8, 12
Kozlitina S.S. No.2
Kozulin S.M. No.5, 8
Kravchuk L.A. No.5
Krikent I.V. No.3
Krivchikov S.Yu. No.5, 6
Krivenko V.G. No.6
Krivtsun I.V. No.3
Kruglenko M.G. No.11
Kuchuk-Yatsenko S.I. No.5, 6, 9
Kuchuk-Yatsenko V.S. No.8
Kulik V.M. No.6, 10
Kunkin D.D. No.11
Kura R.I. No.9
Kuran R.I. No.10
Kushnaryova A.S. No.11
Kushnaryova O.S. No.5
Kutishenko A.V. No.2
Kuzmenko A.Z. No.7
Kuzmenko G.V. No.5
Kuzmenko O.G. No.9
Kuzmenko V.G. No.5
Kuzmich-Yanchuk E.K. No.11
Kyrian V.I. No.4

Lankin Yu.N. No.2
Lashchenko G.I. No.8
Lebedev A.V. No.9
Lebedev V.A. No.5
Lendel I.V. No.5
Levchenko O.G. No.8
Levchuk A.N. No.6
Levchuk V.K. No.8, 11
Lipodaev V.N. No.12
Litvinenko S.N. No.5
Lobanov L.M. No.1, 2, 3, 5, 10, 11, 12
Lukashenko A.G. No.4
Lukashenko D.A. No.4
Lukin E.I. No.7
Lutsenko N.F. No.11
Lyashchenko A.P. No.11
Lyasota I.N. No.7
Lychko I.I. No.5, 8

Makarenko N.A. No.2
Makhnenko O.V. No.2, 8
Makhnenko V.I. No.1, 2, 7, 8, 12
Makovetskaya O.K. No.6, 11, 12
Maksimenko A.A. No.5, 8, 12
Maksimov S.Yu. No.5, 6
Maksymova S.V. No.9, 11
Malgin M.G. No.4
Malinov L.S. No.7
Malinov V.L. No.7
Manchenko A.N. No.12
Markashova L.I. No.5, 8(2), 11
Martikainen J. No.4
Matveev I.V. No.4
Matvejchuk V.A. No.7
Mazur S.I. No.9
Medovar L.B. No.2
Melnichenko T.V. No.4
Mikhoduj O.L. No.1, 3, 11, 12
Mikitenko A.M. No.5
Milenin A.S. No.7
Mishchenko D.D. No.12
Mladenov G.M. No.2
Moravetsky S.I. No.8, 9, 10
Moskovich G.N. No.2
Murashov A.P. No.2, 4, 10

Nakonechny A.A. No.8
Nazarenko O.K. No.7
Nemlej N.V. No.10
Nimko M.A. No.9, 10
Nurkova L.I. No.8

Odin Yu.V. No.9
Oganisyan E.S. No.8
Olabode M. No.4
Olejnik O.I. No.1
Olshanskaya T.V. No.2
Osadchuk S.A. No.8
Osechkov P.P. No.2
Osipov N.Ya. No.11
Ovchinnikov A.V. No.2

Palagesha A.N. No.12
Paltsevich A.P. No.3, 5
Pantelejmonov E.A. No.4
Pashchin N.A. No.1, 2, 3, 11, 12
Paton B.E. No.4
Patselov A.M. No.9
Pentegov I.V. No.11
Perekrest V.V. No.11
Pereplyotchikov E.F. No.7
Petrichenko I.K. No.11, 12
Petrushinets L.V. No.4
Pismenny A.A. No.3
Pismenny A.S. No.3, 11
Pivtorak N.I. No.1, 7, 12
Plotnikov A.V. No.9
Pokhodnya I.K. No.2, 3, 5, 6, 12
Poleshchuk M.A. No.4
Poletaev Yu.V. No.3, 7

Polishko A.A. No.2
Polukhin V.V. No.3
Porokhonko V.B. No.10
Poznyakov V.D. No.3, 5, 8(2), 12
Prilipko E.A. No.6
Prilutsky V.P. No.1
Prokofiev A.S. No.3
Proncheva V.N. No.1
Protokovilov I.V. No.10
Protsenko N.A. No.5
Protsenko P.P. No.5
Pulka Ch.V. No.1, 9

Quiroz V. No.1

Reisgen U. No.2
Rethmeier M. No.1
Romanova V.A. No.10
Rosert R. No.7
Rozynka G.F. No.1, 7, 12
Rudenko M.M. No.1
Rukhansky S.B. No.1
Ryabtsev I.A. No.2, 7, 11
Rybin V.V. No.9

Sabadash O.M. No.10
Saenko V.Ya. No.2
Savchenko V.S. No.10
Savitsky M.M. No.6
Savitsky V.V. No.11
Schleser M. No.2
Selin R.V. No.12
Semikin V.F. No.2
Senchishin V.S. No.1, 9
Sergienko N.A. No.2
Shably O.N. No.1
Shapovalov K.P. No.2, 5
Sharyk M.V. No.1
Shatan A.F. No.2
Shejkovsky D.A. No.11
Shekera V.M. No.8
Shelyagin V.D. No.6, 12
Shishkevich A.S. No.8
Shiyan K.V. No.11
Shuba I.V. No.6
Shulym V.F. No.4
Shutikov A.V. No.7
Shvets V.I. No.5
Shvets Yu.V. No.5, 6
Sineok A.G. No.3
Sinyuk V.S. No.3, 5
Siora A.V. No.6, 11, 12
Sivtsev M.N. No.6
Skalsky V.R. No.7
Skuba T.G. No.11
Skulsky V.Yu. No.8, 9, 10
Sleptsov O.I. No.6
Sokolsky V.E. No.12
Solomijchuk T.G. No.12
Solovej S.A. No.7
Stefaniv B.E. No.10
Stefaniv B.V. No.9
Steklov O.I. No.3
Stemkovsky E.P. No.11
Stepanyuk S.I. No.2
Strizhius G.N. No.9, 10
Sudarkin A.Ya. No.5
Syrenko T.A. No.10

Taganovsky V.M. No.5
Ternovoj E.G. No.4
Terovets N.V. No.10
Timoshenko A.N. No.5
Tisenkov V.V. No.2
Tkachuk G.I. No.11
Todorenko V.A. No.11
Trojnyak A.A. No.9
Trushnikov D.N. No.2
Tsaryuk A.K. No.8, 9, 10
Tsymbalistaya T.V. No.4, 6
Tunik A.Yu. No.2, 11
Turichin G. No.2

Ustinov A.I. No.4

Valdaitseva E. No.2
Varlamov D.P. No.3
Vashchenko O.Yu. No.11
Vasiliev D.V. No.10
Vavilov A.V. No.8
Velikoivanenko E.A. No.1, 7, 12
Vigilyanskaya N.V. No.1, 2
Vinokurov G.G. No.6
Vojnarovich S.G. No.11
Volkov V.S. No.10
Volkova A.Yu. No.9
Voloshin A.I. No.5
Voronchuk A.P. No.1
Voronov V.V. No.8, 10, 11

Yakushin B.F. No.11
Yashnik A.N. No.3, 5, 9
Yavdoshchin I.R. No.12
Yukhimenko R.V. No.3
Yushchenko K.A. No.5, 8, 10

Zagadarchuk V.F. No.5
Zalevsky A.V. No.11
Zaruba I.I. No.2
Zelnichenko A.T. No.11
Zhdanov L.A. No.11
Zhdanov S.L. No.8, 12
Zhernosekov A.M. No.1
Zhiltsov A.V. No.12
Zhudra A.P. No.1, 2
Zhuravlyov S.I. No.5
Zhyginas V.V. No.11
Zubchenko A.S. No.8
Zuber T.A. No.12
Zvyagintseva A.V. No.1
Zyakhor I.V. No.9, 10

SUBSCRIPTION
FOR «THE PATON WELDING JOURNAL»

If You are interested in making subscription directly via Editorial Board, fill, please, the coupon and send application by fax or e-mail.

The cost of annual subscription via Editorial Board is $324.

Telephones and faxes of Editorial Board of «The Paton Welding Journal»:
Tel.: (38044) 200 82 77, 200 81 45
Fax: (38044) 200 82 77, 200 81 45.

«The Paton Welding Journal» can be also subscribed worldwide from catalogues of subscription agency EBSO.

SUBSCRIPTION COUPON
Address for journal delivery ______________________________
____
Term of subscription since ________ 20 ____ till ________ 20 ____
Name, initials ______________________________
Affiliation ______________________________
Position ______________________________
Tel., Fax, E-mail

Subscription to the electronic version of «The Paton Welding Journal» can be done at site: *www: rucont.ru*

РУКОНТ
НАЦИОНАЛЬНЫЙ ЦИФРОВОЙ РЕСУРС

We offer for the subscription all issues of the Journal in pdf format, starting from 2009. You can subscribe to individual issues or to the entire archive including all issues over a period of 2009–2011. The subscription is available for natural persons and legal entities.

ADVERTISEMENT
IN «THE PATON WELDING JOURNAL»

External cover, fully-colored:
First page of cover (190×190 mm) – $700
Second page of cover (200×290 mm) – $550
Third page of cover (200×290 mm) – $500
Fourth page of cover (200×290 mm) – $600

Internal cover, fully-colored:
First page of cover (200×290 mm) – $350
Second page of cover (200×290 mm) – $350
Third page of cover (200×290 mm) – $350
Fourth page of cover (200×290 mm) – $350

Internal insert:
Fully-colored (200×290 mm) – $300
Fully-colored (double page A3) (400×290 mm) – $500
Fully-colored (200×145 mm) – $150
Black-and-white (170×250 mm) – $80
Black-and-white (170×125 mm) – $50
Black-and-white (80×80 mm) – $15

- Article in the form of advertising is 50 % of the cost of advertising area
- When the sum of advertising contracts exceeds $1000, a flexible system of discounts is envisaged

Technical requirement for the advertising materials:

- Size of journal after cutting is 200×290 mm
- In advertising layouts, the texts, logotypes and other elements should be located 5 mm from the module edge to prevent the loss of a part of information

All files in format IBM PC:

- Corell Draw, version up to 10.0
- Adobe Photoshop, version up to 7.0
- Quark, version up to 5.0
- Representations in format TIFF, color model CMYK, resolution 300 dpi
- Files should be added with a printed copy (makeups in WORD for are not accepted)